

CHAKRA ROKAYA

# Printed Energy Storage for Energy Autonomous Flexible Electronics



CHAKRA ROKAYA

Printed Energy Storage  
for Energy Autonomous  
Flexible Electronics

ACADEMIC DISSERTATION

To be presented, with the permission of  
the Faculty of Information Technology and Communication Sciences  
of Tampere University,  
for public discussion in the auditorium TB109  
of Tietotalo, Korkeakoulunkatu 1, Tampere,  
on 9<sup>th</sup> December 2022, at 12 o'clock.

## ACADEMIC DISSERTATION

Tampere University, Faculty of Information Technology and Communication  
Sciences  
Finland

*Responsible  
supervisor  
and Custos*

Professor Donald Lupo  
Tampere University  
Finland

*Pre-examiners*

Adjunct Professor  
Kai Vuorilehto  
Helsinki University  
Finland

Associate Professor  
Per Lundgren  
Chalmers Univ. of Technology  
Sweden

*Opponent*

Professor Leif Nyholm  
Uppsala University  
Sweden

The originality of this thesis has been checked using the Turnitin OriginalityCheck service.

Copyright ©2022 author

Cover design: Roihu Inc.

ISBN 978-952-03-2688-3 (print)

ISBN 978-952-03-2689-0 (pdf)

ISSN 2489-9860 (print)

ISSN 2490-0028 (pdf)

<http://urn.fi/URN:ISBN:978-952-03-2689-0>



Carbon dioxide emissions from printing Tampere University dissertations  
have been compensated.

PunaMusta Oy – Yliopistopaino  
Joensuu 2022



# ACKNOWLEDGMENTS

This research work was performed at the Laboratory for Future Electronics at Tampere University. This work was financially supported by the Austrian Research Foundation's project Self-PoSH and the European Union's Horizon 2020 research project Smart2Go.

I would like to thank my supervisor, Prof. Donald Lupo, for his support and guidance throughout my work. I would also like to thank Dr. Jari Keskinen for being a great mentor and actively supporting my work throughout the research.

I would also like to acknowledge especially the co-authors of the publications, and past and present colleagues at the Laboratory for Future Electronics for their support.

Finally, I would like to thank my family (father, mother, brother, and sister) and relatives for their continuous support and encouragement in life. I especially want to thank my beloved wife for always being there for me. Without her support and encouragement, this work would not have been possible.



# ABSTRACT

High-performance and efficient energy storage devices are a necessity for fulfilling the global demand of the growing market of distributed electronics, IoT, mobile electronic devices, electric vehicles, and many more. Supercapacitors and batteries are a priority for energy storage applications. In comparison with batteries, supercapacitors have longer cycle life and higher power density. In some cases, supercapacitors are integrated with batteries to increase electrical performance and efficiency.

The aim of the research in this thesis is to develop and scale the design of a sustainable, low-cost, non-toxic, flexible, reliable, and eco-friendly energy storage device for energy-autonomous and distributed electronics platforms. The use of novel materials and a fabricating process for supercapacitor design were essential to achieve the goal of the research. With the use of low specific area electrode ink, the measured capacitance was 3–4 mF in dual cell supercapacitors. Similarly, a PET/Al laminated metal current collector has advantages due to high conductivity, low ESR, and the use of PC electrolyte (2.5 V/cell) to the target voltage range for low power BLE transmission applications. We also developed a PEDOT: PSS based polymer electrolytic capacitor as an alternative to supercapacitors, which demonstrated a way to print flexible capacitors of a few  $\mu\text{F}$ . This capacitor was modeled for low frequency applications such as smoothing and filtering. The second focus of the thesis was to perform a reliability study on the energy storage devices. This helps to observe the performance of the device in different situations, from normal to harsh environments. The supercapacitor's electrical performance was stable over a wide temperature range from  $-40\text{ }^{\circ}\text{C}$  to  $100\text{ }^{\circ}\text{C}$ . The supercapacitors maintain 100% retention for 10,000 bending cycles and a minimum bending radius of 0.41 cm, showing a high degree of flexibility. The device's performance declined after thermal shock testing due to defects and cracks in the porous electrode because of rapid prolonged temperature cycling between  $-40\text{ }^{\circ}\text{C}$  and  $100\text{ }^{\circ}\text{C}$ .

The final part of the thesis is to harvest green energy from ambient surroundings using an organic photovoltaic (OPV) module or a piezoelectric transducer. The maximum indoor energy harvested with an OPV module and stored to the supercapacitor was 39 mJ.

On the other hand, with a piezoelectric transducer, the maximum harvested energy was 1.1 mJ and peak power was 11.1 mW. The harvested energy was stored in our printed and flexible storage devices. We also demonstrated that the energy harvested was enough to power an LED driver circuit. Thus, these printed, low-cost, novel, and flexible devices open a door for the field of energy autonomous flexible electronics.

# CONTENTS

1	Introduction.....	15
1.1	Aims and scope of the thesis.....	16
1.2	Structure of the thesis .....	17
1.3	Author's contribution .....	18
2	Background.....	19
2.1	Capacitors .....	19
2.2	Basic principles of supercapacitors .....	20
2.3	Types of supercapacitors .....	22
2.3.1	Electrochemical double-layer capacitors .....	23
2.3.2	Pseudocapacitors .....	23
2.3.3	Hybrid capacitors.....	24
2.4	Energy harvesting and storage .....	24
2.5	Supercapacitor vs. battery.....	30
2.6	Applications of supercapacitors .....	31
3	Material and methods .....	34
3.1	Supercapacitor materials .....	34
3.1.1	Current collector.....	35
3.1.2	Electrode .....	36
3.1.3	Electrolyte .....	37
3.1.4	Separator.....	37
3.2	Device fabrication .....	38
3.3	Device characterization.....	39
3.3.1	Cyclic voltammetry.....	41
3.3.2	Electrochemical impedance spectroscopy .....	43
3.3.3	Leakage current measurement.....	44
4	Results and discussion .....	46
4.1	Substrate and current collector .....	46
4.2	Electrode materials.....	49
4.3	Ambient energy harvesting.....	52
4.4	Reliability of the devices .....	56
5	Conclusions .....	60

## *List of Figures*

**Figure 1.** Schematic diagram of parallel plate capacitor.

**Figure 2.** Schematic structure of polymer electrolytic capacitor.

**Figure 3.** Operational principle of supercapacitor.

**Figure 4.** Electric double layer model. Helmholtz model (a), Gouy- Chapman model (b), and Stern model (c).

**Figure 5.** Supercapacitor types and electrode materials. Adapted from [15].

**Figure 6.** Ambient energy harvesting. Adapted from [24].

**Figure 7.** Schematic drawing of bulk heterojunction solar cell. Adapted from [27].

**Figure 8.** Schematic diagram of operating principle in organic solar cells. Adapted from [26].

**Figure 9.** Direct and reverse piezoelectric effect. Adapted from [34].

**Figure 10.** Ragone plot of electrical storage systems. Adapted from [8].

**Figure 11.** Portable devices powered with a supercapacitor. Adapted from [47].

**Figure 12.** Schematic drawing of the electrode top view and a cross-section of the entire device.

**Figure 13.** Schematic representation of the doctor blade coating.

**Figure 14.** Setup of blade coating (left) and screen printing (right).

**Figure 15.** An example of galvanostatic discharge to measure IR drop value.

**Figure 16.** An example of CV measurements of the supercapacitors (a), and constant current charge-discharge measurement (b).

**Figure 17.** An example of a Nyquist plot. Adapted from **Publication II**.

**Figure 18.** Dual cell supercapacitor made of PET/Al laminate (left) adapted from **Publication I** and Al foil Alpha 897 (right).

**Figure 19.** Al foil cross-section (left) and surface structure (right). Adapted from **Publication III**.

**Figure 20.** Nyquist plot of real and imaginary impedance (measured and fitted). Adapted from **Publication I**.

**Figure 21.** Polymer electrolytic capacitor. Adapted from **Publication III**.

**Figure 22.** Cyclic voltammetry graph. Adapted from **Publication III**.

**Figure 23.** Piezoelectric transducer.

**Figure 24.** Integration of OPV, IC and supercapacitor. Adapted from **Publication I**.

**Figure 25.** Voltage measurement across the dual cell supercapacitors as function of time. Adapted from **Publication I**.

**Figure 26.** Block diagram of piezo energy harvesting module. Adapted from **Publication III**.

**Figure 27.** Output response of piezoelectric transducer (a) and rectified voltage of transducer 2 to 20 Hz (b). Adapted from **Publication III**.

**Figure 28.** CV measurement of device at temperatures from -40 to 100 °C. Adapted from **Publication II**.

**Figure 29.** Microscopic image of electrode layer after thermal shock test shows defects and cracks. Adapted from **Publication II**.

**Figure 30.** Photographs showing flexibility of supercapacitor (left) and polymer electrolytic capacitor (right). Adapted from **Publications II, III**.

**Figure 31.** CV measurement up to 10,000 bending cycles of supercapacitors. Adapted from **Publication II**.

## *List of Tables*

**Table 1.** Comparison of specific energy and power density using different electrode materials [14].

**Table 2.** Comparison of energy storage technology [1]. (Results here are for full device data, compared to the electrode materials only shown in Table 1).

**Table 3.** Harvested power from ambient energy sources [46].

**Table 4.** Properties of PZT-5H and PVDF materials [35].

**Table 5.** Commercial supercapacitors with capacitance and voltage range [54]. (High voltage values in the table are for series connected modules).

**Table 6.** Electrical parameters of the supercapacitors reported in publications.

**Table 7.** Energy harvested, and storage reported in the publications.



# ABBREVIATIONS AND SYMBOLS

A	Area
AC	Activated carbon
Al	Aluminum
BLE	Bluetooth low energy
C	Capacitance
CV	Cyclic voltammetry
d	Plate distance
D	Displacement
DCSC	Dual cell supercapacitor
E	Electric field
EDL	Electric double layer
EIS	Electrochemical impedance spectroscopy
EV	Electric vehicle
ESR	Equivalent series resistance
F	Farad
HOMO	Highest occupied molecular orbital
IC	Integrated circuit
IoT	Internet of things
LUMO	Lowest unoccupied molecular orbital
OPV	Organic photovoltaic
PEDOT:PSS	Poly(3,4-ethylenedioxythiophene) polystyrene sulfonate
PC	Propylene carbonate
pC/N	picocoulomb/Newton
PET	Polyethylene terephthalate
PVDF	Polyvinylidene difluoride
PZT	Lead zirconate titanate
RFID	Radio frequency identifications
s	Mechanical compliance
SEM	Scanning electron microscopy
SoC	System on chip
T	Stress

TEABF <sub>4</sub>	Tetraethylammonium tetrafluoroborate
WSN	Wireless sensor networks
X	Strain
μ	Micro
ε	Permittivity

# LIST OF PUBLICATIONS

- I. C. Rokaya, J. Keskinen, and D. Lupo “Integration of fully printed and flexible organic electrolyte-based dual cell supercapacitor with energy supply platform for low power electronics,” *J. Energy Storage*, vol. 50, pp. 1–10, 2022, doi: 10.1016/j.est.2022.104221.
- II. C. Rokaya, J. Keskinen, S. Lahokallio, and D. Lupo, “Reliability test of fully printed and flexible organic electrolyte-based supercapacitor”, *Flex. Print. Electron.*, vol. 7, pp. 1-11, 2022, doi: <https://doi.org/10.1088/2058-8585/ac9001>
- III. C. Rokaya, J. Keskinen, C. Bromels, P. Schaffner, E. Küzeci, and D. Lupo, “Polymer-based printed electrolytic capacitor and its circuitry application in a low pass filtering, rectifying and energy storage unit,” *Flex. Print. Electron.*, vol. 6, no. 2, pp. 1–11, 2021, doi: 10.1088/2058-8585/ac023d
- IV. C. Rokaya, P. Schaeffner, S. Tuukkanen, J. Keskinen, and D. Lupo, “Motion energy harvesting and storage system including printed piezoelectric film and supercapacitor,” *IEEE International Flexible Electronics Technology Conference*, 2019, pp. 1-8, doi: 10.1109/IFETC46817.2019.9073717



# 1 INTRODUCTION

Research on energy storage devices is becoming popular in order to manage energy and environmental problems through increasing energy efficiency and minimizing greenhouse gas emissions to reduce global warming. Sustainable, nontoxic, and environmentally friendly energy storage devices reduce energy waste and are efficient [1][2]. The main energy storage devices are supercapacitors and batteries for storing harvested energy. In addition, these devices act as a backup source when the primary energy source is not available [2][3]. Supercapacitors are also known as electric double-layer capacitors (EDLC), ultracapacitors, or electrochemical capacitors [4][5]. They can offer higher power densities than batteries, and higher energy densities than conventional capacitors [6]. Batteries consist of problematic materials such as lead or lithium, and recycling is required by law in the European Union (EU) [4]. Supercapacitors have become popular in many applications because of advantages such as quick charging time, high efficiency, long life cycle, wide temperature ranges, flexibility, and no risk of explosion [3][6][7] although they have far lower energy density than batteries [8]. Further, supercapacitors can be fabricated with simple printing and coating methods using inexpensive and abundant environmentally friendly materials [4][9].

Energy harvesting from renewable, sustainable, and ambient energy sources such as heat, motion, pressure, vibration, light, and sound has become popular in low-power flexible electronic devices. Thin, lightweight and bendable [10] energy storage systems such as supercapacitors are thus needed for a variety of flexible, wearable, lightweight, and portable electronics [11][12]. Supercapacitors are used to provide short-term peak power in many energy applications. Examples of the uses of a supercapacitor include the Internet of things (IoT), wireless sensor networks (WSN), RFID tags, Bluetooth Low Energy (BLE) transmission, and sensors [4].

## 1.1 Aims and scope of the thesis

The first aim of the thesis is to develop energy storage devices and capture ambient energy for distributed electronics. The choice of materials determines the electrochemical behavior of the device related to voltage, capacitance, device flexibility, and wide temperature range. We focus on dual cell supercapacitors (DCSCs) with low capacitance value and a working voltage up to 5 V, as well as printed electrolytic capacitors. The primary research questions are:

1. How does choice of materials, architecture, and processes affect the performance of energy storage devices. Is it possible to optimize for specific applications?
2. Can printed supercapacitors based on organic electrolyte achieve the capacitance and ESR values required to power radio transmission of information from smart objects?
3. Can printed electrolytic capacitors be used for energy storage, or alternatively to enable integration into printed electronic circuits?
4. Can energy harvesting be integrated with printed energy storage in novel devices?
5. Can printed supercapacitors survive the mechanical and thermal stresses expected from integration into and use in products, e.g. smart skis for winter sports?

**Publication I** presents the development of the materials and architecture for 5V supercapacitor modules with capacitance of a few mF and sufficiently low series resistance to power a Bluetooth Low Energy (BLE) transmission. The work reports on two-cell supercapacitor modules using carbon black as electrode and propylene carbonate as electrolyte. These materials were chosen to lower the capacitance and increase the maximum voltage to values suitable for the target application. These supercapacitors were also integrated with an OPV (organic photovoltaic) module for indoor light harvesting and storage for powering low-power devices.

In **Publication II**, the results of a reliability study on the modules reported in the first publication are presented. As the devices are to be integrated into a smart ski fitted with multiple sensors, they need to withstand elevated temperatures during e.g., lamination or in-molding and low temperatures during skiing, as well as to demonstrate mechanical flexibility. It is found that the devices are highly stable at temperatures from  $-40\text{ }^{\circ}\text{C}$  to  $+100\text{ }^{\circ}\text{C}$ , as well as to cyclic bending at a radius of only 0.41 cm, though some degradation was observed after multiple thermal shock tests.

In **Publication III**, we reported the fabrication of a polymer-based electrolytic capacitor with specific capacitance of  $1\text{ }\mu\text{Fcm}^{-2}$ . This capacitor is applicable in a passive low pass filter for smoothing purposes, with a cut-off frequency of 1.03 kHz. The integration of this capacitor with a vibration-motion piezo transducer harvester and rectifier circuit gives energy of about 1 mJ and can be applicable in low-power portable devices.

In **Publication IV**, we report on the study of a piezoelectric transducer as an energy harvester, connected to a rectifier circuit for converting AC to DC and a supercapacitor and commercial electrolytic capacitor as a storage unit. In addition, the bending characteristics, sensitivity, and charge generation of the piezoelectric transducer were explained. A peak power of 11.1 mW was generated from the piezoelectric transducer, which was sufficient to drive an LED.

## 1.2 Structure of the thesis

The thesis consists of five chapters and four peer-reviewed publications. Chapter 1 describes the aim and scope of the thesis, the thesis structure, and gives a broad overview of the topic. Chapter 2 explains the basic working principles of capacitors and supercapacitors, including a comparison with other energy storage devices, and briefly introduces energy harvesting from OPV and piezoelectric materials. Chapter 3 provides a brief explanation of the materials and methods used in this thesis. The main results and findings are discussed in Chapter 4. Finally, Chapter 5 presents the conclusion of the thesis with some discussion of possible future work. The publications are added at the end of the thesis.

## 1.3 Author's contribution

In collaboration with other researchers, the articles mentioned in this thesis have been published and the author's contribution is as follows:

**Publication I:** The author and co-authors planned the research work. The author was responsible for ink preparation, device fabrication, device characterization, and writing the first draft. The manuscript was revised and finalized with the assistance of Dr. Jari Keskinen and Prof. Donald Lupo.

**Publication II:** The author and co-authors planned the research work. The author was responsible for ink preparation, device fabrication, device characterization, and writing the first draft. The manuscript was rewritten and finalized with the co-authors. Dr. Sanna Lahokallio assisted in performing temperature and thermal shock tests at Trelic Oy.

**Publication III:** The author and co-authors planned the research work. The author was responsible for ink preparation, device fabrication, device characterization, and writing the first draft. The manuscript was rewritten and finalized with the co-authors. The piezoelectric transducer as an energy source was fabricated by Philipp Schäffner. Erkan Küzeci made the SEM characterization.

**Publication IV:** The author and co-authors planned the research work. The author was responsible for ink preparation, device fabrication, device characterization, and writing the first draft. He also designed and fabricated the 3D setup model for piezo energy harvesting. The manuscript was rewritten and finalized with the co-authors. The piezoelectric transducer energy source was fabricated by Philipp Schäffner.



## 2 BACKGROUND

### 2.1 Capacitors

Capacitors store electrical energy in the form of an electric field. They consist of two conducting plates separated by a layer of dielectric material. Popular dielectric materials are metal oxides, insulating polymers, ceramic, mica, silicon base glass, air, and vacuum. The capacitors are categorized as polarized and non-polarized capacitors. Polarized capacitors have marked positive and negative terminals. This means the positive terminal should be connected to a positive power supply and the negative terminal should be connected to a negative power supply. Reversing the polarity shorts or damages the device. On the other hand, non-polarized capacitors have no fixed polarity and terminals can be connected to the power supply in either way. Electrolytic capacitors and most supercapacitors are polarized, and ceramic and film capacitors are non-polarized. The schematic structure of the parallel plate capacitor is shown in Figure 1. The capacitance value depends on the plate area, dielectric materials, and separation distance.

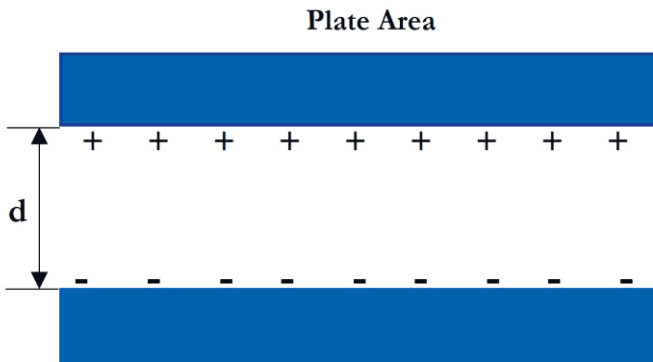


Figure 1. Schematic diagram of parallel plate capacitor.

The expression of the parallel plate capacitance is given by Equation 1.

$$C = \frac{\epsilon A}{d} \quad (1)$$

where  $C$  is the capacitance,  $A$  is the area of the plate,  $\epsilon$  is the permittivity of the dielectric material, and  $d$  is the separation between plates.

The anode of an electrolytic capacitor has a high surface area obtained by the electrochemical etching process. In addition, the anodizing process results in an insulating dense oxide layer on top of the anode that acts as a dielectric [13]. Then, deposition of different conducting materials on top of the oxide layer acts as the cathode of the capacitor. Electrolytic capacitors have relatively large capacitance due to the enlarged surface area. The anode material in electrolytic capacitors can be, e.g., aluminum or tantalum, or also a conducting polymer such as PEDOT-PSS, which is used in **Publication III**. The schematic structure of an electrolytic capacitor is shown in Figure 2.

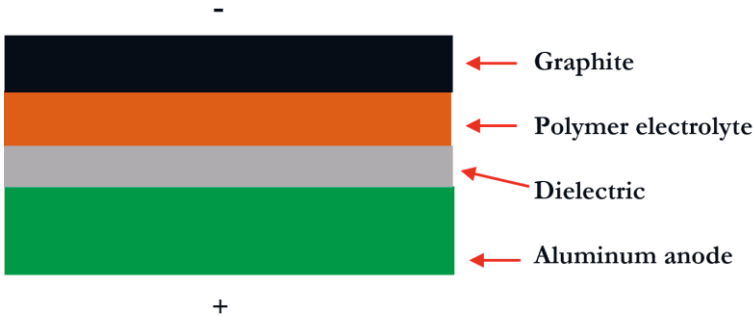


Figure 2. Schematic structure of polymer electrolytic capacitor

## 2.2 Basic principles of supercapacitors

In supercapacitors based on electric double layer, electrical energy is stored at the interface between the electrode and electrolyte due to the electric field. Electric double layer capacitor (EDLC) consists of two electrodes that are separated by the separator and filled with electrolytes between them [14] [15]. When the device is charged with external voltage, then the electric double layer is formed. The basic working principle of a supercapacitor is shown in Figure 3.

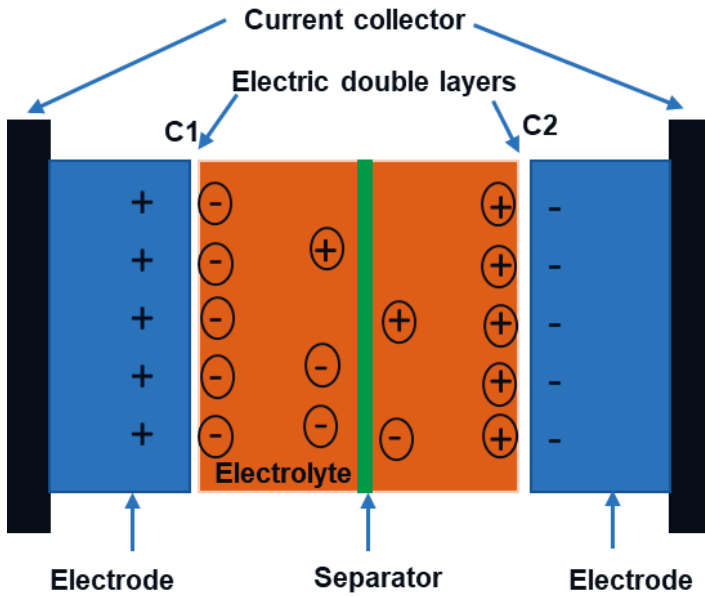


Figure 3. Operational principle of a supercapacitor.

The electric double layer (EDL) theory was first explained by Hermann von Helmholtz and later further modeled by Gouy-Chapman and Stern [15][16]. Helmholtz demonstrates a simple model, as shown in Figure 4(a), concerning the spatial charge separation at double layer interfaces. Here, the negative charges are attracted toward the positive charges and vice versa, forming an electric double layer. The distance between charges is denoted as  $d$ .

The Gouy-Chapman model is also a diffuse model, because the ions in the electrolyte diffuse further from the interface. The model consists of a diffusion layer as shown in Figure 4(b). This model is not accurate for highly charged double layers [15][16].

The Stern model, as shown in Figure 4(c), is a combination of the Helmholtz and Gouy-Chapman models. The first layer consists of the immobile ions captured inside the porous electrode surface and the second layer contains mobile ions in the diffusion layer [15][16].

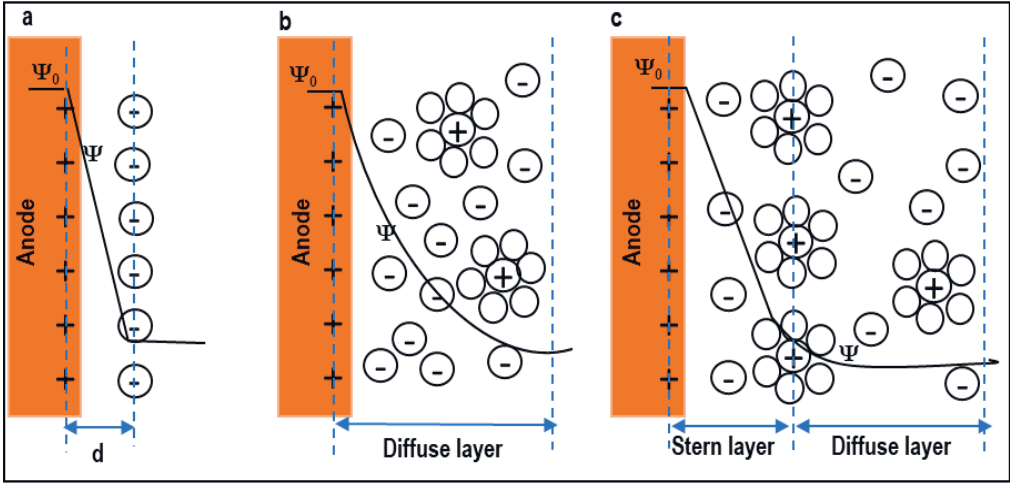


Figure 4. Electric double layer model. Helmholtz model (a), Gouy-Chapman model (b), and Stern model (c) Adapted from [15].

As there are double interface layers inside the supercapacitor, the total capacitance is the combination of the layers at positive and negative electrodes and is given by Equation 2.

$$C = \frac{C_1 C_2}{C_1 + C_2} \quad (2)$$

where  $C$  is the total capacitance and  $C_1$  and  $C_2$  are individual capacitances.

## 2.3 Types of Supercapacitors

The chart for different types of supercapacitors is shown in Figure 5. The classification is based on the type of materials, such as activated carbon, graphene or conducting polymers, used in device fabrication and on the structure, which is either symmetric or asymmetric.

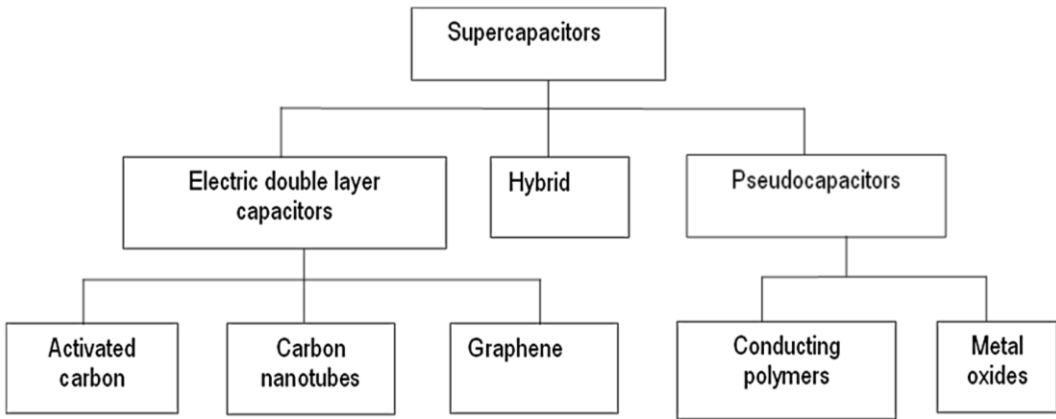


Figure 5. Supercapacitor types and electrode materials. Adapted from [15].

### 2.3.1 Electric double-layer capacitors

Electric double-layer capacitors are symmetrical, and typically made up of two identical carbon electrodes. The most common electrode material used in EDLCs is activated carbon (AC), though other materials like carbon nanotubes and graphene have also been used [17][18][19]. These materials are easily available, inexpensive, have a large surface area, and are porous, resulting in a higher specific capacitance than electrostatic capacitors. A comparison of energy density and power density of the supercapacitor with different electrode materials is shown in Table 1.

### 2.3.2 Pseudocapacitors

Pseudocapacitors consist of an electrode based on conducting polymers such as polyaniline, polypyrrole [20], or metal oxide such as lithium cobalt oxide ( $\text{LiCoO}_2$ ), manganese dioxide ( $\text{MnO}_2$ ), ruthenium oxide ( $\text{RuO}_2$ ), or nickel oxide ( $\text{NiO}$ ) [21]. Pseudocapacitance is achieved due to reversible reduction-oxidation (redox) reactions close to or at the surface of a material in contact with the electrolyte. These capacitors provide higher energy density than electric double layer capacitors [21]. Polyaniline can give a charge density of  $140 \text{ mAhg}^{-1}$ , which is slightly lower than that obtained from metal oxides such as  $\text{LiCoO}_2$  but much higher than carbon devices, which provide about  $15 \text{ mAhg}^{-1}$  [22].

Table 1. Comparison of specific energy and power density using different electrode materials [14].

Carbon material	Energy density (Wh.kg <sup>-1</sup> )	Power density (kW.kg <sup>-1</sup> )	Electrode capacitance (F.g <sup>-1</sup> )
Activated carbon	5–25	10–40	50–125
Carbon fiber cloth	2–36	5–11	3.5–60
Carbon nanotube	0.5–40	30–1000	12–120
Graphene	20–70	40–250	100–200
Carbon nanofiber	10–20	5–20	50–100
Templated carbon	5–60	5–40	10–150

### 2.3.3 Hybrid capacitors

Hybrid capacitors are also referred to as asymmetric supercapacitors. These supercapacitors use active electrode materials based on a combination of electric double layer and pseudocapacitive processes. They show non-Faradaic and Faradaic battery-type behavior. An example of this is a lithium-ion capacitor, which consists of high surface area activated carbon as the positive electrode and lithium ion-containing material as a negative electrode. These capacitors can store ten times more energy than conventional EDLCs and have long cycle life [15].

## 2.4 Energy harvesting and storage

The process of capturing electrical energy from our surroundings is called energy harvesting [23]. Suitable ambient energy sources for sustainable renewable energy scavenging from ambient energy sources include pressure or movement, light, heat, and wind. The use of the energy from these renewable sources reduces greenhouse gas emissions (CO<sub>2</sub>) and enables cleaner energy technology [1]. The harvested energy can be used in multiple applications such as low-cost microelectronic devices, wireless sensor networks, the Internet of Things, and portable devices [24]. Options for various energy harvesting sources are shown in the chart in Figure 6.

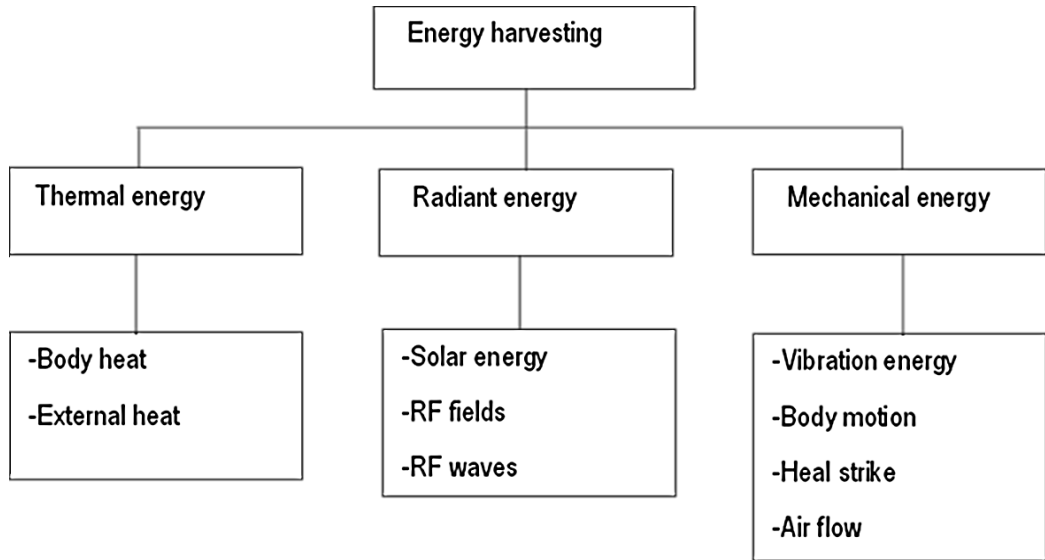


Figure 6. Ambient energy harvesting. Adapted from [24].

The integration of energy storage devices with an energy harvester is very important and improves the performance of the system. An energy storage system such as capacitor, supercapacitor, and battery should be reliable, efficient, and affordable. These systems store the energy generated and act as a backup power supply if needed. A comparison of energy storage technology is shown in Table 2.

Table 2: Comparison of energy storage technologies [1]. (Results here are for full device data, compared to the electrode materials only shown in Table 1).

Technology	Energy density (Wh/kg)	Cost capital (€/kW)	Efficiency (%)
Supercapacitors	0.1–5	200–1000	85–98
Nickel batteries	20–120	200–750	60–91
Lithium batteries	80–150	150–250	90–100
Lead acid battery	24–45	50–150	60–95

This thesis mainly focuses on two energy harvesters: the organic photovoltaic (OPV) module, and the piezoelectric transducer. Light is the most plentiful energy source available indoors from such sources as halogen lamps, LEDs, and fluorescent tubes, as well as outdoor in the form of sunlight [25]. This harvester converts light into electrical power using the photovoltaic principle. The basic architecture of the organic solar cell

and a schematic diagram of the operating principle are shown in Figure 7 and Figure 8 respectively. An OPV device consists of the organic semiconducting material sandwiched between the top and bottom electrode. Organic solar cells are mainly of four types—single layer, bilayer, bulk heterojunction, and tandem solar cell. When the light strikes the cell, the energy gets absorbed. The energy of the photon should be equal to or greater than the bandgap for the excitation of the electron. The electron in the highest occupied molecular orbital (HOMO) moves to the lowest unoccupied molecular orbital (LUMO). This results in the creation of holes and electron pairs called excitons. The excitons are localized and held together by the high coulombic force of attraction because of the low dielectric constant of the active layer in the range of 3–4. To obtain the charge transport process, the excitons need to be separated; this process is called exciton dissociation. The dissociations, or charge separation, can only be achieved at the donor-acceptor interface. The electrons travel from the LUMO of a donor to the LUMO of an acceptor because the energy level of the LUMO of the donor is at a higher state, forming an electron-hole pair. After the separation, the electron moves to the acceptor layer and is collected at the cathode. The hole moves to the donor layer and is collected at the anode [26][27]. The recent progress in solar technology in terms of flexibility, robustness, low cost, and lightweight OPV module, is positive in terms of possible energy harvesting [28]. Ambient indoor light harvesting using commercial OPVs helps to generate energy in the range of 10 to 100  $\mu\text{W}/\text{cm}^2$  [29][30]. Instead of directly integrating the supercapacitor with OPV, the use of an energy management integrated circuit (IC), such as E-peas AEM10941, helps to maintain charge balance, voltage protection, regulation, and increased storage efficiency by maintaining operations as far as possible at the maximum power point of the OPV device. Here, the IC acts as a bridge between the harvester and the supercapacitors [31].

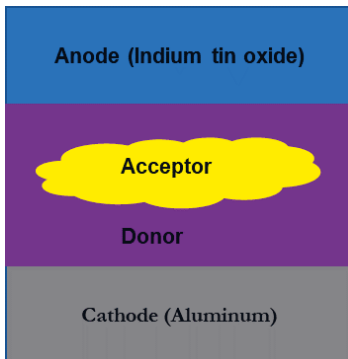


Figure 7. Schematic drawing of bulk heterojunction solar cell. Adapted from [27].



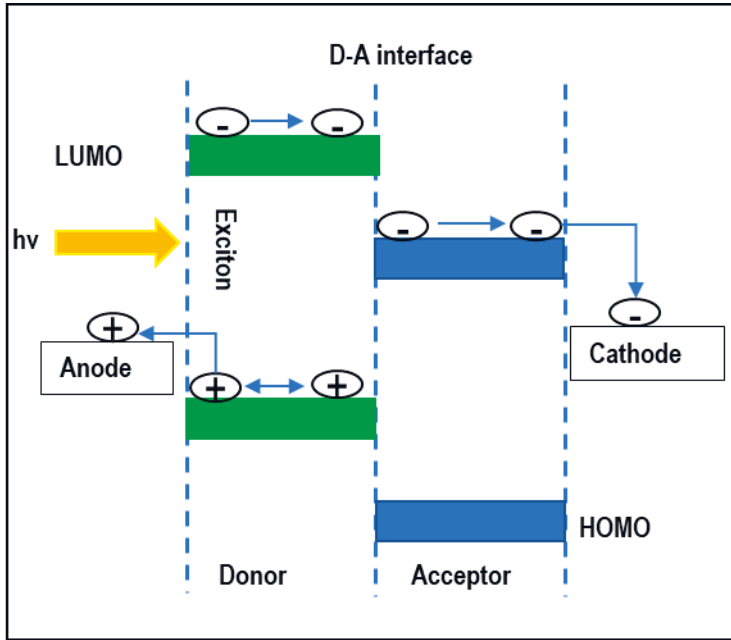


Figure 8. Schematic diagram of operating principle in organic solar cells. Adapted from [26].

Energy can also be harvested from pressure, motion, or deformation by using a piezoelectric transducer. Such a transducer generates energy when mechanical force is applied to the material and is based on a phenomenon known as the piezoelectric effect [32], which was discovered in 1880 by Pierre and Jacques Curie. This effect involves a shift of charges or ions in piezoelectric materials under mechanical stress. Figure 9 shows the direct piezoelectric effect and converse piezoelectric effect. In the direct effect, the electricity is generated when pressure is applied to the piezoelectric materials. If the piezoelectric materials are mechanically deformed by applying an electric potential, then the reverse piezoelectric effect occurs, and the electrical energy is converted to motion. In terms of the application, the direct effect is common in sensors and transducers, whereas the reverse effect is seen in actuators [33]. The expressions of the direct and converse piezoelectric effect are given in Equations 3 and 4.

$$D = dT + \epsilon E \text{ (Direct effect)} \quad (3)$$

$$X = sT + d_e E \text{ (Converse effect)} \quad (4)$$

where  $D$  is electrical displacement,  $d$  is the direct piezoelectric coefficient,  $d_t$  is the converse piezoelectric coefficient,  $T$  is stress,  $\epsilon$  is permittivity,  $X$  is the strain,  $E$  is the electric field, and  $s$  is mechanical compliance.

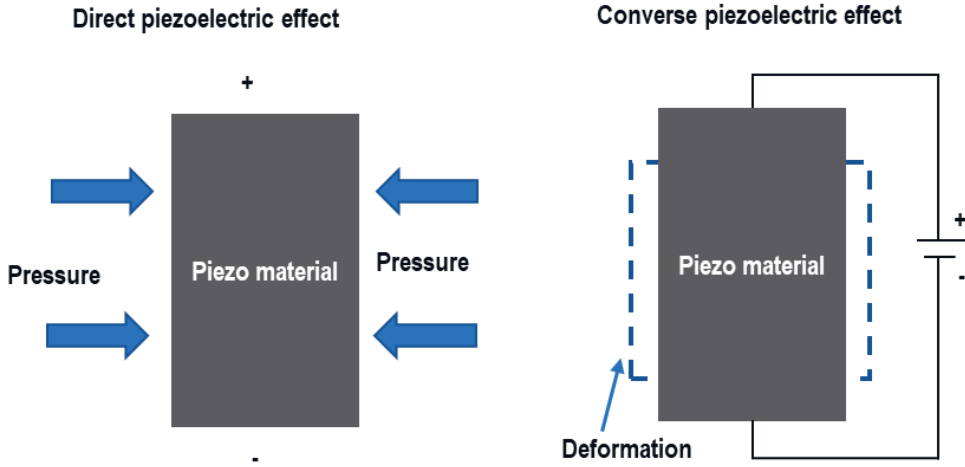


Figure 9. Direct and reverse Piezoelectric effects. Adapted from [34].

The two most common piezoelectric material groups are piezoceramics such as lead zirconate titanate (PZT), barium titanate (BT), and piezopolymers such as polyvinylidene difluoride (PVDF) and its copolymer trifluoroethylene (PVDF-TrFE). Piezoceramics provide a high energy conversion efficiency and have a large electro-mechanical coupling constant but are rigid and brittle. Piezopolymers are flexible and have a low electro-mechanical coupling constant [33]. Energy harvesting using cantilever beams geometry of different shapes and sizes is quite common. Other harvesters use disc shapes such as cymbal transducer and circular diaphragms [35]. Benasciutti et al. investigated a harvester model using a rectangular bimorph cantilever beam with PZT layers [36]. Tong et al. designed and simulated a PZT cantilever beam that gives maximum outpower of 4.4 mW [37]. Mohamed et al. designed a T-shaped cantilever that gives 3.4 times more power than a triangular-shaped cantilever beam at low excitation frequency up to 10 Hz. The author concluded that shape optimization of beams helps to maximize power generation [38]. Shenck et al. developed energy scavenging shoes with flexible, multilayer PVDF bimorph that generates approximately 1.3 mW of power [39]. Puscasu et al. developed an energy harvesting tile prototype with commercially available piezoelectric membranes that was able to produce 17.7 mJ of energy [40]. These previously reported harvesters were compared with the printed PVDF:TrFE transducer used in our experiment (**Publication**

**IV)**, which was able to generate 11.1 mW output power. Piezoelectric transducers are flexible, light weight, and can be integrated with the human body for health monitoring, wearables, shoes, bags and other motion harvesters [41]. Piezoelectric transducers are popular due to their high energy density compared to electromagnetic and electrostatic transducers [42]. Piezoelectric energy harvesting has been reported extensively [41][42][43][44][45]. The harvested energy can be stored in energy storage devices that can be used for different applications like wireless sensors networks, cardiac pacemakers, and Bluetooth modules [29] [44]. Table 3 shows the amount of the harvested power from ambient energy sources. Table 4 shows the properties of piezoelectric materials.

Table 3. Harvested power from ambient energy sources [46].

Energy Source	Characteristics	Scavenging	Harvested power
Light	Indoor	Solar cell	10 $\mu\text{W}/\text{cm}^2$
	Outdoor		10 $\text{mW}/\text{cm}^2$
Vibration	Human	Piezoelectric	4 $\mu\text{W}/\text{cm}^2$
	Industry		100 $\mu\text{W}/\text{cm}^2$
Thermal	Human	Thermoelectric	30 $\mu\text{W}/\text{cm}^2$
	Industry		1-10 $\text{mW}/\text{cm}^2$
Radio frequency	GSM900 MHz	Antenna	0.1 $\mu\text{W}/\text{cm}^2$
	WiFi		0.001 $\mu\text{W}/\text{cm}^2$

Table 4. Properties of PZT-5H and PVDF materials [35].

Property	PZT-5H (ceramic)	PVDF (polymer)
Density( $\text{g}/\text{cm}^3$ )	7.65	1.78
Dielectric constant	3250	6
Young's modulus Y33	71.4	2
Mechanical quality factor Qm	32	10
Piezoelectric charge constant d33 (pC/N)	590	25
Piezoelectric charge constant d31 (pC/N)	-270	12-23
Electro-mechanical coupling factor K33	0.75	0.22

## 2.5 Supercapacitor vs. battery

Both batteries and supercapacitors are energy storage systems; the main differences being their mechanisms of storing energy. Supercapacitors store energy in the form of an electric field, whereas batteries store it in a chemical form. In an ideal case, there are no reduction-oxidation (redox) reactions in supercapacitors—only electrostatic processes for charging and discharging the device. On the other hand, the battery operation principle is based on chemical reduction and oxidation [20]. As shown in Figure 10, supercapacitors are a better choice when high power density is required, whereas batteries are preferred for high specific energy. In addition, supercapacitors have higher specific energy than conventional capacitors. Batteries are suitable for charge-discharge cycles of a few hours due to slow chemical reactions. Electrolytic capacitors are preferred over short cycle times in the order of milliseconds (ms) or microseconds ( $\mu$ s).

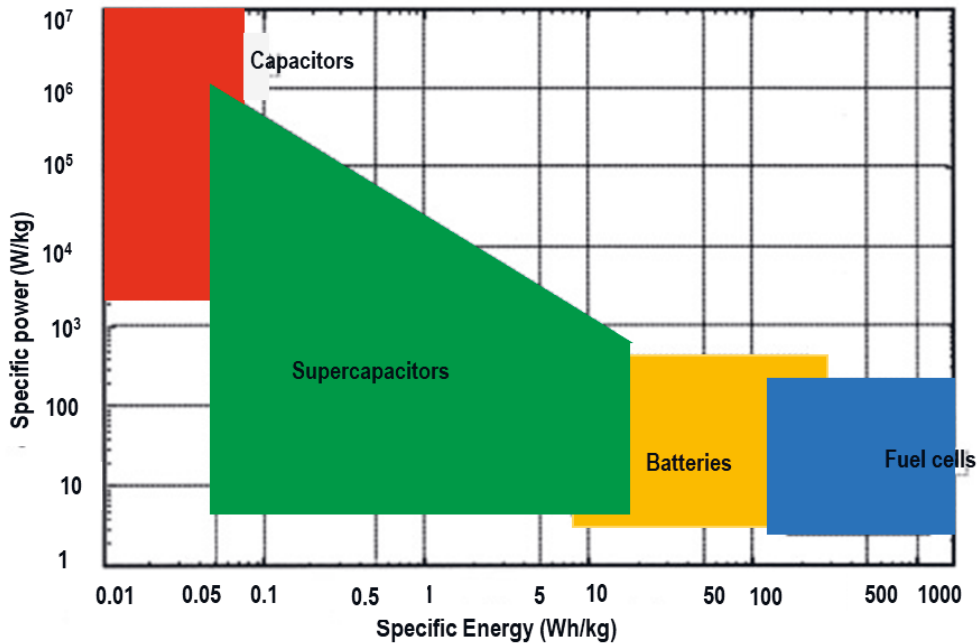


Figure 10. Ragone plot of electrical storage systems. Adapted from [8].

## 2.6 Applications of supercapacitors

Supercapacitors are experiencing a large market growth and have been used in a wide range of applications in recent years. Portable and flexible electronics, such as smartwatches, cameras, phones, and other smart devices, are ubiquitous in modern society. Supercapacitors can play a very important role as an energy storage system to power those smart devices. It is easy to integrate flexible supercapacitors with wearable textiles and sensors for powering electronic devices, as shown in Figure 11. In addition, supercapacitors can be integrated with energy harvesters such as OPV modules or piezoelectric transducers for storing harvested energy[47]. Supercapacitors are used in back-up power applications, providing power peaks when primary energy is unavailable. They have several advantages, such as high specific power, long cycle life, wide temperature range, and flexibility [48]. This makes the devices well suited for military and aerospace applications such as uninterrupted power supply in military vehicles, black boxes on helicopters, airbag deployment, and GPS-guided missiles [47] [49]. The hybrid combination of lithium-ion batteries and supercapacitors as an energy storage system has been recently reported [50]. This system is good for applications such as toys, drones, and low-cost microelectronics devices, and has advantages such as fast charging, long life, and high power density, but also some disadvantages, such as discontinuity and matching of power, and challenging synchronization with a feedback system [1][51]. In many cases, supercapacitors alone can make the system more efficient. A few examples include switched-mode power supply, system on a chip (SoC), IoT, sensors, and BLE. The use of supercapacitors in electric vehicles (EV) to conserve kinetic energy obtained from regenerative braking leads to an improvement in vehicle fuel efficiency [24]. Supercapacitors are widely used in the energy sector—according to Maxwell Technologies Inc. some 20 to 30% of wind turbines are equipped with a supercapacitor pitch control system [52]. In a microgrid system, supercapacitors can maintain quick load fluctuations [53]. Similarly, supercapacitors have been used on solar farms in California where an energy storage duration of 20 to 30 seconds is required to control short term solar power fluctuations and provide ramp rate control [48]. Table 5 shows examples of commercial supercapacitors with capacitance and voltage range.



Figure 11. Portable devices powered with a supercapacitor. Adapted from [47].

Table 5. Commercial supercapacitors with capacitance and voltage range [54]. (High voltage values in the table are for series connected modules).

Manufacturer	Capacitance range (F)	Voltage range (V)
Maxwell	1–3400	2.7–2.85
Murata	0.035–1	4.2–5.5
Ioxus	1300–3150	2.7–2.85
Panasonic	0.1–100	2.1–5.5
Bussmann	0.1–3400	2.5–5.5
Nippon Chemi-Con	50–1400	2.5

## 3 MATERIALS AND METHODS

Chapter 3 describes the materials, fabrication technique, and measurement tools used in our research.

### 3.1 Supercapacitor materials

The use of materials in fabrication depends on the requirements and purposes of the device. The key materials are current collectors, electrodes, electrolytes, and separators. The use of recyclable, non-toxic, abundant, low-cost, and incinerable materials is preferred. The schematic drawing of a supercapacitor is shown in Figure 12.

The current collector is responsible for collecting electrons from electrode material and transferring them to the external circuit. Current collectors are commonly metals such as copper, aluminum, nickel, and stainless steel. Most supercapacitors use two current collectors: one at the anode and one at the cathode terminal. The stability and conductivity of a supercapacitor partly depends on the current collector [55]. The internal resistance of the device can be improved by minimizing the contact resistance between the electrode and the current collector. This will give high energy density and quick charge-discharge time constant.

Materials with a high surface area should be used as electrodes for supercapacitors, because capacitance is proportional to the surface area. The electrode materials commonly used in supercapacitors are activated carbon; other materials like carbon black, graphene, conducting polymers, and transition metals have also been applied. Carbon electrodes have high porosity, a surface area of up to  $3000 \text{ m}^2\text{g}^{-1}$ , and capacitance of  $250 \text{ Fg}^{-1}$  [56]. Activated carbon is the most common of electrode materials. It is cheap, and chemically and electrically compatible with the electrolyte. Beside their high surface area, the pore diameter of electrodes is very important for achieving high capacitance. It has been reported earlier that in order to use all the pores effectively, the pore size should be double that of ions [57]. Hence the ions can move freely in and out of the pores, resulting in high charge storage. Thus, the size and distribution of pores play a significant role in achieving high capacitance [13][57]. Pyun et al. reported that EDLC performance



depends on the pore size distribution, and that smaller pore sizes cause a higher time constant due to slow ion penetration into pores compared to electrodes with large pores [58].

Energy storage capacity is determined both by the electrochemical window of the electrolyte, which determines the maximum voltage, and the capacitance, which depends mainly on the electrode. The electrolyte is made up of solvent and ions. The most common electrolytes are aqueous and organic electrolytes. The conductivity of the electrolyte affects the ESR of the supercapacitor. An increase in ionic conductivity decreases the ESR of the device. The electrolyte determines the voltage window of the supercapacitor, which limits the cell voltage and the energy storage capacity of the device. The working voltage window of aqueous electrolytes is 1 V–1.3 V and organic electrolytes is from 2.5 V–3.3 V [20] [59]. Because of higher maximum voltage, many manufacturers prefer organic electrolyte supercapacitors. Propylene carbonate and acetonitrile are common solvents used in organic electrolytes. Organic electrolytes yield ionic conductivity in the range of 10–60 mS cm<sup>-1</sup>. On the other hand, aqueous electrolytes are cheap and easier to fabricate than organic electrolytes, which need an inert atmosphere for fabrication. Aqueous electrolytes can be acidic, alkaline, or neutral [13]. The ionic conductivity of 1 M NaCl solutions is about 80 mS cm<sup>-1</sup> [60].

A separator is inserted between two electrodes to prevent the device from short circuiting. The separator should be porous and should allow the ions to pass through it. It should be flexible, light, have high ionic conductivity when impregnated with electrolyte, and be thermally stable. The different separators available for the supercapacitor are cellulose fibers and polymers such as polyethylene and polyimide [20].

### 3.1.1 Current collector

The polyethylene terephthalate aluminum foil (PET/Al) was used as a substrate in **Publications I and II**. In this case the aluminum current collector has very low resistance and is compatible with the organic electrolyte, propylene carbonate (PC). In **Publication III**, aluminum foil (Alpha 897) was used as an anode. This foil was etched and has a porous surface. The deposition of polymer PEDOT: PSS Poly(3,4-ethylenedioxythiophene) polystyrene sulfonate on the foil acts as a counter electrode. In **Publication IV**, polyethylene terephthalate (PET) was used as substrate. The coating of graphite ink Acheson PF407C on PET acts as a current collector. The advantage of this

substrate is that it prevents corrosion with an aqueous electrolyte, which was observed in the case of an aluminum current collector.

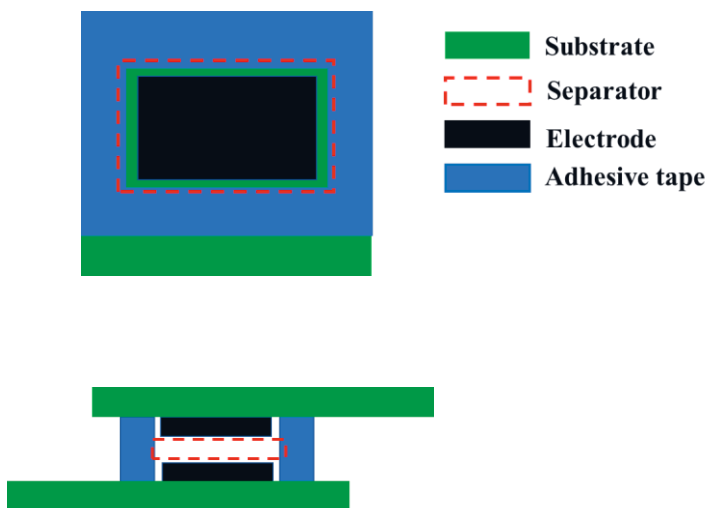


Figure 12. Schematic drawing of the electrode top view and a cross-section of the entire device.

### 3.1.2 Electrode

In the supercapacitors described in **Publications I–II**, commercially available Timcal Super P carbon black was used to formulate electrode ink. The desired capacitance with this electrode material was in the range of 3–4 mF to provide sufficient energy for BLE transmission, while maintaining an ESR of not over 1–2 Ohm to provide sufficient peak power. Due to the low specific surface area of about 62 m<sup>2</sup>g<sup>-1</sup>, carbon black leads to devices with lower capacitance. In the case of high capacitance applications, activated carbon (AC) ink is the better choice with 1500–2000 m<sup>2</sup>g<sup>-1</sup> specific surface area [61].

For the electrolytic capacitors, the conducting polymer poly((3,4-ethylenedioxythiophene) polystyrene sulfonate) PEDOT: PSS was used as one electrode, while the etched and oxidized Al surface served as the other, as described in **Publication III**. The specific capacitance of the device was 1 μFcm<sup>-2</sup>, allowing for the printing of capacitors that can be used in low pass filtering and energy storage. The graphite ink Acheson PF407C was used as an electrode in the supercapacitor described in

**Publication IV.** These supercapacitors were integrated with a piezoelectric transducer for the storage of harvested energy.

### 3.1.3 Electrolyte

The supercapacitors described in **Publications I–II** use an organic electrolyte made up of 1 M tetraethylammonium tetrafluoroborate (TEABF<sub>4</sub>) in propylene carbonate. The supercapacitors reported in **Publication IV** use 1 M sodium chloride in deionized water. The choice of electrolyte depends on the application. The most common organic electrolyte solvents are propylene carbonate and acetonitrile, and the most commonly used salt is tetraethylammonium tetrafluoroborate. Aqueous electrolyte solutions are strong acids and bases such as sulfuric acid (H<sub>2</sub>SO<sub>4</sub>), potassium hydroxide (KOH), and neutral salts such as sodium chloride (NaCl) and potassium chloride (KCl) [54] [62].

As mentioned above, in many commercial supercapacitors the use of organic electrolyte is preferred, due to the larger voltage window of 2.5–3.3 V [31][59]. The energy storage capacity in supercapacitors is proportional to the square of the voltage. Hence, electrolyte selection affects the energy density of the supercapacitors [63]. PC electrolyte is easily available and is thermally stable, safe, and inexpensive. The reported melting point of PC is -48 °C [64]. On the other hand, aqueous electrolyte provides higher ionic conductivity, environmental friendliness, non-flammability, and low cost, but it is limited to voltage between 0.6–1.4 V [62][63]. The organic electrolyte requires preparation in an inert atmosphere (glove box) to eliminate moisture, as moisture would lead to side reactions when the electrochemical window of water is reached [20].

### 3.1.4 Separator

A separator is a physical barrier that is inserted between the electrodes to prevent electrical shorting. It should have a porous structure, be wettable, flexible and non-flammable, and have good ionic conductivity when impregnated with electrolyte. The most commonly used separators reported are paper separators consisting of cellulose fibers, and polymer separators such as polypropylene, polyethylene, or polyethylene terephthalate [65][66]. Dreamweaver silver AR40 cellulose paper was used in **Publications II** and **IV**. In **Publication I**, Dreamweaver titanium 40 cellulose paper was used. The thickness of the paper was 40 µm.

## 3.2 Device fabrication

The devices described in this thesis were printed with the doctor blade coating method. The doctor blade coating, or the rod or bar coating method is simple, easy to operate, and inexpensive to use. It can provide a wide range of electrode thicknesses. In our device, the wet thickness of the printed layer was between 40–100  $\mu\text{m}$ . The fabrication process using this technique had been reported earlier [4][67][68]. It produces films with thickness typically in tens of micrometers, depending on mask thickness. In this method, as the blade rod moves, the ink is spread over the mask and the layer is printed on the substrate. Figure 13 shows a schematic drawing of the doctor blade coating method. When this coating process is used in conjunction with a patterned mask, as done in this work, it is often called stencil printing. In addition to stencil printing, other common ways of device fabrication include screen printing [69][70], inkjet printing [71], flexographic printing [72], gravure printing [73], sputtering [74], photolithography [75], and spray coating [10].

After printing the electrode layer, the drying of the electrode can be done with an oven or at room temperature. The curing temperature for supercapacitors was 80 °C and 130 °C for polymer electrolytic capacitors.. Curing or drying removes the remaining solvent or water from the printed film. In **Publications I** and **II** the assembling of the device was done inside a glovebox under an inert atmosphere, because PC electrolytes are sensitive to moisture. In **Publications III** and **IV**, the assembling of the device does not need an inert environment. In **Publications I, II** and **IV**, supercapacitors were assembled in a face-to-face configuration by sandwiching the top and bottom electrodes with separators in between. Finally, heat sealing or adhesive tape was used to seal the device. In **Publication III**, we made a stacked layer electrolytic capacitor device. It consists of anodized Al foil (Alpha 897) as anode and polymer PEDOT: PSS printed on top as a cathode, and finally current collector graphite ink is printed on polymer. Figures 13 and 14 show a schematic drawing of the doctor blade coating and photographs showing the screen-printing method, respectively.

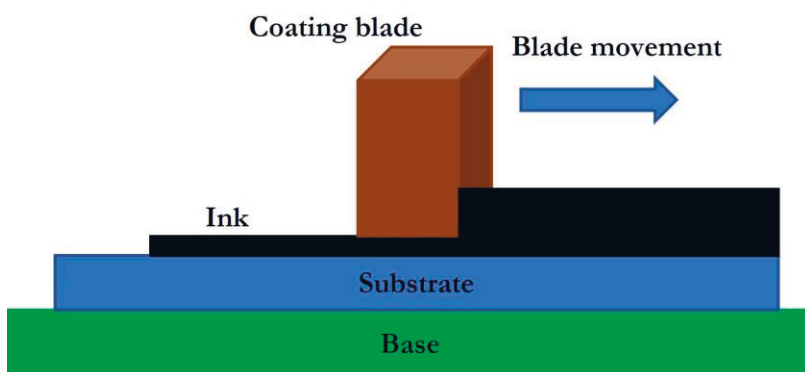


Figure 13. Schematic representation of the doctor blade coating.

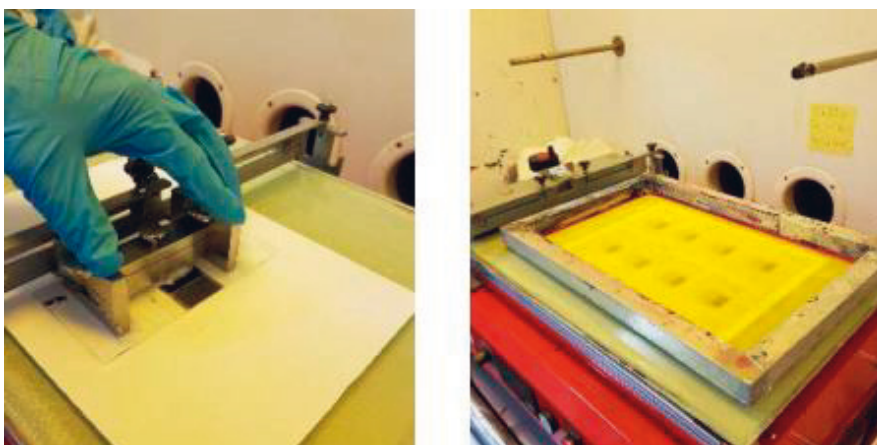


Figure 14. Setup of blade coating (left) and screen printing (right).

### 3.3 Device characterization

Common methods for characterizing the device are cyclic voltammetry (CV) and galvanostatic charge-discharge (GCD) measurement. CV is a widely used electrochemical characterization technique. In CV the electrode potential is increased linearly as a function of time to the maximum value and is swept back to the original value in the opposite direction, and the resulting current is measured. The area of the CV curve is used to calculate the capacitance of the supercapacitor [76]. Ideal supercapacitors have a rectangular CV curve, but in real devices the curve is inflected due to the resistance of the device. Capacitance is calculated by dividing current by scan rate. The value of current is taken from the discharge curve. Another method for determining the capacitance value

is the total charge of the device divided by the voltage. The total charge of the device is measured by integrating the current with respect to the time [62].

GCD is an established method for determining the capacitance and ESR of the supercapacitor. It forms the basis of industrially approved standards such as IEC 62391-1 [20][77] and ISO 8894 [54] for devices and prototypes. The supercapacitor is charged with a constant current and the output voltage is measured.

The device characterization with a Maccor 4300 unit has been reported earlier [4] [25] [63] to calculate capacitance, ESR, and leakage current. The supercapacitors charged and discharged three times between 0 and maximum cell voltage with constant current. Then, the device voltage was kept constant for 30 mins at maximum voltage and later the device was discharged with constant current. The voltage drops occurred immediately after the discharge, followed by the liner slope and this voltage was calculated from the slope with the MATLAB program. The ESR was determined from the voltage drop at the beginning of the discharge process. The ESR value was calculated by dividing voltage drop by change in current, as shown in Equation 5. Figure 15 is an example of galvanostatic discharge showing the IR drop of the device.

$$ESR = \frac{\Delta V}{\Delta I} \quad (5)$$

Where  $\Delta V$  is voltage drop and  $\Delta I$  change in current.

The device capacitance is determined from two points of the discharge curves using the IEC standard [77]. The points are selected at capacitor voltage of 40% and 80%. The expression for capacitance is described in Equation 6.

$$C = I * \frac{t_2 - t_1}{V_1 - V_2} \quad (6)$$

where  $t_1$ ,  $t_2$ ,  $V_1$  and  $V_2$  are the time and voltage at points 1 and 2 on the discharge curve.

To measure the leakage current, the maximum cell voltage is applied to a device constantly for an hour. Then, the float current to maintain that voltage level is reported as leakage current. Cell voltage in the case of aqueous electrolyte is 1.2 V and with organic electrolyte 2.5 V. Keskinen et al. reported that better encapsulation and robust sealing of a device can reduce the leakage current by 50%, from 10–20  $\mu A$  to 2–10  $\mu A$  [4].

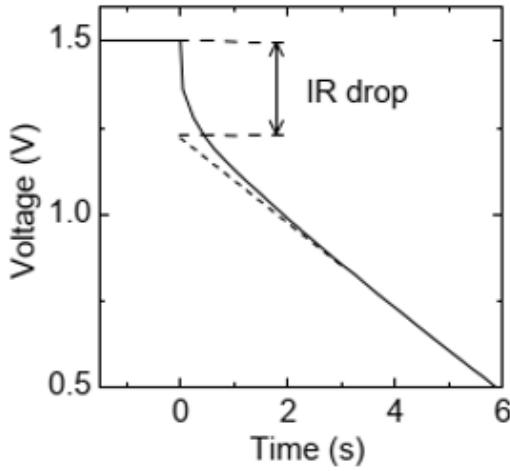


Figure 15. An example of Galvanostatic discharge to measure IR drop value.

Self-discharge leads to undesired energy loss in electrochemical supercapacitors. The self-discharge rate can be defined in the following way. The device is fully charged for a specified time, normally from 24 to 72 hours or longer for reliable data. After it is fully charged the device is disconnected, then the output voltage is measured at different time intervals to record the decay voltage. The possible causes of self-discharge are impurities in the electrolyte solution causing electrochemical reactions, ohmic leakage, redox reactions, and overcharge voltage [78]. The self-discharge rate depends on the charge duration of the device. A longer charging time reduces the voltage decay because the electrode surface charges uniformly and ions can evenly penetrate through pores [79]. Keskinen et al. observed similar voltage decay behavior of the device over time as reported in [79]. In addition, the authors of article [4] found that this decay is linear due to Faradaic reactions. A possible reason is contamination of materials during printing, drying, and assembly in ambient air [4].

### 3.3.1 Cyclic voltammetry

CV measurement was performed to measure the capacitance of the devices with a Zahner Zennium potentiostat. In CV, the potential increases over time and when the set potential is reached, it decreases in the reverse direction. The current during the anodic and cathodic sweep is recorded [62][66]. An example of the CV curve sweeps is shown in Figure 16(a). The shape of a CV curve is similar at given scan rates between

10–80 mVs<sup>-1</sup>. The plot of voltage vs. time at a constant current of 1 mA, 3 mA, and 10 mA is shown in Figure 16 (b).

The capacitance value was calculated using Equations 7 and 8.

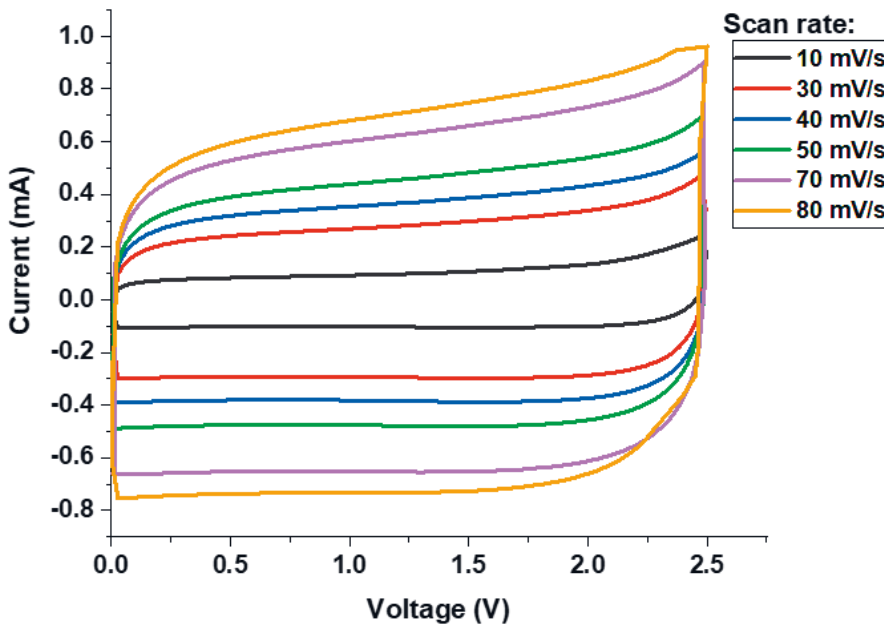
The current needed to increase the voltage with the rate of dV/dt for a capacitor with capacitance C is

$$I(t) = C \frac{dV}{dt} \quad (7)$$

The expression for the capacitance is

$$C = \frac{I}{dV/dt} \quad (8)$$

a





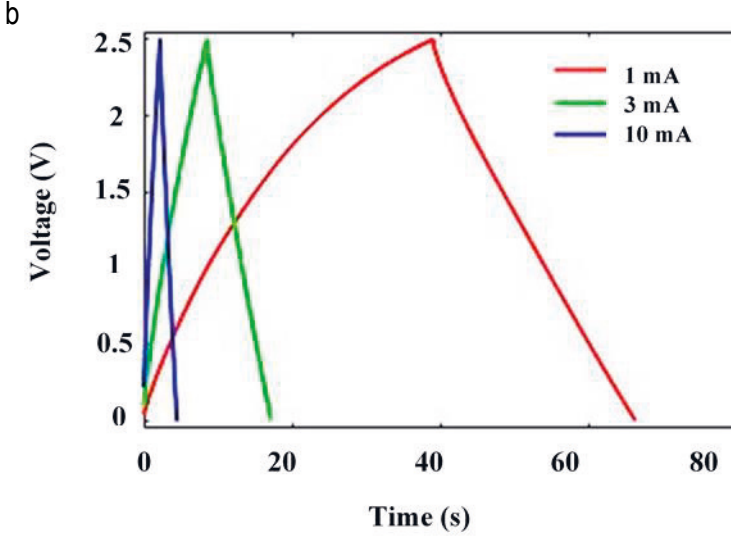


Figure 16. An example of CV measurements of the supercapacitors (a), and constant current charge-discharge measurement (b).

### 3.3.2 Electrochemical impedance spectroscopy

EIS is used for characterization of the supercapacitor or electrochemical cells. With EIS, we get information about device capacitance and impedance and can construct Bode and Nyquist plots. The use of EIS measurement has been reported earlier [80][81][82].

In this method a small alternating voltage  $v(t)$  of 10 mV amplitude is applied to the device, and output current is measured. The excitation frequency of the input voltage is between 1 Hz - 1 MHz. The voltage-current relationship is given by Equation 9.

$$v(t) = Zi(t) \quad (9)$$

where  $Z$  is the complex impedance.

For a Nyquist plot of the device as shown in Figure 17, the complex impedance  $Z$  consists of a real part and an imaginary part. The equation for the magnitude of the complex impedance is given by Equation 10.

$$Z = \sqrt{Z'^2 + Z''^2} \quad (10)$$

where  $Z'$  is the real part, referred to as equivalent series resistance (ESR), and  $Z''$  is the imaginary part of the impedance.

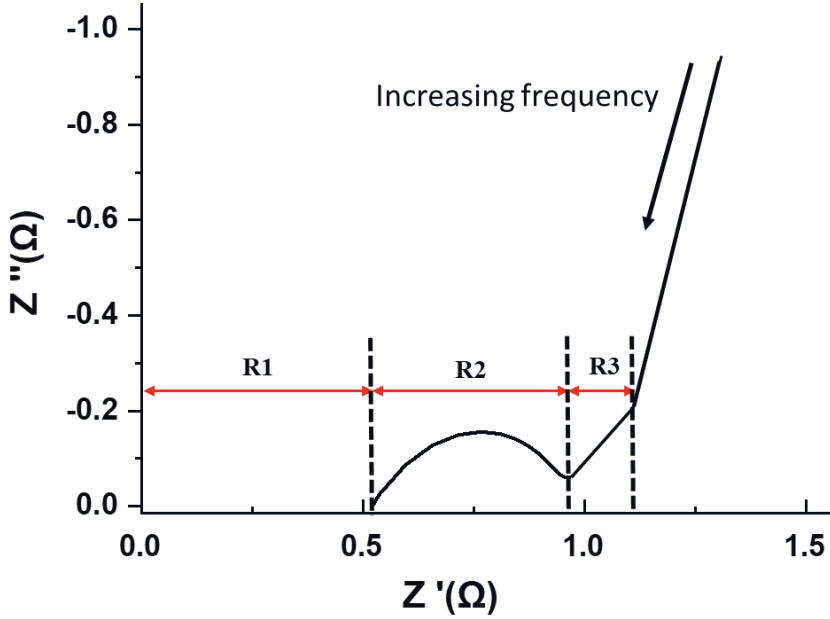


Figure 17. An example of a Nyquist plot. Adapted from **Publication II**.

The parameters defining the ESR of the devices were  $R_1$ ,  $R_2$  and  $R_3$  as shown in figure 17. The resistance  $R_1$  (left most intersect of  $Z'$ ) includes the total resistance of current collectors and ionic resistance in the separator region.  $R_2$  (width of the semicircle) describes the resistance of porous carbon electrode as well as the electrolyte inside the pores. A slope of about  $45^\circ$  is observed at low frequency, called the Warburg diffusion region [83] and  $R_3$  is the distributed resistance in the Warburg diffusion region due to mass transport of ions. (Discussion with Kai Vuorilehto, pre-examiner)

### 3.3.3 Leakage current measurement

The industrial standard IEC 62391-1 [77] was used to determine the leakage current. The supercapacitors were charged to the maximum voltage value depending on organic or aqueous electrolyte for 24 hours. A float current to balance the voltage level in supercapacitors was measured; this is the leakage current. The Faradaic charge-transfer reactions at the electrodes may cause small residual leakage current due to impurities. The impurities that are frequently found in carbon materials may be transition metal ions.

Final assembly of these devices in a glove box and robust sealing are very important to prevent water or oxygen from entering the devices.

## 4 RESULTS AND DISCUSSION

The aim of the research was to develop a flexible energy storage device and, in parallel, to integrate it with energy harvesters to operate low power flexible electronics. Based on the specification required by the project (capacitance a few mF, ESR 1-2 Ohm, for powering a Bluetooth Low Energy transmission), the target was to develop a supercapacitor module that can store sufficient energy for power peaks based on input of 3.7 V from a micro battery. Initially, we investigated the effect of varying the materials for different parts of the device, such as electrode, electrolyte and current collector. Electrode inks were formulated from activated carbon (AC), and carbon black (CB), as well as composites of both. Because of the choice of PC as electrolyte in order to achieve 2.5 V/cell, new inks had to be reformulated based on binders that do not dissolve in PC; earlier inks used in the group used chitosan as binder, which is not stable in PC. Several different binders were tried but CMC was found to produce inks with the appropriate behavior for printing or coating and to lead to good quality electrode films. The AC increases the capacitance due to surface area, while carbon black increases conductivity. It was found that even relatively small amounts of AC ink give higher capacitance than desired, due to its high specific area. Thus, the pure carbon black ink yielded both capacitance and ESR meeting the target values. Because of the goal of using low-cost current collectors on polymer film, the two feasible options were Cu and Al-PET laminates. The Cu was corroded by the electrolyte, while the Al remained intact, therefore it was used in subsequent experiments.

### 4.1 Substrate and current collector

In **Publications I–IV**, we always used flexible substrates and current collectors. The requirements were that they needed to be environmentally friendly, low cost, and meet the required specifications. For a wireless application like BLE transmission, the ESR should be no more than a few ohms to prevent unwanted voltage drop. The required peak power is in the mW range for a duration of 10 ms. In **Publications I and II**, we are targeting an ESR of 1–2  $\Omega$ , as the supercapacitor module is expected to power a BLE transmission. Thus, a metal current collector with high conductivity is needed. Graphite

is not sufficiently conductive, therefore Al and Cu were used. We found that the propylene carbonate electrolyte corrodes the Cu layer, so Al was a better option. Table 6 shows the electrical parameters of the devices reported in the publication. A photograph of a dual cell supercapacitor with PET/Al laminate and Al foil (Alpha 897) used in actual devices is shown in Figure 18.

Table 6. Electrical parameters of the capacitors reported in the publications.

Device	Substrate	Current collector	Capacitance	ESR ( $\Omega$ )	Leakage current ( $\mu\text{A}$ )
Dual cell supercapacitor	PET/Al	Al	3–4 mF	1.8–3	0.1–0.3
Single cell supercapacitor	PET/Al	Al	8–10 mF	1–2	0.1–0.4
Polymer electrolytic capacitor	Al foil	Al	10–14 $\mu\text{F}$	9	0.2
Graphite supercapacitor	PET	Graphite	10–33 $\mu\text{F}$	7–10	0.3



Figure 18. Dual cell supercapacitor made on PET/Al laminate (left), adapted from **Publication I** and Al foil Alpha 897 (right).

In **Publication III**, Al foil Alpha 897 (TDK) with a thickness of 85  $\mu\text{m}$  was used as anode. The anode plate has a high surface area obtained by electrochemical etching. In addition, the dense oxide layer on top of the foil is added by anodizing and acts as the capacitor dielectric [13]. The thickness of the oxide layer was about 300 nm and determined by the supplier by electrochemical anodization method. The SEM image of the cross-section and surface structure of the foil are shown in Figure 19.

PET was used as a substrate and graphite as a current collector in **Publication IV**. The ESR is measured with the help of electrochemical impedance spectroscopy. The ESR of the devices comes from electrolyte resistance, contact resistance, and diffusion resistance. The Nyquist plot of real and imaginary impedance measured and fitted is shown in Figure 20. The ESR value of the laminated PET/Al reported in **Publications I** and **II** is lower than obtained for the capacitor using graphite as current collector.

The ESR of the devices is limited by the current collector, electrolyte, and contact resistance between the electrode and the current collector. The PET/Al metal current collector gives lower ESR values than the graphite-coated PET current collector. The ESR varies due to the use of different materials in the devices. From the Nyquist plot of the single cell supercapacitor as shown in Figure 17, the measured electrolyte resistance was about  $0.51\ \Omega$  (R1), contact resistance between current collector and the electrode was about  $0.4\ \Omega$  (R2), and the distributed resistance was  $0.21\ \Omega$  (R3). DCSCs have higher ESR than a single cell because the total ESR is the sum of individual cells' ESR. On the other hand, the ESR of a polymer electrolytic capacitor is  $9\ \Omega$  and is mainly due to the coated PEDOT: PSS and graphite ink on top of the Al foil.

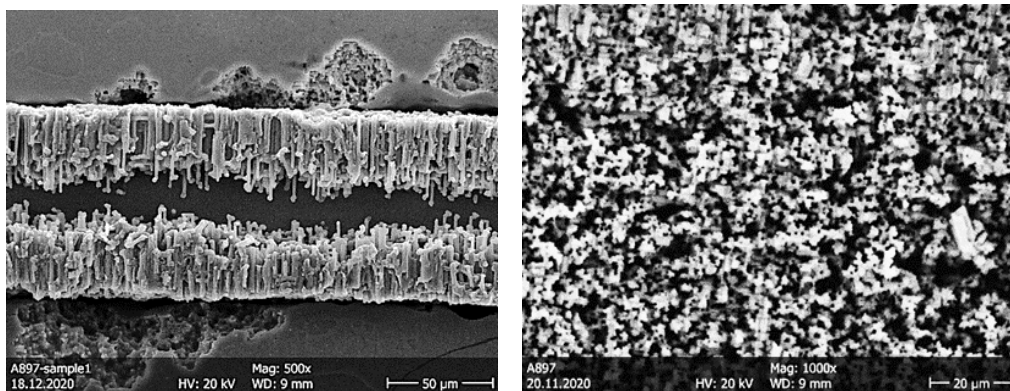


Figure 19. Al foil cross-section (left) and surface structure (right). Adapted from **Publication III**.

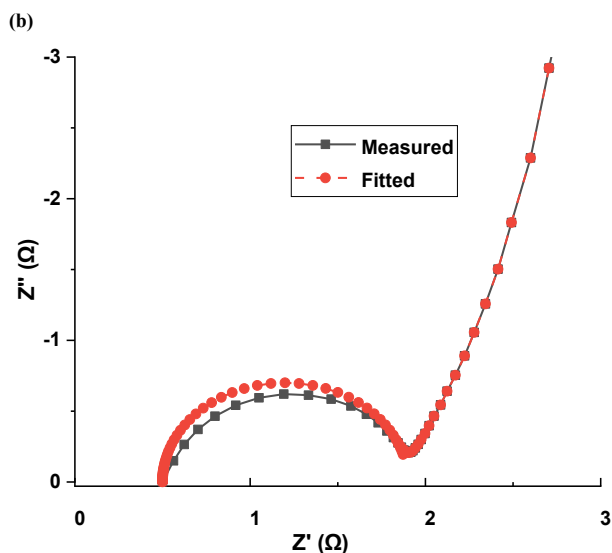


Figure 20. Nyquist plot of real and imaginary impedance (measured and fitted). Adapted from **Publication I**.

## 4.2 Electrode materials

The electrode materials used in this work were based on activated carbon (AC) and carbon black (CB), as well as composites of both materials. The device with an all-AC electrode gives very high capacitance, due to its high surface area ( $>100 \text{ mF}$ ) and excessively high ESR due to its low conductivity, thus did not meet the targeted specifications for the project in which the work was performed. Composites were also unable to meet the specifications. The best combination of low capacitance and low ESR was achieved using an ink formulated from CB. While chitosan was used as a binder in aqueous supercapacitors, this was not possible in devices using propylene carbonate as electrolyte; therefore, new inks needed to be formulated. The best binder for the purpose was found to be carboxymethyl cellulose (CMC). The electrode materials contribute to the device's capacitance, peak power, and energy storage capacity. Electrodes should be porous with a high specific surface area. In **Publications I, II, and IV**, the supercapacitors were assembled in a face-to-face configuration as shown in figure 12. In **Publication III**, the capacitor consists of a stacked structure printed layer by layer on a single substrate, as shown in Figure 21. Table 6 shows the electrical parameters of the devices reported in the publications.

**Publication I** mainly focuses on material selection, design, and scaling of DCSCs for energy storage. Reliability studies of these devices in different environments were performed in **Publication II**. The device fabricating process is similar in **Publications I and II**. Super P carbon black bound with carboxymethyl cellulose (CMC) was used as an electrode. The carbon particle size is about 40 nm, given in manufacturer datasheet. The amounts of carbon black and binder were 90 wt% and 10 wt% respectively. The wet thickness of the electrode layer was 100  $\mu\text{m}$ . The specific area of the electrode is less than that made using AC ink. Thus, this carbon black is suitable for achieving capacitance of only a few mF, as targeted for the specific application. The water-based CMC binder is a good choice, and good adhesion was obtained between the electrode and the current collector. Another advantage was compatibility with PC electrolyte. The PC electrolyte's voltage window was 2.5 V/cell. The device can be scaled from single cell to multi-cell, depending on the application.

In **Publication III**, the commercial conductive polymer PEDOT: PSS (Heraeus Clevis SV4) was used as a counter electrode. This polymer is highly conductive, transparent, and has excellent stability. Because of these advantages, it is widely used in commercial electrolytic capacitors for filtering and coupling applications [84] [85]. The initial idea for studying these polymer electrolytic capacitors was as an alternative option to the supercapacitors, which is to provide power peaks to BLE transmission. However, the devices give very low capacitance in the  $\mu\text{F}$  range rather than a few mF, and thus were not able to power a transmission. The specific capacitance of the printed devices was 1  $\mu\text{Fcm}^{-2}$ , which is close to the nominal value as specified by the supplier. The CV measurement of the device is shown in Figure 22. Furthermore, we demonstrated some practical applications of these capacitors such as resistor-capacitor (RC) filtering at about 1.03 kHz frequency and storage. The capacitance of the polymer electrolytic capacitor is less than that of the supercapacitors in the other publications. This is not surprising, since the dielectric thickness is ca. 300 nm as explained above, compared to the extremely thin ionic double layer in supercapacitors.

**Publication IV** reports on supercapacitors based on the commercial graphite PF407C ink used as an electrode, PET as a substrate, and NaCl as an electrolyte. The thickness of graphite was 40  $\mu\text{m}$ , and was printed on the top of PET. Here, we connected five aqueous supercapacitors (1.2 V/cell) to accommodate the relatively high voltage generated by the piezoelectric transducer. The characterization of the flexible piezoelectric transducer (PVDF:TrFE) was done with a 4810 BRÜEL & KJÆR mini shaker. The maximum



dynamic sensitivity ( $\text{pC/N}$ ) piezoelectric transducer was  $24.41 \pm 3.2$  in normal mode and  $286 \pm 52$  in bend mode. The piezoelectric transducer was used as an energy harvester and integrated with rectifier circuit and storage unit. The details are explained in section 4.3.

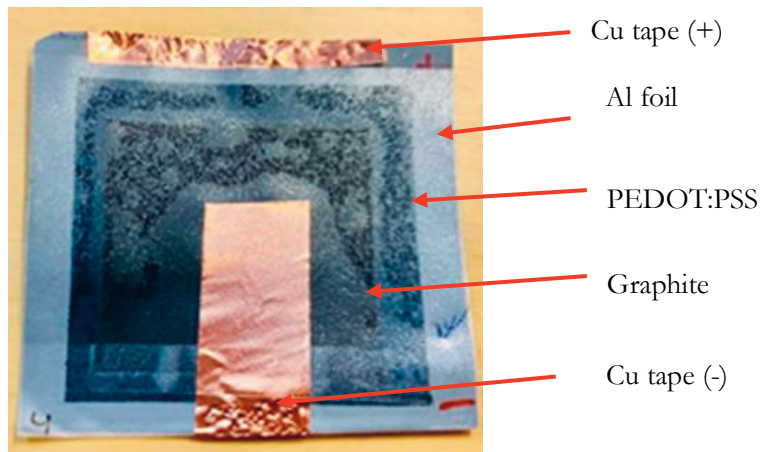


Figure 21. Polymer electrolytic capacitor. Adapted from **Publication III**.

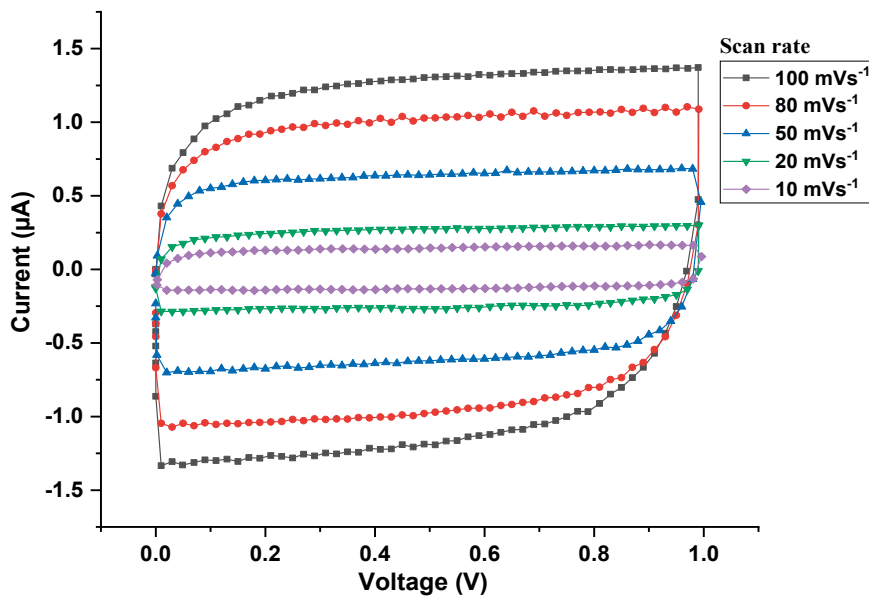


Figure 22: Cyclic voltammetry graph. Adapted from **Publication III**.

### 4.3 Ambient energy harvesting

There are two main types of energy harvesting methods studied in this research. The first one is motion energy harvesting from piezoelectric polymers (**Publications III, IV**) and the second one is light energy harvesting (**Publication I**) using OPV. The publications report the amount of energy generated and their possible applications in low-power electronics in more detail, but the key results are summarized here. A photograph of the piezoelectric transducer used in this study is shown in Figure 23. Table 7 shows the details of the energy source and the amount of energy harvested.



Figure 23. Piezoelectric transducer.

The amount of stored energy depends on the capacitance and voltage. To maximize the energy, both the voltage and capacitance value should be high. On the other hand, an excessively large capacitance could make it difficult to fully charge the device, especially from weak energy sources. The maximum energy generated was 39 mJ, as reported in **Publication I**. This energy was harvested from indoor lighting. The Infinity OPV module was used as an energy harvester and dual cell supercapacitors as an energy storage device. The harvester uses an energy harvesting chip (Epeas AEM10941) that advances the energy storage efficiency of the supercapacitor and maintains the voltage level at 4.5 V. The energy harvested in DCSCs is enough to power a BLE module for 10 ms. The energy harvesting setup is shown in Figure 24 and the plot of voltage as a function of time across the supercapacitor is shown in Figure 25.

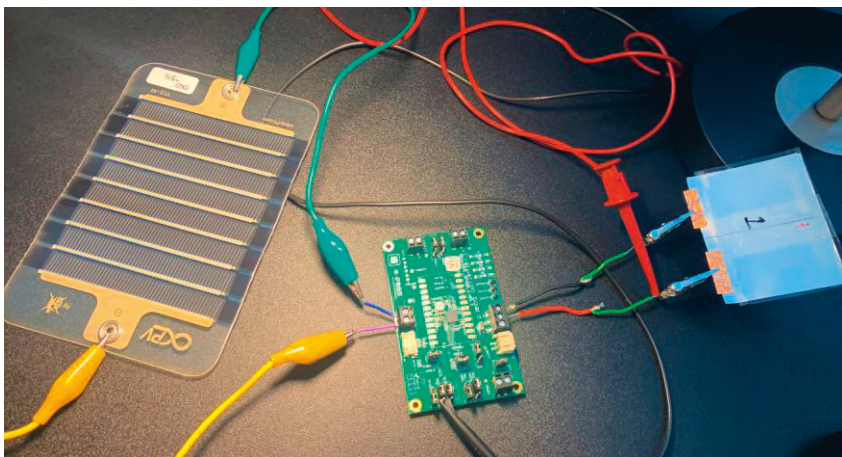


Figure 24. Integration of OPV, IC, and supercapacitor. Adapted from **Publication I**.

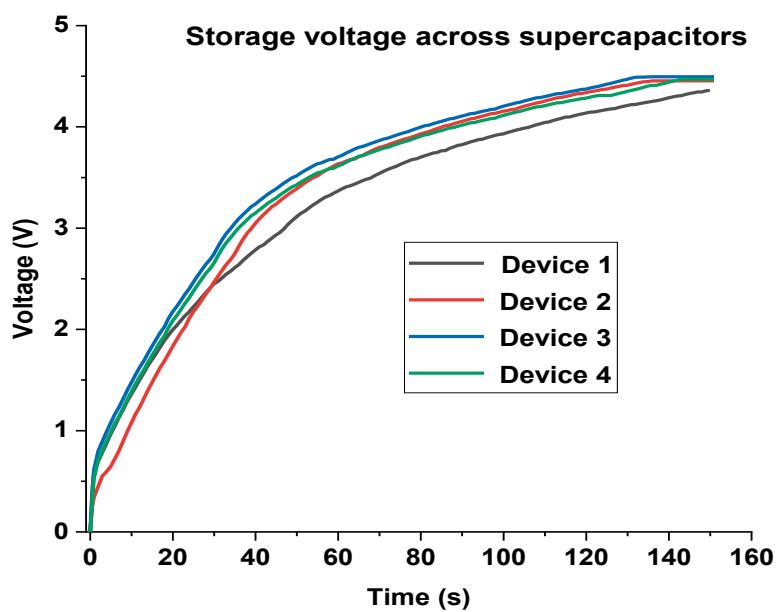


Figure 25. Voltage measurement across the dual cell supercapacitors as a function of time. Adapted from **Publication I**.

In **Publications III** and **IV**, a piezoelectric transducer from Joanneum Research Center was used as an energy source; the device fabrication process was reported earlier [44] [86]. The polymer electrolytic capacitor from **Publication III**, commercial electrolytic capacitors, and graphite supercapacitors from **Publication IV** were used as energy storage devices. The amount of energy harvested and stored in these devices was studied. As the aqueous graphite supercapacitors have a maximum voltage of 1.2 V, five supercapacitors were connected in a series to achieve higher voltage, but this will automatically decrease the total capacitance of the device. The output current from the piezoelectric transducer is low. Due to this, we observe that it is slow to charge capacitors above 100  $\mu\text{F}$ , and even slower for mF range supercapacitors. Therefore, devices with smaller capacitance were used in further experiments. The block diagram of the energy harvesting system is shown in Figure 26. The output voltage response of the transducer and rectified voltage are shown in Figure 27. The excitation frequency of the motor striking the piezoelectric transducer is up to 50 Hz. Even at low frequency, the response of the transducer was good; output voltage shows dependency on the excitation frequency of the motor. The AC voltage is converted to DC using a bridge rectifier circuit. The capacitor charged to peak value within 60s. In the case of graphite supercapacitors, the energy storage is only 0.073 mJ because the capacitor value was only 3  $\mu\text{F}$ . On the other hand, the amount of energy harvested in both electrolytic capacitors was similar, about 1–1.12 mJ. Compared with the OPV module, energy is very low and is not sufficient to power BLE transmissions, but it can be used in other low-power devices such as a wireless transceiver operating at 67 nW of power and transmitting data at a rate of 4.8 kbps [87]. Also, these devices can play important roles in low pass filtering and smoothing purposes.

Table 7: Energy harvested, and storage reported in the publications

Energy harvester	Storage device	Capacitance value	Energy (mJ)
Piezoelectric transducer	Commercial electrolytic capacitor	22 $\mu\text{F}$	1.12
Piezoelectric transducer	Graphite supercapacitor	3 $\mu\text{F}$	0.073
Piezoelectric transducer	Polymer electrolytic capacitor	14 $\mu\text{F}$	1
OPV module	Dual-cell supercapacitor	3.9 mF	39

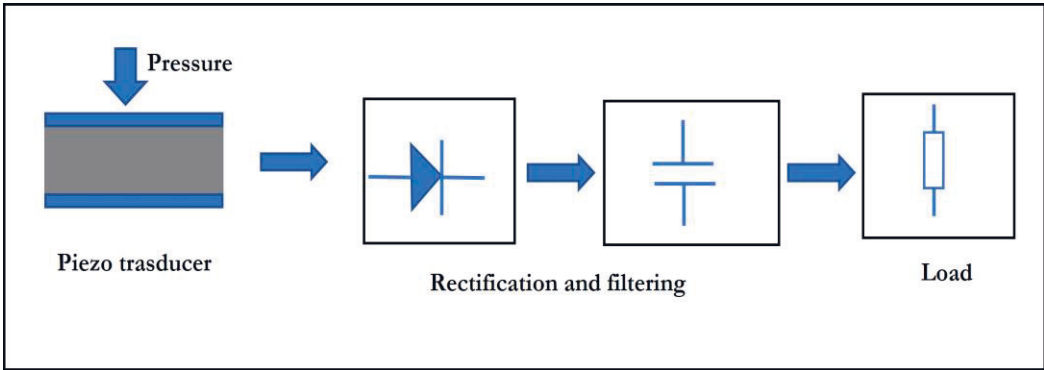
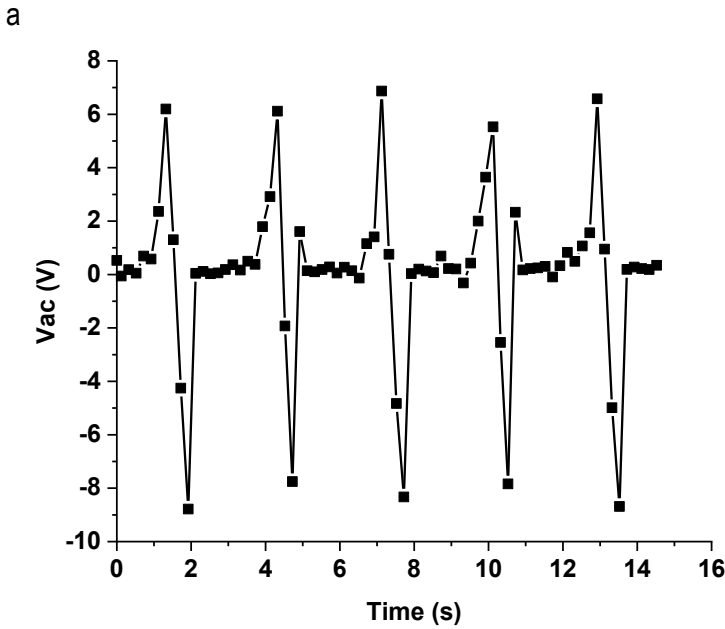


Figure 26. Block diagram of piezo energy harvesting module. Adapted from **Publication III**.



b

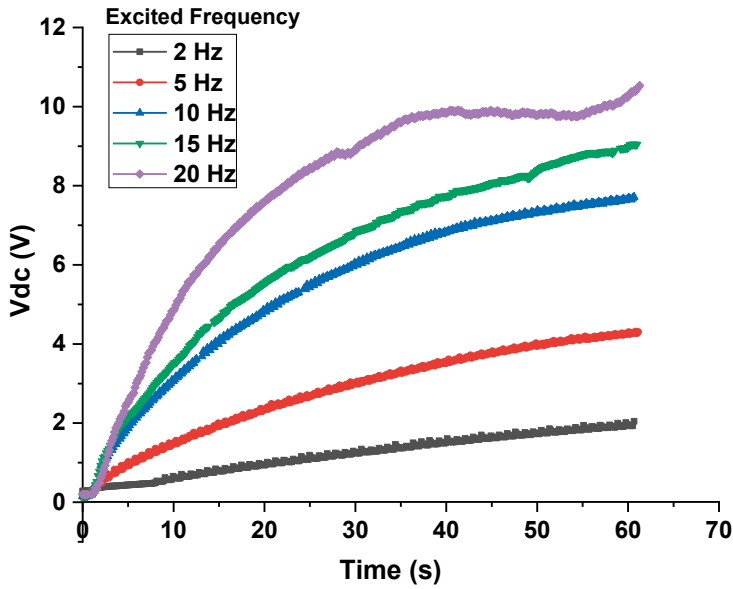


Figure 27. Output response of piezoelectric transducer (a) and rectified voltage of transducer 2 to 20 Hz (b). Adapted from **Publication III**.

## 4.4 Reliability of the devices

The mechanical, electrical, and temperature reliability of energy storage devices is very important for flexible energy storage applications. In this thesis, the devices show good flexibility and robustness under different conditions. Organic electrolyte-based printed, flexible supercapacitors were reported in **Publication I** and their reliability was investigated systematically in **Publication II**.

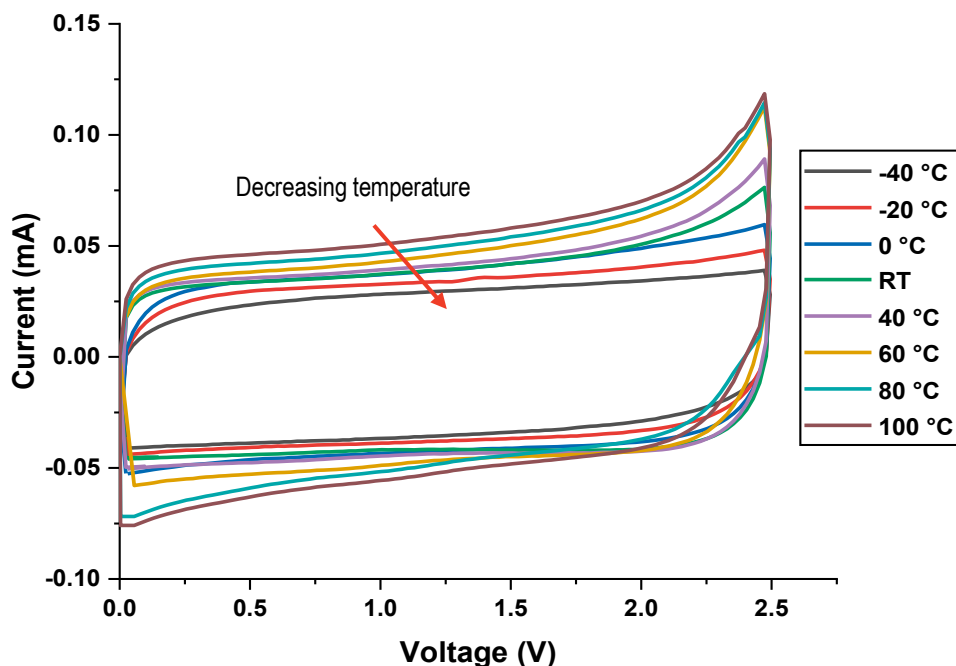


Figure 28. CV measurement of device at temperature ranges from -40 to 100 °C at a scan rate of 5 mV/s  
Adapted from **Publication II**.

The reliability of the organic electrolyte-based devices under exposure to high and low temperatures, cyclic bending, and thermal shock was studied. Figure 28 shows the CV measurement of the supercapacitors at a scan rate  $5 \text{ mVs}^{-1}$  from 0 to 2.5 V over a range of temperatures. The devices are functional at temperatures between -40 °C to 100 °C. We observed that capacitance dependence is weaker on temperature than the ESR. Next, the subzero temperature was investigated. As the temperature dropped from room temperature (RT) to -40 °C, the ESR of the supercapacitor increased from  $1.97 \text{ } \Omega$  to  $4.98 \text{ } \Omega$ . The EIS investigation shows that increased viscosity and decreased ionic conductivity caused higher ESR values. An earlier report on an aqueous 1 M NaCl-based supercapacitor shows that the devices were functional down to -15 °C [88]. Supercapacitors with organic electrolyte can be used in even colder environments. Since one of the targeted applications for the devices was integration into a smart snow ski, the improved lower temperature limit of the propylene carbonate-based devices was a substantial advantage. Next, the supercapacitors were subjected to cyclic bending. The samples were measured before and after bending at specific number of bending cycles. The capacitance retention was 100% after 10,000 bending cycles at a bending radius of 0.41 cm. The devices are functional and have no physical damage or leakage. This is

mainly due to robust sealing and the flexibility of the PET/Al. The minimum recorded bending radius was 0.41 cm, which shows enough flexibility in the device for wearable and printed electronic applications.

The supercapacitors were subjected to a dedicated climate chamber for thermal shock tests at temperatures between  $-40\text{ }^{\circ}\text{C}$  and  $100\text{ }^{\circ}\text{C}$ . The temperature change rate between minimum and maximum was  $90^{\circ}\text{C}/\text{min}$  over a cycle of approximately 30 mins. The thermal shock test shows a significant decrease in device performance after a large number of shock cycles. From EIS, we concluded that this is because of the increase in contact resistance between the electrode and the current collector. The reason for increasing contact resistance is due to micro cracks and defects on the electrode layer, as shown in Figure 29. These cracks lead to poor adhesion of electrode to the current collector. As the capacitance is proportional to the electrode area, any cracks or damages in the electrode results in a significant decrease in capacitance.

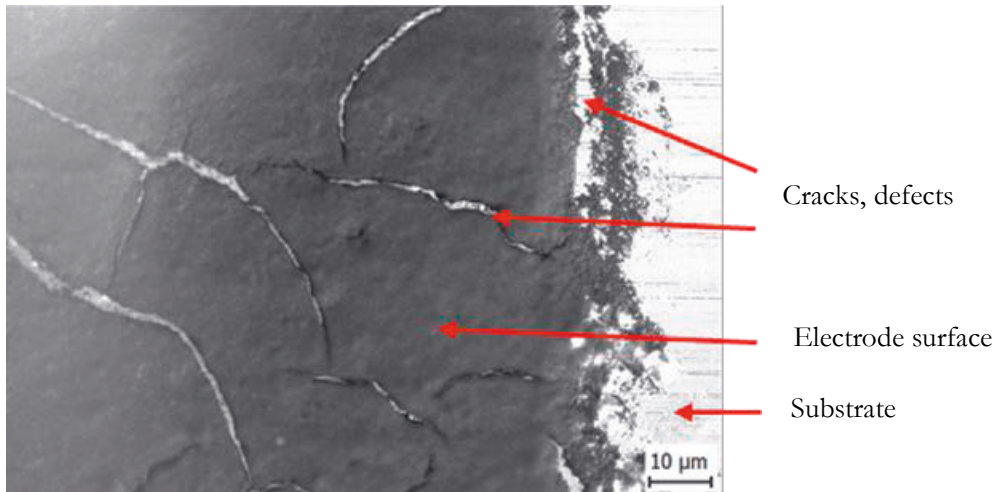


Figure 29. Microscopic image of electrode layer after thermal shock test shows defects and cracks. Adapted from **Publication II**.

A study of the temperature dependence of the printed polymer electrolytic capacitor was reported in **Publication III**. The device was subjected to a temperature range of between  $20\text{ }^{\circ}\text{C}$  and  $90\text{ }^{\circ}\text{C}$ . The shape of the CV curves shows good capacitive behavior at these temperature ranges. The area of the CV increases with increasing temperature, thus showing the increase in the capacitance value. In the polymer electrolytic capacitor, expansion of polymer PEDOT:PSS increases the contact area with Al foil, hence the increase in capacitance [89]. The flexibility of the polymer electrolytic is determined by



bending, twisting, and rolling the device. The minimum bending radius was 0.4 cm, which was identical to the supercapacitor based on carbon black and propylene carbonate. Photographs of the devices during bending are shown in Figure 30; the CV measurement is shown in Figure 31.

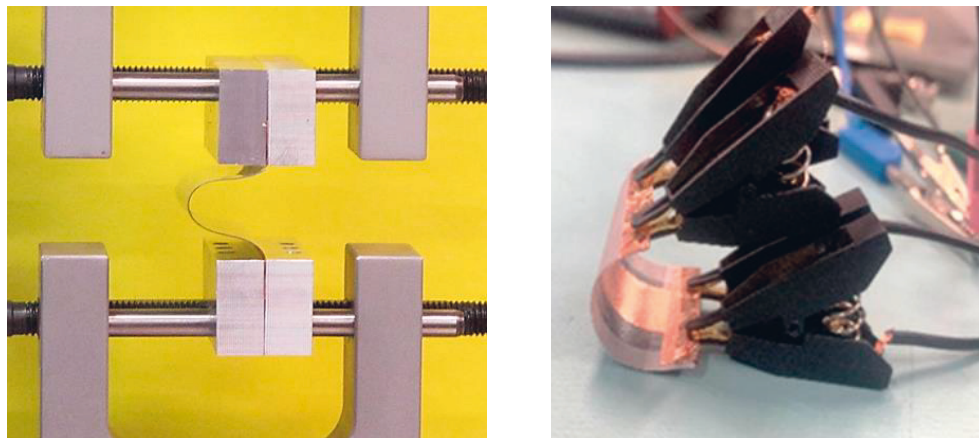


Figure 30. Photographs showing flexibility of the supercapacitor (left) and the polymer electrolytic capacitor (right). Adapted from (**Publications II, III**).

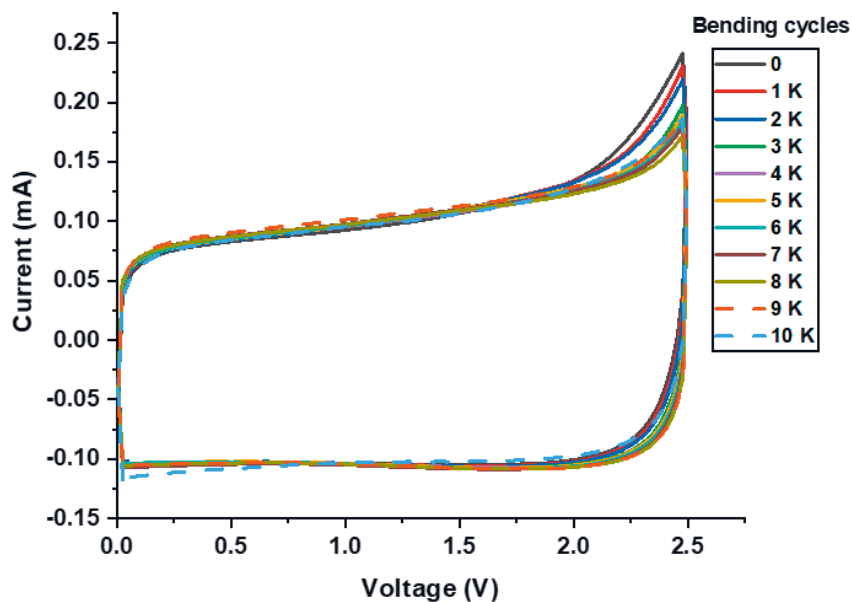


Figure 31. CV measurement up to 10,000 bending cycles of supercapacitors at scan rate of 10mV/s. Adapted from **Publication II**.

## 5 CONCLUSION

In this research work, we fabricated supercapacitors and polymer electrolytic capacitors for flexible and wearable energy storage applications. In addition, the devices were integrated with OPV and piezoelectric polymer-based energy harvesters. The results indicated that the combination of energy harvesting and interim energy storage in supercapacitors can be a suitable approach for distributed low-power electronics such as sensors and IoT devices.

Detailed study of the materials and technology was a focus of this research work. As we are focusing on printed, flexible supercapacitors in the range of a few mF, experiments were carried out initially with a wide range of carbon materials and electrolytes, in order to tune the capacitance and ESR to suitable values. Low-cost, nontoxic, and environmentally friendly materials were favored whenever possible.

The answer to research question 1 explains the choice of materials, architectures, and processes to meet the targeted electrical specifications of the devices for various applications. Based on current experiments and previously reported AC electrode-based supercapacitors show capacitance above 100 mF due to AC's high specific surface area. The use of graphite on a metal current collector showed lower capacitance but did not achieve the necessary low ESR. The laminated PET/Al metal current collector is a better choice due to lower resistance, and in addition there is no issue of Al corrosion with PC. The technical goal of the work reported in this thesis is to improve the architectural design of dual cell supercapacitors with a suitable ink electrode, electrolyte, and current collector in order to achieve capacitance of 3-4 mF and ESR below 2  $\Omega$ . Furthermore, the choice of the electrolyte in the supercapacitors helps to achieve targeted voltage for high energy storage. As a result, it was found that applying low specific area ink made of Super P carbon black and PC electrolyte resulted in the required properties. In this way device optimization and materials choice helps to achieve the desired electrical parameters.

Research question 2 asks whether the printed organic electrolyte-based supercapacitors achieve the capacitance and ESR values to power radio transmission of information from smart objects. We observed that a device can be connected in parallel with a battery or work independently for peak powering of a BLE module. We successfully achieved the

targeted capacitance and ESR value required to power radio transmission. This was demonstrated in the smart ski, where the supercapacitor acts as a secondary energy source to power a BLE, while the primary energy source was a thin-film battery. As the battery performance drops sharply below 0 °C, the supercapacitor is a critical part of the energy module to enable data transmission under cold conditions prevailing on ski slopes. The supercapacitors can be further optimized from single cells to multi-cell, depending on the targeted requirements. The supercapacitors in a multicell module are connected in series in order to achieve a higher storage voltage. A metal current collector is chosen in order to minimize the ESR. The capacitance is proportional to the electrode area, thus higher capacitance uses a large electrode area. Similarly, for large capacitance application AC ink is a better choice than carbon black. One disadvantage of metal current collectors is the possibility of corrosion with aqueous electrolyte. Also, if the ESR is not too critical, graphite can be used as a current collector with aqueous electrolyte.

Research question 3 asked about the integration of printed electrolytic capacitors with electronics circuits and their ability to act as possible energy storages. The printed electrolytic capacitors are flexible, light-weight, and can be easily integrated with a piezoelectric energy harvester module for possible energy storage of about 1 mJ. These devices can also be used in low pass filtering circuits in the 1.03 kHz range, and with a bridge rectifier circuit as a smoothing capacitor, it is possible to achieve efficiency of 81%, as demonstrated in **Publication III**.

Research question 4 is about energy harvesting and energy storage in novel devices. Therefore, we focused on the possible amount of clean energy from the ambient environment and storing it in our fabricated novel devices. The two main energy harvesting devices were OPV and a piezoelectric transducer. In **Publication I**, an energy management IC was integrated with OPV and DCSC, which have advantages like regulated power to the DCSC, charge balance across the device, increased storage efficiency, and device protection. The maximum storage voltage across the DCSC device was 4.49 V. The maximum amount of energy harvested with an OPV module from an indoor light source was 39 mJ. The harvested energy was enough to provide power peaks to energy-autonomous devices such as BLE transmission, sensors, IoT, and other low-power applications. On the other hand, with a piezo energy harvester, the maximum energy harvested was 1.12 mJ. This energy can be used to power portable devices such as cardiac pacemakers, Wi-Fi (in sleep mode), hearing aids and Bluetooth (in sleep mode).

The answer to research question 5 about the functionality of the devices under extreme environmental conditions is described in **Publication II**. The reliability test of the devices under different conditions is also an important aspect of this thesis. The temperature results show that the supercapacitor can operate in a wide temperature range of -40 °C to 100 °C. We observed an increase in the capacitance with increasing temperatures. For devices operating at subzero temperatures, the ESR is the main limiting factor. The thermal shock results in a decrease in device performance because of the micro cracks and defects in the electrode layer due to rapid temperature cycling. In terms of flexibility and robustness, the device gives 100% retention up to 10,000 cycles and the minimum bending radius was 0.41 cm, while devices can be implemented in many flexible and wearable electronics applications. Due to time limitation, the flexibility test was performed up to 10 K cycles, as explained above, and these tests showed reliable electrical performance of the device when integrated with a smart ski. Similarly, the CV curve of the polymer electrolytic capacitor indicates that these devices were stable from 20 °C to 90 °C. An increase in contact area due to thermal expansion of polymer is the main reason for capacitance increase in the device.

Thus, simple and inexpensive printing technology with novel materials was used for fabricating supercapacitors and polymer electrolytic capacitors for energy storage applications. The devices are flexible and highly reliable. They can be scalable depending on the need for storage capacity, and in the near future they may be compatible with R2R printing techniques. The polymer electrolytic capacitor in our research is limited to a few  $\mu\text{F}$  capacitance only, but in the near future this capacitance can be improved with new dielectric materials with higher dielectric constant, using atomic layer deposition. This technique can enable higher capacitance, which will make the capacitor suitable for a larger number of applications.

## REFERENCES

- [1] T. M. I. Mahlia, T. J. Saktisahdan, A. Jannifar, M. H. Hasan, and H. S. C. Matseelar, "A review of available methods and development on energy storage; technology update," *Renew. Sustain. Energy Rev.*, vol. 33, pp. 532–545, May 2014, doi: 10.1016/J.RSER.2014.01.068.
- [2] M. Aneke and M. Wang, "Energy storage technologies and real life applications – A state of the art review," *Appl. Energy*, vol. 179, pp. 350–377, 2016, doi: 10.1016/j.apenergy.2016.06.097.
- [3] K. Hung, C. Masarapu, T. Ko, and B. Wei, "Wide-temperature range operation supercapacitors from nanostructured activated carbon fabric," *J. Power Sources*, vol. 193, no. 2, pp. 944–949, 2009, doi: 10.1016/j.jpowsour.2009.01.083.
- [4] J. Keskinen *et al.*, "Architectural modifications for flexible supercapacitor performance optimization," *Electron. Mater. Lett.*, vol. 12, no. 6, pp. 795–803, 2016, doi: 10.1007/s13391-016-6141-y.
- [5] R. Zhang, Y. Xu, D. Harrison, J. Fyson, and D. Southee, "A study of the electrochemical performance of strip supercapacitors under bending conditions," *Int. J. Electrochem. Sci.*, vol. 11, no. 9, pp. 7922–7933, 2016, doi: 10.20964/2016.09.59.
- [6] S. Wang, T. Wei, and Z. Qi, "Supercapacitor energy storage technology and its application in renewable energy power generation system," in *Proceedings of ISES World Congress 2007 (Vol. I -- Vol. V)*, 2009, pp. 2805–2809, doi: 10.1007/978-3-540-75997-3\_566.
- [7] H. Moon *et al.*, "Ag/Au/Polypyrrole core-shell nanowire network for transparent, stretchable and flexible supercapacitor in wearable energy devices," *Sci. Rep.*, vol. 7, no. 1, p. 41981, 2017, doi: 10.1038/srep41981.

- [8] R. Kötzt and M. Carlen, “Principles and applications of electrochemical capacitors,” *Electrochim. Acta*, vol. 45, pp. 2483–2498, 2000, doi: 10.1057/9780230503014.
- [9] A. Wang, K. Sun, R. Xu, Y. Sun, and J. Jiang, “Cleanly synthesizing rotten potato-based activated carbon for supercapacitor by self-catalytic activation,” *J. Clean. Prod.*, vol. 283, p. 125385, Feb. 2021, doi: 10.1016/J.JCLEPRO.2020.125385.
- [10] M. Kaempgen, C. K. Chan, J. Ma, Y. Cui, and G. Gruner, “Printable thin film supercapacitors using single-walled carbon nanotubes,” *Nano Lett.*, vol. 9, no. 5, pp. 1872–1876, 2009, doi: 10.1021/nl8038579.
- [11] C. Shi *et al.*, “An ‘all-in-one’ mesh-typed integrated energy unit for both photoelectric conversion and energy storage in uniform electrochemical system,” *Nano Energy*, vol. 13, pp. 670–678, 2015, doi: 10.1016/j.nanoen.2015.03.032.
- [12] A. Nechibvute, A. Chawanda, and P. Luhanga, “Piezoelectric Energy Harvesting Devices: An Alternative Energy Source for Wireless Sensors,” *Smart Mater. Res.*, vol. 2012, pp. 1–13, 2012, doi: 10.1155/2012/853481.
- [13] D. G. W. Goad and H. Uchi, “Modelling the capacitance of d.c. etched aluminum electrolytic capacitor foil,” *Journal of Applied Electrochemistry*, vol. 30, no. 3, pp. 285–291, 2000, doi: 10.1023/A:1003527316173.
- [14] A. Yu, V. Chabot, and J. Zhang, *Electrochemical Supercapacitors for Energy Storage and Delivery*. Vancouver, BC: CRC Press, 2013.
- [15] A. González, E. Goikolea, J. A. Barrena, and R. Mysyk, “Review on supercapacitors: Technologies and materials,” *Renew. Sustain. Energy Rev.*, vol. 58, pp. 1189–1206, May 2016, doi: 10.1016/J.RSER.2015.12.249.
- [16] H. Wang and L. Pilon, “Accurate simulations of electric double layer capacitance of ultramicroelectrodes,” *J. Phys. Chem. C*, vol. 115, no. 33, pp. 16711–16719, 2011, doi: 10.1021/jp204498e.
- [17] W. Wang *et al.*, “Hierarchical core–shell Co<sub>3</sub>O<sub>4</sub>/graphene hybrid fibers: potential electrodes for supercapacitors,” *J. Mater. Sci.*, vol. 53, no. 8, pp. 6116–6123, 2018, doi: 10.1007/s10853-017-1971-z.

- [18] J. Qin, F. Zhou, H. Xiao, R. Ren, and Z. S. Wu, "Mesoporous polypyrrole-based graphene nanosheets anchoring redox polyoxometalate for all-solid-state micro-supercapacitors with enhanced volumetric capacitance," *Sci. China Mater.*, vol. 61, no. 2, pp. 233–242, 2018, doi: 10.1007/s40843-017-9132-8.
- [19] A. Borenstien, M. Noked, S. Okashy, and D. Aurbach, "Composite carbon nano-tubes (CNT)/activated carbon electrodes for non-aqueous supercapacitors using organic electrolyte solutions," *J. Electrochem. Soc.*, vol. 160, no. 8, pp. A1282–A1285, 2013, doi: 10.1149/2.103308jes.
- [20] J. Keskinen, "Supercapacitors on Flexible Substrates for Energy Autonomous Electronics," Tampere University, Tampere, 2018.
- [21] V. Augustyn, P. Simon, and B. Dunn, "Pseudocapacitive oxide materials for high-rate electrochemical energy storage," 2014, doi: 10.1039/c3ee44164d.
- [22] G. A. Snook, P. Kao, and A. S. Best, "Conducting-polymer-based supercapacitor devices and electrodes," *J. Power Sources*, vol. 196, no. 1, pp. 1–12, Jan. 2011, doi: 10.1016/J.JPOWSOUR.2010.06.084.
- [23] Y. Bai, H. Jantunen, and J. Juuti, "Energy harvesting research: The road from single source to multisource," *Adv. Mater.*, vol. 30, no. 34, pp. 1–41, 2018, doi: 10.1002/adma.201707271.
- [24] A. Riaz, M. R. Sarker, M. Hanif, M. Saad, R. Mohamed, and C. K. Jeong, "Review on Comparison of Different Energy Storage Technologies Used in Micro-Energy Harvesting, WSNs, Low-Cost Microelectronic Devices: Challenges and Recommendations," 2021, doi: 10.3390/s21155041.
- [25] M. Arvani *et al.*, "Flexible energy supply for distributed electronics powered by organic solar cell and printed supercapacitor," in *Proceedings of the IEEE Conference on Nanotechnology*, 2020, vol. 2020-July, doi: 10.1109/NANO47656.2020.9183493.
- [26] I. Arbouch, Y. Karzazi, and B. Hammouti, "Organic photovoltaic cells: Operating principles, recent developments and current challenges – review," *Phys. Chem. News*, vol. 72, no. 4, pp. 73–84, 2014.
- [27] S. Najam and B. Kumar, "Organic Solar Cell: Operating Principle, Performance Parameters, Structures and Its Advantages," *2018 5th IEEE Uttar Pradesh Sect. Int. Conf. Electr. Electron. Comput. Eng. UPCON 2018*, pp. 5–10,

2018, doi: 10.1109/UPCON.2018.8597120.

- [28] T. D. Nielsen, C. Cruickshank, S. Foged, J. Thorsen, and F. C. Krebs, “Business , market and intellectual property analysis of polymer solar cells,” *Sol. Energy Mater. Sol. Cells*, vol. 94, no. 10, pp. 1553–1571, 2010, doi: 10.1016/j.solmat.2010.04.074.
- [29] B. Pozo, I. Garate, Á. Araujo, and S. Ferreira, “Energy Harvesting Technologies and Equivalent Electronic Structural Models — Review,” 2019.
- [30] R. M. Ferdous, A. W. Reza, and M. F. Siddiqui, “Renewable energy harvesting for wireless sensors using passive RFID tag technology: A review,” *Renew. Sustain. Energy Rev.*, vol. 58, pp. 1114–1128, 2016, doi: 10.1016/j.rser.2015.12.332.
- [31] C. Rokaya, J. Keskinen, and D. Lupo, “Integration of fully printed and flexible organic electrolyte-based dual cell supercapacitor with energy supply platform for low power electronics,” *J. Energy Storage*, vol. 50, pp. 1–10, 2022, doi: 10.1016/j.est.2022.104221.
- [32] C. Covaci and A. Gontean, “Piezoelectric energy harvesting solutions: A review,” *Sensors (Switzerland)*, vol. 20, no. 12, pp. 1–37, 2020, doi: 10.3390/s20123512.
- [33] H. S. Kim, J. H. Kim, and J. Kim, “A review of piezoelectric energy harvesting based on vibration,” *Int. J. Precis. Eng. Manuf.*, vol. 12, no. 6, pp. 1129–1141, 2011, doi: 10.1007/s12541-011-0151-3.
- [34] S. Jee, L. MH, and Leong Salman, “Review of vibration-based energy harvesting technology: Mechanism and architectural approach,” *Int. J. Energy Res.*, vol. 42, pp. 1866–1893, 2018.
- [35] H. Li, C. Tian, and Z. D. Deng, “Energy harvesting from low frequency applications using piezoelectric materials,” *Appl. Phys. Rev.*, vol. 1, no. 4, 2014, doi: 10.1063/1.4900845.
- [36] D. Benasciutti, L. Moro, S. Zelenika, and E. Brusa, “Vibration energy scavenging via piezoelectric bimorphs of optimized shapes,” *Microsyst. Technol.*, vol. 16, no. 5, pp. 657–668, 2010, doi: 10.1007/s00542-009-1000-5.
- [37] W. P. Q. Tong, B. M. S. Muhammad Ramadan, and T. Logenthiran, “Design



and Simulation of a Piezoelectric Cantilever Beam for Mechanical Vibration Energy Harvesting,” *Int. Conf. Innov. Smart Grid Technol. ISGT Asia 2018*, no. May, pp. 1245–1250, 2018, doi: 10.1109/ISGT-Asia.2018.8467796.

- [38] K. Mohamed, H. Elgamel, and S. A. Kouritem, “An experimental validation of a new shape optimization technique for piezoelectric harvesting cantilever beams,” *Alexandria Eng. J.*, vol. 60, no. 1, pp. 1751–1766, 2021, doi: 10.1016/j.aej.2020.11.024.
- [39] N. S. Shenck and J. A. Paradiso, “Energy scavenging with shoe-mounted piezoelectrics,” *IEEE Micro*, vol. 21, no. 3, pp. 30–42, 2001, doi: 10.1109/40.928763.
- [40] O. Puscasu, N. Counsell, M. R. Herfatmanesh, R. Peace, J. Patsavellas, and R. Day, “Powering Lights with Piezoelectric Energy-Harvesting Floors,” *Energy Technol.*, vol. 6, no. 5, pp. 906–916, 2018, doi: 10.1002/ente.201700629.
- [41] J. Zhao and Z. You, “A Shoe-Embedded Piezoelectric Energy Harvester for Wearable Sensors,” *Sensors*, vol. 14, pp. 12497–12510, 2014, doi: 10.3390/s140712497.
- [42] S. Priya *et al.*, “A Review on Piezoelectric Energy Harvesting: Materials, Methods, and Circuits,” *Energy Harvest. Syst.*, vol. 4, no. 1, pp. 3–39, 2017, doi: 10.1515/ehs-2016-0028.
- [43] R. Calìo *et al.*, “Piezoelectric energy harvesting solutions,” *Sensors (Switzerland)*, vol. 14, no. 3, pp. 4755–4790, 2014, doi: 10.3390/s140304755.
- [44] C. Rokaya, P. Schaeffner, S. Tuukkanen, J. Keskinen, and D. Lupo, “Motion energy harvesting and storage system including printed piezoelectric film and supercapacitor,” 2019, doi: 10.1109/IFETC46817.2019.9073717.
- [45] I. Choudhry, H. R. Khalid, and H. K. Lee, “Flexible piezoelectric transducers for energy harvesting and sensing from human kinematics,” *ACS Appl. Electron. Mater.*, vol. 2, no. 10, pp. 3346–3357, 2020, doi: 10.1021/acsaelm.0c00636.
- [46] M. K. Mishu *et al.*, “Prospective efficient ambient energy harvesting sources for IoT-equipped sensor applications,” *Electron.*, vol. 9, no. 9, pp. 1–22, 2020, doi: 10.3390/electronics9091345.

- [47] S. Banerjee, B. De, P. Sinha, J. Cherusseri, and K. K. Kar, *Handbook of nanocomposite supercapacitor materials*, vol. 300. 2020.
- [48] A. Berrueta, A. Ursua, I. S. Martin, A. Eftekhari, and P. Sanchis, "Supercapacitors: Electrical Characteristics, Modeling, Applications, and Future Trends," *IEEE Access*, vol. 7, pp. 50869–50896, 2019, doi: 10.1109/ACCESS.2019.2908558.
- [49] D. P. Dubal, N. R. Chodankar, D. H. Kim, and P. Gomez-Romero, "Towards flexible solid-state supercapacitors for smart and wearable electronics," *Chem. Soc. Rev.*, vol. 47, no. 6, pp. 2065–2129, 2018, doi: 10.1039/c7cs00505a.
- [50] N. Vukajlović, D. Milićević, B. Dumnić, and B. Popadić, "Comparative analysis of the supercapacitor influence on lithium battery cycle life in electric vehicle energy storage," *J. Energy Storage*, vol. 31, p. 101603, Oct. 2020, doi: 10.1016/J.EST.2020.101603.
- [51] F. Bu, W. Zhou, Y. Xu, Y. Du, C. Guan, and W. Huang, "Recent developments of advanced micro-supercapacitors: design, fabrication and applications," *npj Flex. Electron.*, vol. 4, no. 1, 2020, doi: 10.1038/s41528-020-00093-6.
- [52] S. Werkstetter, "Ultracapacitors usage in wind turbine pitch control systems," San Diego, 2015. [Online]. Available: <https://www.altenergymag.com/article/2015/06/ultracapacitor-usage-in-wind-turbine-pitch-control-systems/20392>.
- [53] H. Camblong, S. Baudoin, I. Vechiu, and A. Etxeberria, "Design of a SOFC/GT/SCs hybrid power system to supply a rural isolated microgrid," *Energy Convers. Manag.*, vol. 117, pp. 12–20, Jun. 2016, doi: 10.1016/J.ENCONMAN.2016.03.006.
- [54] M. Arvani, *Materials and Devices for Energy Autonomous Distributed Electronics*. 2021.
- [55] B. Panda, I. Dwivedi, K. Priya, P. B. Karandikar, and P. S. Mandake, "Analysis of aqueous supercapacitor with various current collectors, binders and adhesives," *2016 - Bienn. Int. Conf. Power Energy Syst. Towar. Sustain. Energy, PESTSE 2016*, no. January, 2016, doi: 10.1109/PESTSE.2016.7516457.
- [56] A. Schneuwly and R. Gallay, "Properties and applications of supercapacitors from state of art to future trends," *Power Convers. Intell. motion*, pp. 1–10, 2000.

- [57] C. Ji, H. Mi, and S. Yang, “Latest advances in supercapacitors: From new electrode materials to novel device designs,” *Chem. Soc. Rev.*, vol. 64, no. 1, pp. 9–34, 2019, doi: 10.1360/N972018-00815.
- [58] S. Il Pyun, C. H. Kim, S. W. Kim, and J. H. Kim, “Effect of Pore Size Distribution of Activated Carbon Electrodes on Electric Double-Layer Capacitor Performance,” *J. New Mater. Electrochem. Syst.*, vol. 5, no. 4, pp. 289–295, 2002.
- [59] H. V. T. Nguyen, J. Kim, and K.-K. Lee, “High-voltage and intrinsically safe supercapacitors based on a trimethyl phosphate electrolyte,” *J. Mater. Chem. A*, pp. 20725–20736, 2021, doi: 10.1039/d1ta05584d.
- [60] “BioProcess International.” <https://bioprocessintl.com/upstream-processing/biochemicals-raw-materials/comparison-of-concentration-measurement-technologies-in-bioprocess-solutions/>.
- [61] E. Frackowiak, Q. Abbas, and F. Béguin, “Carbon/carbon supercapacitors,” *J. Energy Chem.*, vol. 22, no. 2, pp. 226–240, 2013, doi: 10.1016/S2095-4956(13)60028-5.
- [62] S. Lehtimäki, “Printed Supercapacitors for Energy Harvesting Applications,” Tampere University, 2017.
- [63] W. Gu and G. Yushin, “Review of nanostructured carbon materials for electrochemical capacitor applications: Advantages and limitations of activated carbon, carbide-derived carbon, zeolite-templated carbon, carbon aerogels, carbon nanotubes, onion-like carbon, and graphene,” *Wiley Interdiscip. Rev. Energy Environ.*, vol. 3, no. 5, pp. 424–473, 2014, doi: 10.1002/wene.102.
- [64] Y. Ding *et al.*, “A safe and superior propylene carbonate-based electrolyte with high-concentration Li salt,” *Pure Appl. Chem.*, vol. 86, no. 5, pp. 585–591, 2014, doi: 10.1515/pac-2013-1120.
- [65] K. Xie, S. Yu, P. Wang, and P. Chen, “Polyethylene terephthalate-based materials for lithium-ion battery separator applications: A review based on knowledge domain analysis,” *Int. J. Polym. Sci.*, vol. 2021, no. 1, 2021, doi: 10.1155/2021/6694105.
- [66] K. D. Verma, P. Sinha, S. Banerjee, and K. K. Kar, *Handbook of nanocomposite supercapacitors materials*, vol. 300. Springer International Publishing, 2020.

- [67] J. Keskinen *et al.*, “Printed supercapacitors on paperboard substrate,” *Electrochim. Acta*, vol. 85, pp. 302–306, 2012, doi: <https://doi.org/10.1016/j.electacta.2012.08.076>.
- [68] Y. Liu *et al.*, “High-performance flexible all-solid-state supercapacitor from large free-standing graphene-PEDOT/PSS Films,” *Sci. Rep.*, vol. 5, no. 1, p. 17045, 2015, doi: [10.1038/srep17045](https://doi.org/10.1038/srep17045).
- [69] S. Lehtimäki, A. Railanmaa, J. Keskinen, M. Kujala, S. Tuukkanen, and D. Lupo, “Performance, stability and operation voltage optimization of screen-printed aqueous supercapacitors,” *Sci. Rep.*, vol. 7, pp. 1–9, Apr. 2017, doi: [10.1038/srep46001](https://doi.org/10.1038/srep46001).
- [70] H. Li, X. Li, J. Liang, and Y. Chen, “Hydrous RuO<sub>2</sub>-Decorated MXene Coordinating with Silver Nanowire Inks Enabling Fully Printed Micro-Supercapacitors with Extraordinary Volumetric Performance,” *Adv. Energy Mater.*, vol. 9, no. 15, pp. 1–13, 2019, doi: [10.1002/aenm.201803987](https://doi.org/10.1002/aenm.201803987).
- [71] A. Sajedi-Moghaddam, E. Rahmanian, and N. Naseri, “Inkjet-printing technology for supercapacitor application: Current state and perspectives,” *ACS Appl. Mater. Interfaces*, vol. 12, no. 31, pp. 34487–34504, 2020, doi: [10.1021/acsami.0c07689](https://doi.org/10.1021/acsami.0c07689).
- [72] J. S. Sagu, N. York, D. Southee, and K. G. U. Wijayantha, “Printed electrodes for flexible, light-weight solid-state supercapacitors - A feasibility study,” *Circuit World*, vol. 41, no. 2, pp. 80–86, 2015, doi: [10.1108/CW-01-2015-0004](https://doi.org/10.1108/CW-01-2015-0004).
- [73] H. Li *et al.*, “High-performance supercapacitor carbon electrode fabricated by large-scale roll-to-roll micro-gravure printing,” *J. Phys. D: Appl. Phys.*, vol. 52, no. 11, Jan. 2019, doi: [10.1088/1361-6463/AAFBF3](https://doi.org/10.1088/1361-6463/AAFBF3).
- [74] P. Huang *et al.*, “On-chip and freestanding elastic carbon films for micro-supercapacitors,” *Mater. Sci.*, vol. 351, no. 6274, pp. 691–695, 2016, doi: [10.1126/science.aad3345](https://doi.org/10.1126/science.aad3345).
- [75] S. Wang *et al.*, “Scalable Fabrication of Photochemically Reduced Graphene-Based Monolithic Micro-Supercapacitors with Superior Energy and Power Densities,” *ACS Nano*, vol. 11, no. 4, pp. 4283–4291, Apr. 2017, doi: [10.1021/acs.nano.7b01390](https://doi.org/10.1021/acs.nano.7b01390).
- [76] S. Aderyani, P. Flouda, S. A. Shah, M. J. Green, J. L. Lutkenhaus, and H.

- Ardebili, "Simulation of cyclic voltammetry in structural supercapacitors with pseudocapacitance behavior," *Electrochim. Acta*, vol. 390, p. 138822, 2021, doi: 10.1016/j.electacta.2021.138822.
- [77] IEC 62391-1, "International standard : Fixed electric double-layers capacitors for use in electronic equipment-Part 1: Generic Specification," Geneva, 2006.
- [78] Y. Wu and R. Holze, "Self-discharge in supercapacitors: Causes, effects and therapies: An overview," pp. 1–37, 2021, [Online]. Available: <https://doi.org/10.1515/eetech-2020-0100>.
- [79] M. Kaus, J. Kowal, and D. U. Sauer, "Modelling the effects of charge redistribution during self-discharge of supercapacitors," *Electrochim. Acta*, vol. 55, no. 25, pp. 7516–7523, 2010, doi: 10.1016/j.electacta.2010.01.002.
- [80] R. Kötz, M. Hahn, and R. Gallay, "Temperature behavior and impedance fundamentals of supercapacitors," *J. Power Sources*, vol. 154, no. 2, pp. 550–555, 2006, doi: 10.1016/j.jpowsour.2005.10.048.
- [81] X. Sun, X. Zhang, H. Zhang, B. Huang, and Y. Ma, "Application of a novel binder for activated carbon-based electrical double layer capacitors with nonaqueous electrolytes," *J. Solid State Electrochem.*, vol. 17, no. 7, pp. 2035–2042, 2013, doi: 10.1007/s10008-013-2051-1.
- [82] X. Hu, Y. Chen, Z. Hu, Y. Li, and Z. Ling, "All-solid-state supercapacitors based on a carbon-filled porous/dense/porous layered ceramic electrolyte," vol. 165, pp. 1269–1274, 2018, doi: 10.1149/2.0481807jes.
- [83] A. Awitdrus, M. Suleman, N. Syahirah, and S. Shamsudin, "Energy and power of supercapacitor using carbon electrode deposited with nanoparticles nickel oxide," *Int. J. Electrochem. Sci.*, vol. 11, no. 1, pp. 95–110, 2016.
- [84] A. V. Volkov *et al.*, "Understanding the Capacitance of PEDOT:PSS," *Adv. Funct. Mater.*, vol. 27, no. 28, 2017, doi: 10.1002/adfm.201700329.
- [85] C. Rokaya, J. Keskinen, C. Bromels, P. Sch ffner, E. Küzeci, and D. Lupo, "Polymer-based printed electrolytic capacitor and its circuitry application in a low pass filtering, rectifying and energy storage unit," *Flex. Print. Electron.*, vol. 6, no. 2, pp. 1–11, 2021, doi: 10.1088/2058-8585/ac023d.
- [86] M. Zirkl *et al.*, "An all-printed ferroelectric active matrix sensor network based

on only five functional materials forming a touchless control interface,” *Advanced Materials*, vol. 23, no. 18. pp. 2069–2074, 2011, doi: 10.1002/adma.201100054.

- [87] M. Pulkkinen, T. Haapala, J. Salomaa, and K. Halonen, “Low-Power Wireless Transceiver with 67-nW Differential Pulse-Position Modulation Transmitter,” *IEEE Trans. Circuits Syst. I Regul. Pap.*, vol. 67, no. 12, pp. 5468–5481, 2020, doi: 10.1109/TCSI.2020.3013065.
- [88] A. Railanmaa, S. Lehtimäki, J. Keskinen, and D. Lupo, “Non-toxic printed supercapacitors operating in sub-zero conditions,” *Sci. Rep.*, vol. 9, no. 1, p. 14059, 2019, doi: 10.1038/s41598-019-50570-w.
- [89] Y. Freeman *et al.*, “Capacitance stability in polymer tantalum capacitors with PEDOT counter electrodes,” *ECS J. Solid State Sci. Technol.*, vol. 6, no. 7, pp. N104–N110, 2017, doi: 10.1149/2.0031708jss.

# PUBLICATION I

**Integration of fully printed and flexible organic electrolyte-based dual cell supercapacitor with energy supply platform for low power electronics**

C. Rokaya, J. Keskinen and D. Lupo

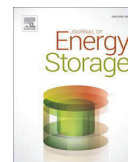
Journal of Energy Storage

<https://doi.org/10.1016/j.est.2022.104221>

**Publication reprinted with the permission of the copyright holders.**







## Research Papers

# Integration of fully printed and flexible organic electrolyte-based dual cell supercapacitor with energy supply platform for low power electronics

Chakra Rokaya<sup>\*</sup>, Jari Keskinen, Donald Lupo

Faculty of Information Technology and Communication Sciences, Tampere University, Korkeakoulunkatu 3, Tampere FI-33720, Finland



## ARTICLE INFO

## Keywords:

Dual cell supercapacitor  
Electrolyte  
Ambient  
Harvester  
Power  
Organic photovoltaic cell  
Energy supply platform  
Energy storage

## ABSTRACT

We report the fabrication of flexible, printed dual cell supercapacitors (DCSCs) and their implementations in energy storage units providing peak power to portable devices. The use of organic electrolytes enhances higher capacity in both potential windows (2.5 V/cell) and the temperature ranges than the aqueous electrolytes, while propylene carbonate retains the advantages of low cost and low toxicity. The device delivered capacitance value between 3 and 4 mF, equivalent series resistance  $< 2 \Omega$ , and very low leakage current of about 0.1  $\mu\text{A}$ . We demonstrated the integration of an organic photovoltaic module (OPV) with an energy supply platform (ESP) and DCSCs for indoor light energy harvesting and storage. The maximum harvested energy was about 39 mJ. The energy is sufficient to provide peak power to portable devices and sensors. This was confirmed by powering an LED with our energy harvesting system. Mechanical deformation testing of DCSCs shows excellent mechanical stability, so that the device is well suited for flexible energy storage units. In a long-term cyclic stability test, the decrease in capacitance value was only 1% of the initial value after 10,000 cycles, indicating good durability and performance.

## 1. Introduction

Research on energy storage devices is a need in today's world to handle environmental and energy issues, which have attracted growing interest in the last decades. Energy storage devices store harvested energy and act as a backup source to provide energy when the primary energy source is not available [1,2]. The main energy storage devices are batteries and supercapacitors. Supercapacitors are a promising and emerging technology [3] for environmentally friendly and low-cost energy harvesting and storage systems in which a traditional battery technology is frequently not the best system, due to toxic or corrosive components, limited peak discharge current, and limited cycle life [4].

Supercapacitors, also known as electric double-layer capacitors (EDLC) [4] or ultracapacitors, have higher power densities than batteries, high efficiency, long cycle life, wide temperature ranges [3,5], quick charging time, high compatibility and no risk of explosion [6]. Supercapacitors are used to provide short term peak power in energy applications such as sensors, active RFID tags, radio transmission, Internet of Things (IoT) [7] and can operate in a wide range of temperature from about  $-40^\circ\text{C}$  to  $100^\circ\text{C}$  [2,8,9]. In general, a supercapacitor assembly consists of current collectors, electrodes, electrolyte,

and separator. Supercapacitors operate at low voltage due to the limited electrochemical window of the electrolyte. With aqueous electrolytes, the maximum potential between electrodes is about 1.3 V, whereas organic electrolytes give a maximum potential of about 3.3 V, thus can provide wider potential window and temperature range than an aqueous electrolyte [2,10].

Energy harvesting from renewable and sustainable sources has become popular in the past decade due to advances in ultralow-power electronics [11]. Flexible energy storage systems are needed for a variety of wearable, low weight, and portable electronics. Ambient energy sources such as heat, light, sound, wind, and vibration can be converted into electrical energy. The practice is called energy harvesting [12]. Previously, we have reported the use of piezoelectric energy harvesters to operate low-power devices [13].

In this paper, we focus on fully printed dual cell supercapacitors (abbreviation: DCSCs) and indoor-light energy harvesting systems which have three main parts: organic photovoltaic (Infinity OPV), energy supply platform (ESP, Epeas) and a supercapacitor (DCSC) as a storage unit. Among different energy sources, light is the most abundant source of the energy and available from indoor light sources such as a fluorescent tube, halogen lamp or LED, as well as outdoors or in indoor

<sup>\*</sup> Corresponding author.

E-mail address: [chakra.rokaya@tuni.fi](mailto:chakra.rokaya@tuni.fi) (C. Rokaya).

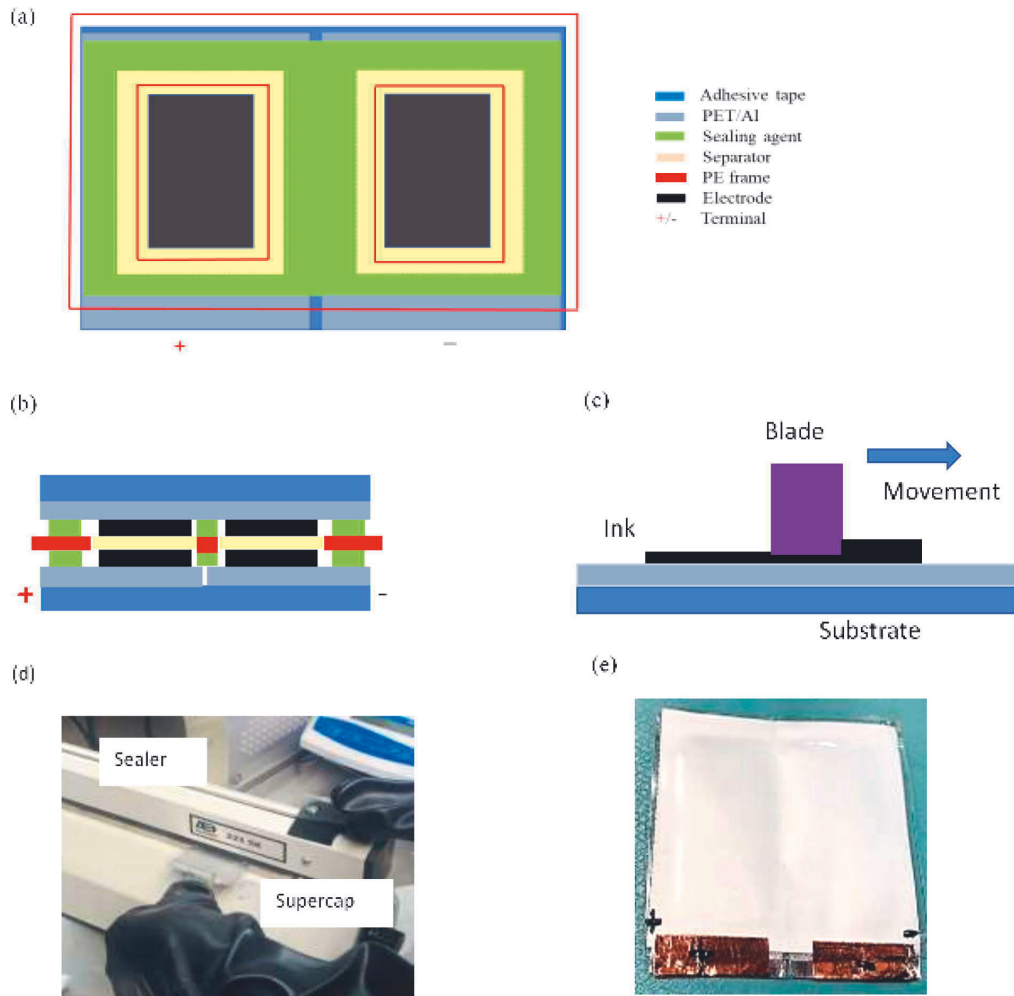


**Fig. 1.** Schematic drawing of dual cell series connected supercapacitor (a, b), Doctor blade coating method (c), Photograph of supercapacitor assembling inside glovebox (d), Fabricated supercapacitor (e). The layer thickness is not to scale.

spaces with windows directly from the sun [14]. Progress in efficient solar cell technology has attracted interest from researchers as well as developers and producers, and quite good low cost solar modules, including flexible modules based on polymers (OPV) are commercially available [15]. Recently, the fabrication of flexible, lightweight, wearable self-powered solar capacitors has been reported. The systems consist of flexible energy harvesting and energy storage module. The system exhibits excellent robustness and mechanical stability for many wearable scenarios. The power conversion efficiency reported was between 10.8 and 14.14% [16,17]. OPV output current is proportional to its active area and can be scaled depending on output energy requirement. Generally, the energy obtainable from ambient indoor light using commercial OPVs is in the range between 10 and 100  $\mu\text{W}/\text{cm}^2$  [18,19]. The modules used in this study, from Infinity PV, have a high degree of flexibility, low weight, thin ( $<0.5$  mm) structure, and are easy to integrate with ESP and supercapacitor. The OPV was characterized with a standard cell testing method, AM1.5 spectrum (1000  $\text{W}/\text{m}^2$ , one sun illumination). The OPV module used in this work is rated to have a power conversion efficiency of 5 %, which would deliver an output

power of 50  $\text{W}/\text{m}^2$  at AM1.5. In far weaker indoor light (approximately 1/100 of AM1.5), the output power is about 0.5  $\text{W}/\text{m}^2$  [20].

Earlier publications describe conventional direct integration of OPV with supercapacitor without a power management IC as a simple stacked device to harvest and store energy. For extremely low-cost systems, this may be adequate, but such an approach has several disadvantages such as low energy conversion, charge imbalance, inefficiency, large power dissipation etc. [21,22]. To mitigate these problems, we used an energy supply platform (ESP): (an E-peas AEM10941 conversion and control full-featured power management circuit board) that acts as an interface between OPV and supercapacitor module. The ESP consists of an ultra-low-power DC-DC buck-boost converter which operates with input voltage in the range from 0.5 V to 5 V and boosts the OPV input voltage to the adjustable output voltage range 2.2–4.5 V. The ESP system provides multiple advantages, such as OPV optimal voltage conditions at maximum power point (MPP) up to 90 %, balance of charge across the dual cell supercapacitor, device protection, increased efficiency of collecting energy, load balance standardization, and regulated power to load by high-efficient low drop output (LDO) regulators [22,23]. The

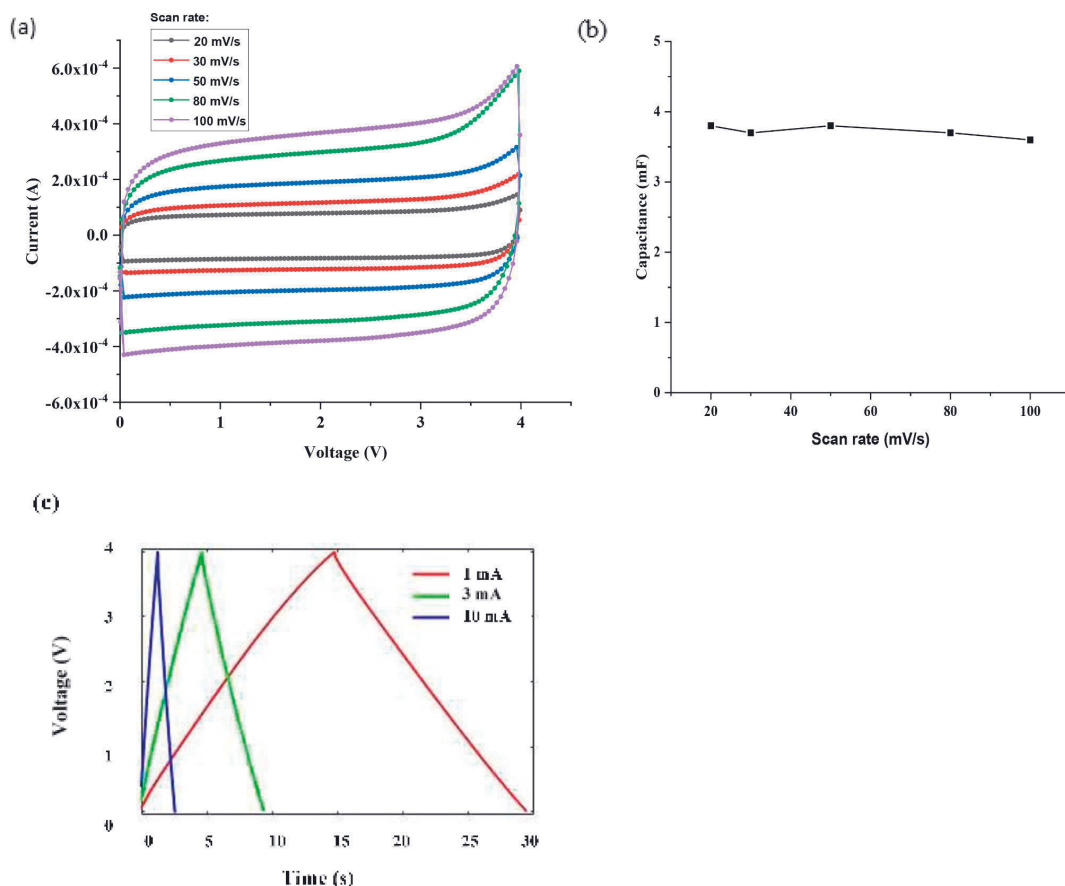


Fig. 2. Cyclic voltammetry measurement (a), Capacitance vs scan rate (b), Charge-discharge measurement (c).

targeted application requires designing of the supercapacitor properties based on the needs of the system. The choices of materials such as electrode ink, electrolyte, and current collector affect the electrical behavior of the supercapacitor in terms of voltage, capacitance, equivalent series resistance (ESR), and device flexibility. In addition to the need for higher voltage per cell and low ESR, scaling and design of the supercapacitor was important. We have previously reported printed supercapacitors for energy storage devices in the range of 100–500 mF [14,24–26]. Activated carbon ink was used to achieve high capacitance because of its high specific surface area, about 1500–2000  $\text{m}^2/\text{g}$ . In this paper, we mainly focus on dual cell (2.5 V/cell) supercapacitors in the range of 3.4 mF to store a small amount of energy that provides sufficient peak power for low energy circuitry or radio transmission. The cells are prepared by depositing pairs of electrodes onto substrates and laminating them into devices which are connected in series internally to provide a maximum potential of 5 V. Super P conductive carbon ink was used to achieve low capacitance because of its relatively low specific surface area of about 62  $\text{m}^2/\text{g}$  and good conductivity that would give improved ESR. Propylene carbonate (PC) electrolyte was used to achieve the targeted voltage range. PC electrolytes have good electrochemical performance, wide temperature range and low toxicity and are thermally stable, safe and relatively inexpensive. Costs are calculated based on the energy consumption and materials costs for the developed device. A cost analysis of the energy storage devices such as supercapacitors, batteries has been reported previously [27]. Like the previously reported

aqueous printed supercapacitors, these are also environmentally friendly, and can be fabricated by low-cost printing processes at low temperature ( $<100^\circ\text{C}$ ), although the final assembly requires a water-free atmosphere. Bending tests on the supercapacitor demonstrate good mechanical stability, while cyclic charge-discharge test demonstrates high cycling stability. Thus, these devices are well suited for flexible energy storage in harvesting and storage systems for distributed electronics.

## 2. Experimental

The schematic structure of the flexible dual cell supercapacitor is shown in Fig. 1(a & b). The fabrication process for this type of printed supercapacitors has been reported earlier [4,24,25,28,29] and is also summarized here. A polyethylene terephthalate and aluminum (PET/Al, Pyroll, thicknesses 50  $\mu\text{m}$  and 9  $\mu\text{m}$ , respectively) substrate size 6 cm by 5 cm was used as a current collector. The electrode material consisted of a mixture of highly conductive Super P carbon (Timcal) and carboxymethyl cellulose (CMC) binder, amounts 90 wt% and 10 wt%, respectively and deionized water to suitable viscosity. The electrodes were printed on the current collector (substrate) with laboratory-scale doctor blade coating method (Mtv Messtechnik) shown in Fig. 1(c). The wet thickness of the ink layer was about 100  $\mu\text{m}$  and the area was 2 cm by 3 cm. The electrodes were cured at  $60^\circ\text{C}$  for 15 min. All prints were weighed before and after applying the carbon ink in order to

**Table 1**  
Measurement of electrical parameters of DCSCs.

S/N	Capacitance (mF)	Capacitance(F/g)	Leakage current (μA)	ESR (Ω)
DCSC1	3.0	0.130	0.10	1.8
DCSC2	3.6	0.125	0.25	2.3
DCSC3	3.9	0.110	0.30	2.4
DCSC4	4.0	0.116	0.24	2.5

determine the specific capacitance from the electrode mass. Once the electrodes were prepared, Paramelt Aquaseal X2277 adhesive was applied on the edges of PET/Al and cured at 80 °C for 20 min.

Once the adhesive was cured, electrodes were immediately transferred to a nitrogen-filled glove box for electrolyte filling and assembly under very clean and dry conditions ( $O_2$  and  $H_2O$  concentration lower than 3 ppm). Then, 1 M tetraethylammonium tetrafluoroborate ( $TEABF_4$ ) in propylene carbonate (PC) electrolyte was prepared inside the glove box. A polyethylene (PE) frame was added between the electrodes to prevent a short circuit. The supercapacitors were then assembled by sandwiching bottom electrodes, separators (Dreamweaver) size 3.5 cm by 2.5 cm and top electrodes as shown in Fig. 1(d). The separator

and electrodes were soaked with electrolyte before assembling to ensure complete filling of the pores. Finally, the system was heat sealed in a face to face configuration with an impulse heat sealer. At the end, 50 μm thick copper tape (3M) was attached to current collectors for robust electrical contact, as shown in Fig. 1(e). The total thickness of the supercapacitor with the packaging was about 0.5 mm, with the length and breadth being 6 cm and 5 cm, respectively.

A Zennium electrochemical workstation (Zahner Elektrik GmbH) was used for cyclic voltammetry (CV) measurements of the supercapacitor. In this method, the supercapacitor was connected to the Zahner workstation. The Zennium CV software allows adjusting the lower and upper potential, number of sweeps, sampling rate etc.

3. Results and discussion

3.1. Cyclic voltammetry (CV) measurement

Cyclic voltammetry is a common method in electrochemical studies and is typically performed using a potentiostat. The value of capacitance was calculated using the formulas given in Eqs. (1) & (2) [30,31]. CV sweeps were measured at different scan rates from 20 mV/s to 100 mV/s at voltage range from 0 to 4 V as shown in Fig. 2(a). The measured

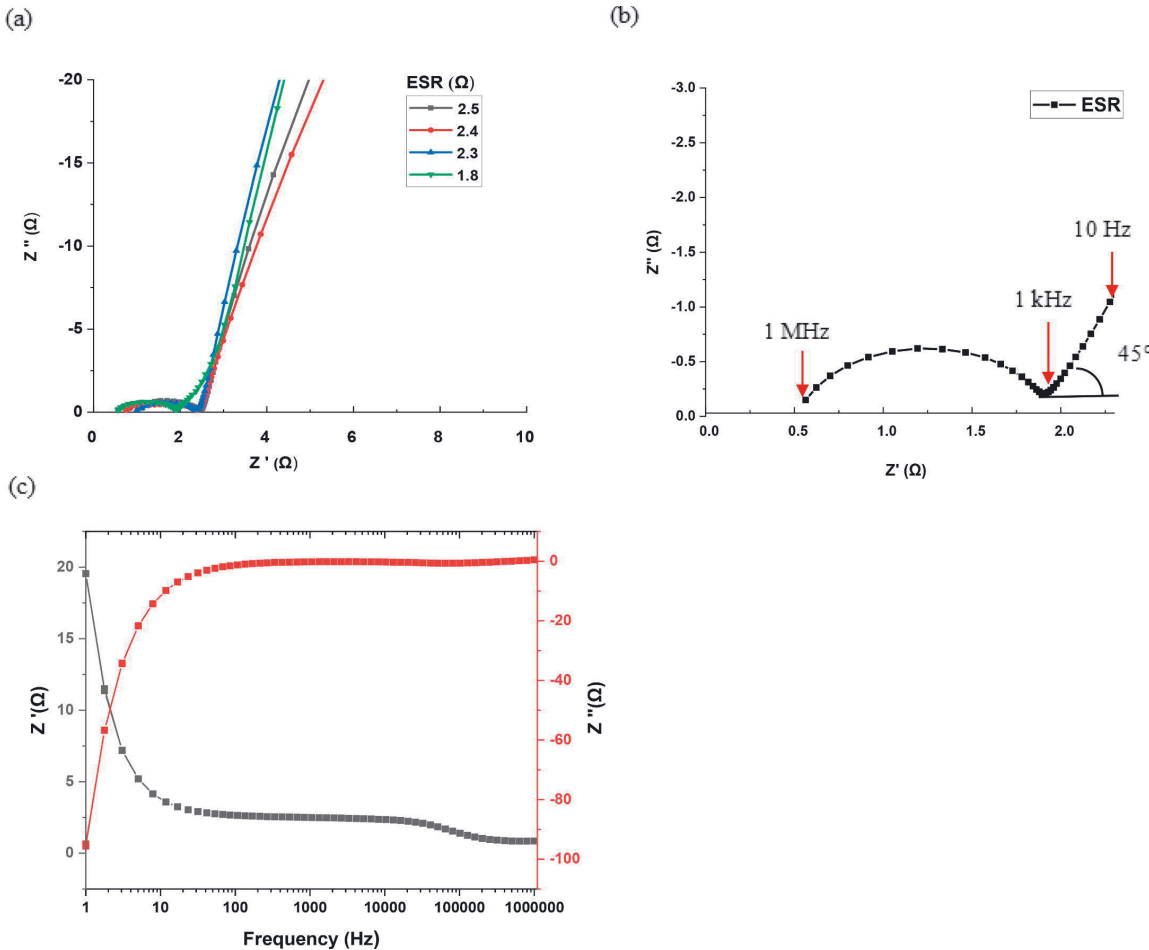


Fig. 3. Nyquist plot real and imaginary impedance (a), Magnified view of Nyquist plot (b), Plot of real and imaginary impedance as a function of frequency (c).

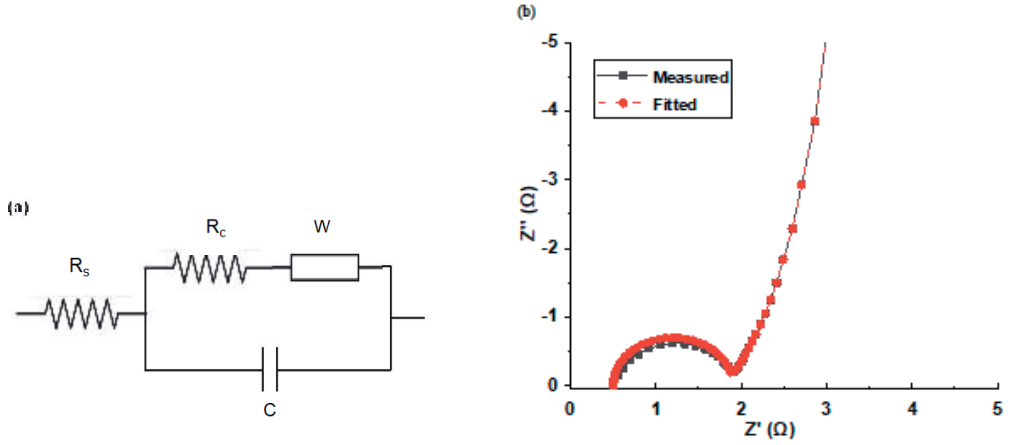


Fig. 4. Randles equivalent circuit model (a), Nyquist plot real and imaginary impedance (Measured and fitted)(b).

capacitance at a different scan rate of device DCSC1 is from 3.6 to 3.9 mF as shown in Fig. 2(b). In total four devices (DCSC1 to DCSC4) were measured for comparison (Table 1).

If  $V(t)$  is an applied voltage to the supercapacitor, the current is defined by Eq. (1).

$$I(t) = C \frac{dV}{dt} \quad (1)$$

The capacitance value is defined by Eq. (2).

$$C = \frac{I(t)}{dV/dt} \quad (2)$$

where  $dV/dt$  is the scan rate.

The capacitance value for these DCSCs is in the range between 3 and 4 mF, as expected due to the low specific area of the electrode ink. CV curves of the capacitors exhibit approximately symmetric rectangular shapes, implying relatively ideal capacitive behaviors of the cells. The galvanostatic charge-discharge curve of the DCSC at a constant current of 1 mA, 3 mA and 10 mA is shown in Fig. 2(c). The applied potential range is from 0 to 4 V. The charging curves of the DCSC are symmetrical with their corresponding discharging curves. This indicates excellent

capacitive characteristics as well as the performance of the DCSC. In addition, almost linear voltage-time curves indicate that the Super P carbon ink has good electrode stability [31,32].

### 3.2. Electrochemical impedance spectroscopy

Electrochemical impedance spectroscopy (EIS) is an electrochemical technique frequently used for the characterization of supercapacitors to obtain information such as capacitance, conductivity, components contributing to the equivalent series resistance, real and imaginary impedances with Nyquist plot and phase angle behavior as a function of frequency with Bode plot method. The importance of EIS has been reported earlier in general, and also for EDLCs [8,29,30,33–39].

In EIS, an AC potential is applied to an electrochemical cell and the amount of current flowing through the cell is measured. The potential excitation is a sinusoidal signal and the response to this is an AC current signal. This AC current signal in the cell contains the excitation frequency and its harmonics. In our EIS measurement, the excitation frequency was in the range from 1 Hz to 1 MHz, with a small excitation signal amplitude of 10 mV. The resulting impedance  $Z$  is a complex number. The Nyquist plot of four DCSCs is shown in Fig. 3(a).

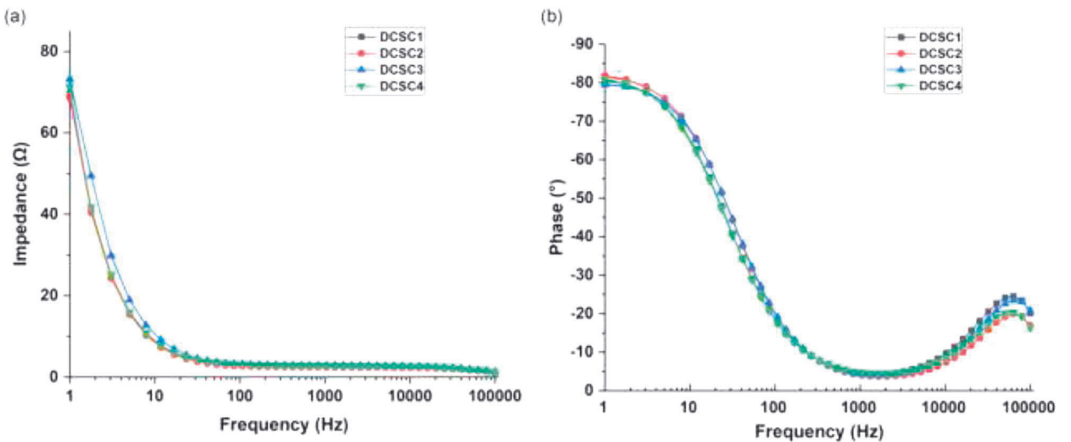


Fig. 5. Bode plot analysis of dual cell supercapacitors. Plot of impedance vs frequency (a), Plot of phase angle vs frequency (b).

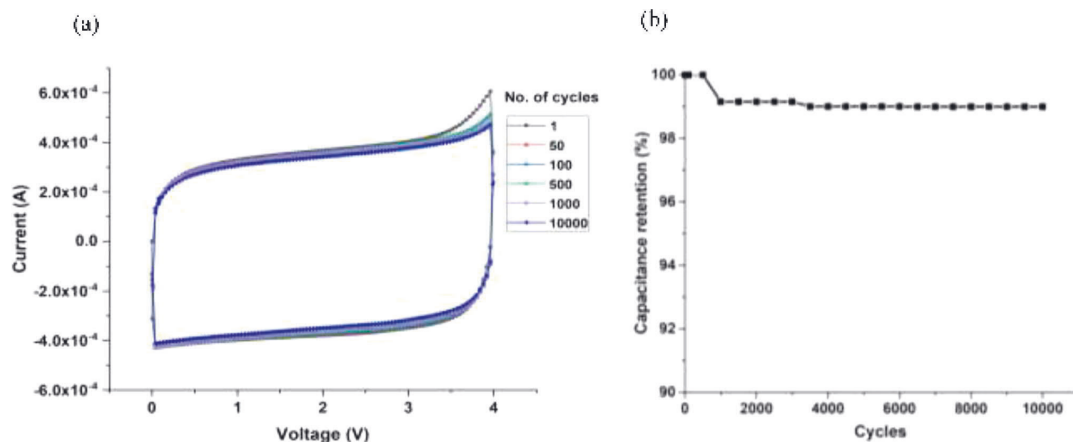


Fig. 6. Cyclic voltammetry graphs from 1 to 10,000 cycles (a), Change in capacitance as a function of cycle number (b).

For an ideal capacitor, the real part of  $Z$  is zero, so the Nyquist plot shows a vertical line only coinciding with the vertical axis. In practice, total impedance consists of real and imaginary values described in Eq. (3) where the impedance's real part is referred to as equivalent series resistance (ESR).

$$Z = \sqrt{Z'^2 + Z''^2} \quad (3)$$

Where,  $Z'$  is the real part and  $Z''$  is the imaginary part of the impedance.

The almost vertical line observed at low frequency is characteristic for ideal capacitance. A slope line of  $45^\circ$  was observed at the intermediate frequency due to the porous structure of active material and is characteristic of the distributed resistance. This region is also called the Warburg diffusion region. The steeper the slope is, the higher is the diffusion capability of ions entering the pores [40]. A semi-circle loop was observed at high frequencies, from 1 kHz to 1 MHz. The shape of the loop is similar in all four DCSCs, and the center of the semicircle lies below the real axis; this is caused by the electron transfer limited process. The ESR decreases towards higher frequencies and intersects the real axis  $Z'$  shown in Fig. 3(a). Fig. 3(b) shows a magnified view of the Nyquist plot. The plot of the real and imaginary value of impedance as a function of frequency is shown in Fig. 3(c). The ESR measured for DCSCs was between 1.8 and 2.5  $\Omega$ . The components defining the ESR of these DCSCs were distributed resistance in the porous active material, contact resistance between the active material and current collector, and the resistance of current collector and electrolyte [8,21,41,42]. The components contributing to the total ESR of the DCSCs can be studied with the Randels circuit model. The Randels circuit model is commonly used in EIS for interpretation of impedance spectra. The circuit model as shown in Fig. 4(a) and Nyquist plot of fitted and measured values for imaginary and real impedance are shown in Fig. 4(b). The circuit model helps in the analysis of bulk resistance (current collector and solution resistance) denoted as  $R_s$  and charge transfer resistance denoted as  $R_c$ , and Warburg diffusion region resistance denoted as  $W$ . In this model, the series element  $R_c$  and  $W$  are connected with capacitor  $C$  in parallel. This parallel combination is connected in series with  $R_s$  shown in Fig. 4 (a) [42].

The value of bulk resistance (current collector and electrolyte)  $R_s$  was from 0.5 to 1  $\Omega$  (left most intersect of real axis), and the charge transfer resistance,  $R_c$  was from 1.2 to 1.4  $\Omega$  (width of semicircle). Finally, the value of distributed resistance in the Warburg diffusion region ( $W$ ) was measured to be from 0.2 to 0.4  $\Omega$  at the  $45^\circ$  line segment.

A Bode plot of the DCSCs related to the impedance and phase behavior over a frequency range from 1 Hz to 100 kHz is given in Fig. 5.

The impedance was high at the low frequency region and decreased with increasing frequency because the impedance of the supercapacitors is inversely proportional to the frequency. At the highest frequency, the ohmic resistance dominates the impedance and the impedance value is constant [34]. The impedance-frequency plot was similar in all four DCSC devices. The phase angle value for devices was from  $79.5^\circ$  to  $81^\circ$ . This value is close to the ideal capacitor value of  $-90^\circ$ . Thus, it indicates the nearly capacitive nature of the device. At a phase angle of  $-45^\circ$ , the resistance and reactance of the devices have equal magnitude. Hence, from the phase-frequency plot diagram, the characteristic frequency at an angle of  $-45^\circ$  is about 22 Hz to 32 Hz. This corresponds to the relaxation time denoted as  $\tau_0$  about 31 to 45 ms ( $\tau_0 = f_0^{-1}$ ). The relaxation time is the minimum time needed to discharge the energy from the capacitor with an efficiency over 50 % of its maximum value [43].

### 3.3. Leakage current

To measure leakage current in our DCSCs, 5 V voltage was applied over them for 24 h and the small float current required to maintain that voltage level was recorded as leakage current. The leakage current was determined using the industrial standard IEC 62391-1 [44]. The measured electrical parameters of DCSCs devices are shown in Table 1. The measured leakage current was very low, between 0.1  $\mu$ A and 0.3  $\mu$ A. One possible cause of the small residual leakage current is from impurities that undergo Faradiac charge-transfer reactions at the electrodes. The impurities may be transition metal ions, which are commonly found in carbon materials [4]. The devices were assembled in inert atmosphere (glove box) to avoid oxygen and water contamination that would be possible in ambient air. Robust sealing of the DCSCs is essential and prevents impurities from entering the devices. This was achieved through hot melt sealing during device assembly.

### 3.4. Life-time test

In order to measure the cyclic stability of the DCSC, we performed cyclic voltammetry from 1 to 10,000 cycles at a scan rate of 100 mV/s. We observed a relatively symmetric rectangular cyclic sweep, as shown in Fig. 6(a), which is indicative of good capacitor behavior. The percentage of change in capacitance as the function of cyclic count is shown in Fig. 6(b); as can be seen, the capacitance value decreases only by 1% from the original value after 10,000 cycles, thus the capacitance of the DCSC reported here is quite stable under cycling.



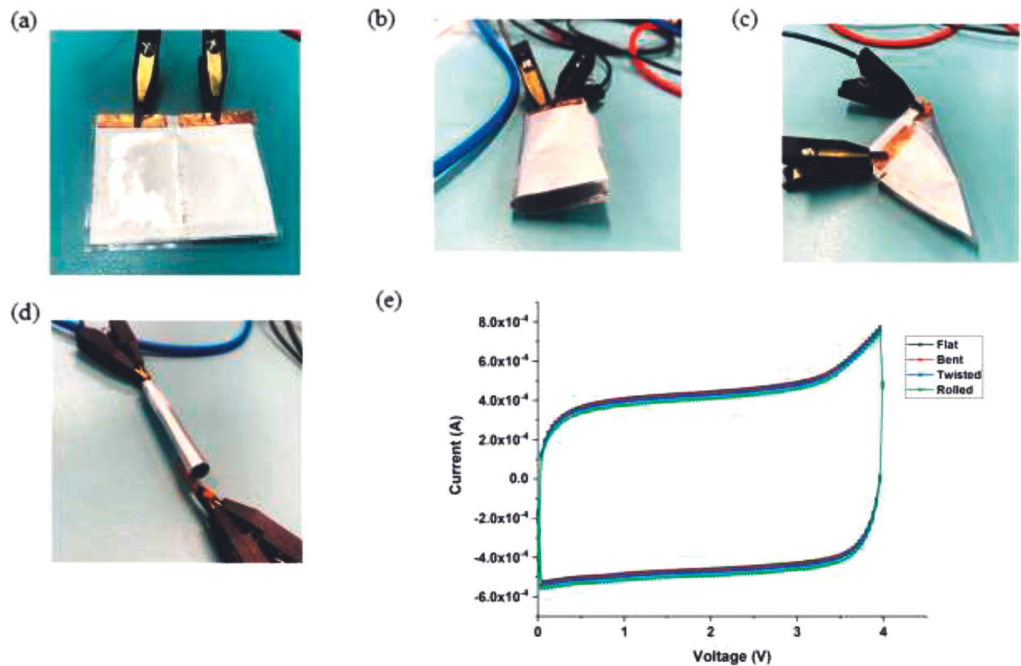


Fig. 7. DCSC under different mechanical deformations: Flat (a), Bent (b), Twisted (c), Rolled (d) and CV measurements graphs of deformed DCSC (e).

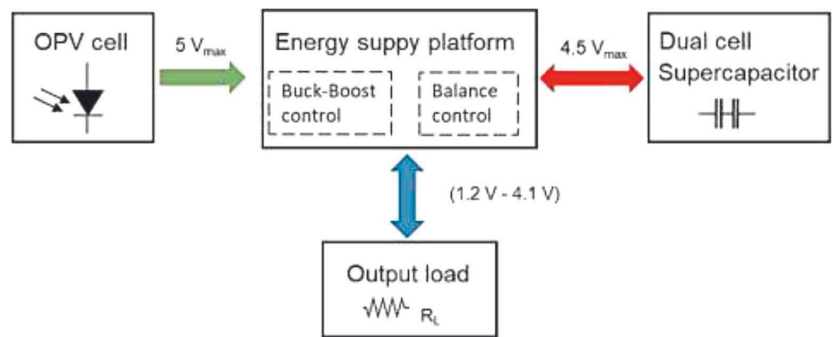


Fig. 8. Schematic view of energy supply platform system with harvester, dual cell supercapacitor and output load unit.

3.5. Mechanical and electrical reliability

Flexibility is a significant property for a printed supercapacitor in many practical applications of electronics. To evaluate the potential and the flexibility of the DCSC for flexible energy storage under real conditions, a mechanical deformation test was performed. The DCSC was bent, twisted and rolled with small curvature radius of 0.5 cm as shown in Fig.7. Cyclic voltammetry was measured at 100 mV/s (0–4 V) to observe the electrical behavior of the DCSC during these mechanical deformations. The cyclic voltammetry curves are almost identical to those measured for unbent devices, indicated excellent mechanical and electrical stability under bending.

3.6. Integration of energy harvester with dual cell supercapacitor

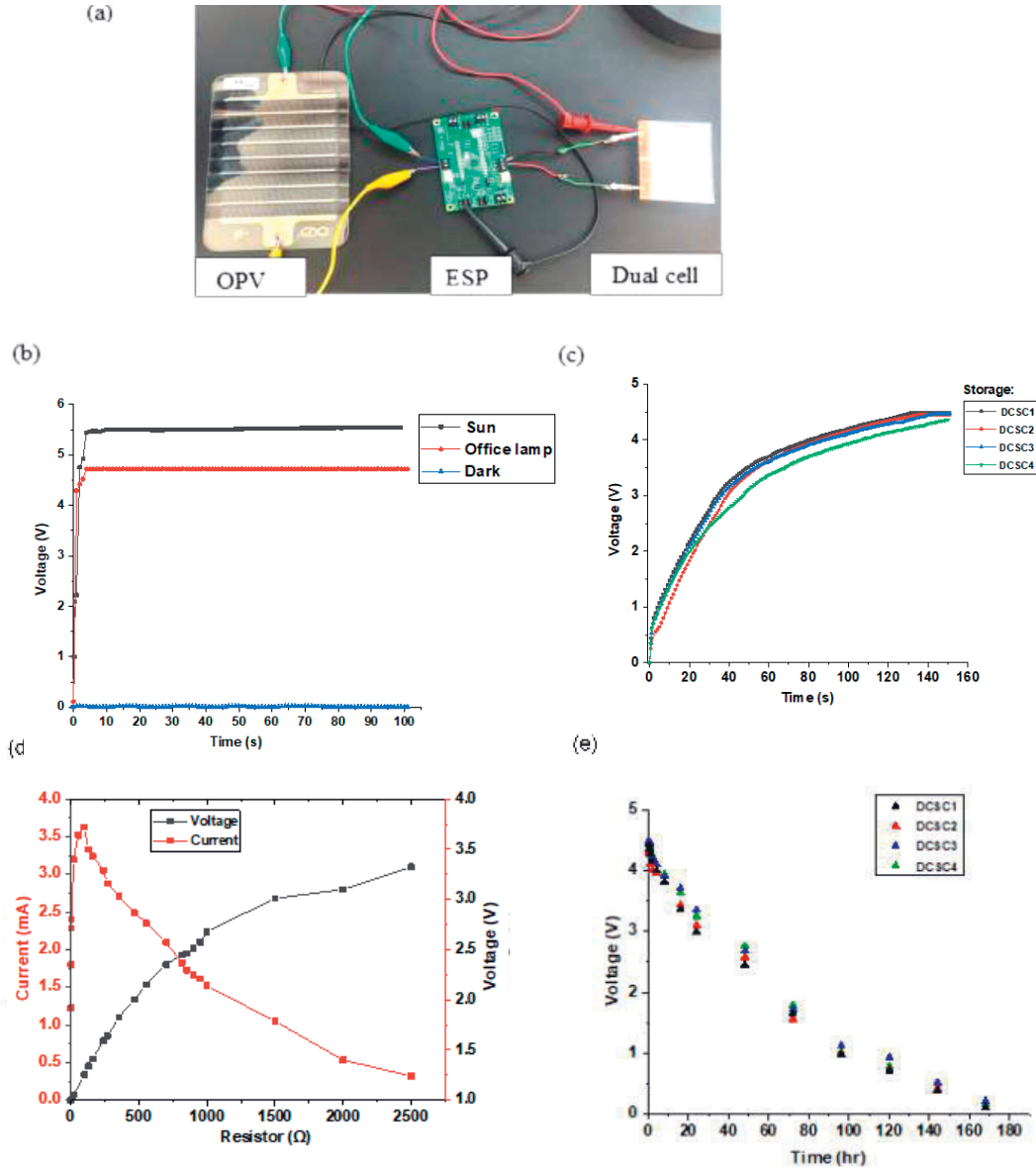
A schematic representation of the energy harvester (OPV module),

Table 2  
MPPT ratio based on the characteristic of the input source.

Config. 1	Config. 2	MPPT
0	0	70%
0	1	75%
1	0	85%
1	1	90%

integrated energy supply platform and dual cell supercapacitor is shown in Fig. 8.

The ESP comprises an AEM10941 harvesting IC, which is suitable for indoor applications because it has ultra-low power startup. The accepted working voltage range of the ESP is between 0.3 V and 5 V. The OPV cell acts as an energy source. The ESP acts as an interface between OPV and the DCSC storage unit. The ESP uses a maximum power point tracking



**Fig. 9.** Photograph of integration of OPV, ESP and dual cell supercapacitor (a), Open circuit voltage measurement of OPV cell under the sun, office lamp and in dark (b), Voltage measured across four dual cell supercapacitors (DCSC) as a function of time (c), Relationship between the output current-voltage and resistor (d), Self-discharge measurement of DCSCs (e).

(MPPT) algorithm to get the most power out of the solar cells. Based on the characteristic of the input power source, the MPPT configuration can be selected as shown in Table 2. The boost converters raise the voltage to a level suitable for charging the DCSC in the range between 2.2 V and 4.5 V. The low drive out (LDO) is available to power loads at different operating voltages between 1.2 V and 4.1 V at a maximum current of 20 mA to 80 mA. When the DCSC voltage reaches the maximum value of 4.5 V, the charge is completed, and internal logic prevents damage to the storage element and to the internal circuitry. If the DCSC is discharged

below 2.2 V, the LDO is power gated to shut down mode and protects the storage element from further discharge [23].

A photograph of the circuit connection of OPV cell, ESP and DCSC is shown in Fig. 9(a). Initially, the open-circuit voltage of the OPV cell was measured at three different conditions: direct sun, office lamp and in dark. The measured output voltage under direct sun and office lamp is about 5.5 V and 4.8 V, respectively, as shown in Fig. 9(b). The plot of output current and voltage of the OPV across the external load resistance in the range 1–2.5 k $\Omega$  is shown in Fig. 9(d). The maximum output



**Table 3**  
Calculation of voltage measured and energy harvested across the four DCSCs.

S/N	Capacitance (mF)	Voltage (V DCSC)	V <sub>DCSC</sub> (%)	Energy harvested (mJ)
DCSC1	3.0	4.49	99.7	30.2
DCSC2	3.6	4.45	98.8	35.6
DCSC3	3.9	4.47	99.3	39.0
DCSC4	4.0	4.35	96.6	37.8

current of 3.72 mA was obtained at a resistance about 100 Ω. Similarly, the maximum power was 5.2 mW at load resistor 1 kΩ. As we are focusing on indoor light energy harvesting, the voltage range is enough to power the ESP unit. The OPV was irradiated with a 7.7 W LED lamp having luminous flux of 806 lm, positioned at a distance of about 30 cm. The voltage across the DCSCs as a function of time is shown in Fig. 9(c). The measured maximum voltage of DCSCs was from 4.35 V to 4.49 V and the logic circuit prevents DCSC from further charging by disabling the boost converter and maintaining charge balance. The energy harvested in the DCSC is given by Eq. (4).

$$E = \frac{1}{2} CV^2 \quad (4)$$

where C is the capacitance and V is the voltage measured across the DCSC

The measured voltage and energy harvested are shown in Table 3. The self-discharge behavior of the supercapacitor was measured over a period of one week. The self-discharge behavior was similar in all supercapacitors. The plot of voltage over time is shown in Fig. 9(c). The maximum charge voltage was 4.5 V, which decreases to below 1 V after 4 days. This is a more rapid decay of voltage than has been seen in larger supercapacitors and is due to the small capacitance (3 to 4 mF). Self-discharge phenomena such as Ohmic leakage (shunt resistance), or diffusion-controlled self-discharge due to the presence of impurities in carbon, make a relatively larger contribution to self-discharge in low-capacitance devices. Ricketts et al. reported quite rapid self-discharge in an organic electrolyte-based supercapacitor and mentioned that the diffusion process causes a significant loss of stored energy [45]. Details about the self-discharge mechanism in supercapacitors have been reported earlier [4,45,46].

Fig. 10(a) shows a photograph of a practical demonstration of an energy harvester unit operating a low power device. In this experiment, a LED was connected to the ESP unit. Once the DCSC reaches a voltage of about 3.6 V, the LDO is turned on and provides peak power to the LED. The LED blinks for a few seconds and the voltage measured across the led was 2.5 V. The voltage of the LED as a function of time is shown in

Fig. 10(b). The peak power generated by the circuit was about 20 mW. This demonstrates that the energy module delivers sufficient energy, even under indoor lighting conditions, to operate low-power portable devices.

#### 4. Conclusion

In this work, we designed an organic electrolyte-based, printable, and flexible dual cell supercapacitor (DCSC), to fulfill the requirements of higher voltage, low ESR and low leakage current. The DCSC is environmentally friendly, manufactured by low-cost printing and coating methods, and fabricated at relatively low temperature (<100 °C). In addition, we have demonstrated an energy harvesting system through the integration of flexible OPV, printed dual cell supercapacitor and energy supply platform. The ESP is capable of tracking maximum power from OPV (MPPT), DC-DC boost of OPV output, charge our supercapacitor efficiently and operate the load device through a low drive output (LDO) unit. The printed 3 to 4 mF DCSC is sufficient to store energy and power a LED. The maximum energy harvested from the harvester was about 39 mJ. This energy is enough for powering portable electronic devices and sensors. DCSCs are mechanically stable, and the devices are well suited for flexible energy storage. In cycle life test up to 10,000 cycles, DCSCs show good performance with about 99 % capacitance retention.

#### Author statement

All authors have participated in (a) conception and design, or analysis and interpretation of the data; (b) drafting the article or revising it critically for important intellectual content; and (c) approval of the final version. Furthermore, each author certifies that this material has not been and will not be submitted to or published in any other publication.

#### Declaration of Competing Interest

All authors have participated in (a) conception and design, or analysis and interpretation of the data; (b) drafting the article or revising it critically for important intellectual content; and (c) approval of the final version. This manuscript has not been submitted to, nor is under review at, another journal or other publishing venue. The authors have no affiliations with or involvement in any organization or entity with any financial interest (such as honoraria; educational grants; participation in speakers' bureaus; membership, employment, consultancies, stock ownership, or other equity interest; and expert testimony or patent/licensing arrangements), or non-financial interest (such as personal or

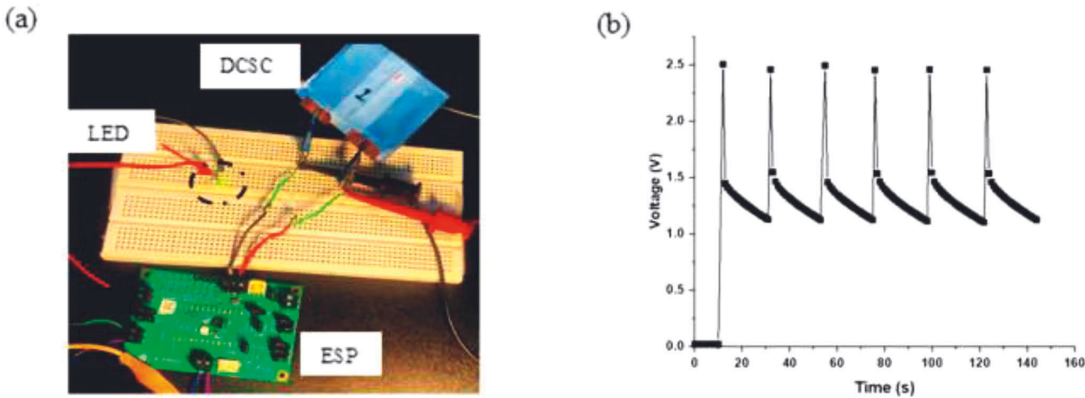


**Fig. 10.** Photograph of energy harvester unit powering a LED (a), Peak voltage measured across LED as a function of time (b).

professional relationships, affiliations, knowledge or beliefs) in the subject matter or materials discussed in this manuscript.

## Acknowledgment

This work was financially supported from the European Union's Horizon 2020 research and innovation programme under grand agreement n 825143, project Smart2Go. We also thank to Mr. Markus Tuomikoski (VTT) and Mr. Andreas Tschopp (Joanneum Research) for helpful discussions related to energy harvesting and integration.

## References

- [1] M. Aneke, M. Wang, Energy storage technologies and real life applications – a state of the art review, *Appl. Energy* 179 (2016) 350–377, <https://doi.org/10.1016/j.apenergy.2016.06.097>.
- [2] K. Hung, C. Masarapu, T. Ko, B. Wei, Wide-temperature range operation supercapacitors from nanostructured activated carbon fabric, *J. Power Sources* 193 (2) (2009) 944–949, <https://doi.org/10.1016/j.jpowsour.2009.01.083>.
- [3] S. Wang, T. Wei, Z. Qi, Supercapacitor energy storage technology and its application in renewable energy power generation system, in: *Proceedings of the ISES World Congress 2007*, 2009, pp. 2805–2809, [https://doi.org/10.1007/978-3-540-75997-3\\_566](https://doi.org/10.1007/978-3-540-75997-3_566). 1– VolV.
- [4] J. Keskinen, et al., Architectural modifications for flexible supercapacitor performance optimization, *Electron. Mater.* 12 (6) (2016) 795–803, <https://doi.org/10.1007/s13391-016-6141-y>.
- [5] K. Krishnamoorthy, P. Pazhamalai, V. K. Mariappan, S. Manoharan, D. Kesavan, and S. Kim, “Two-dimensional Siloxene – raphene heterostructure-based high-performance supercapacitor for capturing regenerative braking energy in electric vehicles,” doi: 10.1002/adfm.202008422.
- [6] H. Moon, et al., Ag/Au/polyppyrole core-shell nanowire network for transparent, stretchable and flexible supercapacitor in wearable energy devices, *Sci. Rep.* 7 (1) (2017) 41981, <https://doi.org/10.1038/srep41981>.
- [7] J. Keskinen, et al., Asymmetric and symmetric supercapacitors based on polypyrrole and activated carbon electrodes, *Synth. Met.* 203 (2015) 192–199, <https://doi.org/10.1016/j.synthmet.2015.02.034>. May.
- [8] R. Köt, M. Hahn, R. Gallay, Temperature behavior and impedance fundamentals of supercapacitors, *J. Power Sources* 154 (2) (2006) 550–555, <https://doi.org/10.1016/j.jpowsour.2005.10.048>.
- [9] X.H. Li, Y.Z. Meng, Q. Zhu, S.C. Tjong, Thermal decomposition characteristics of poly(propylene carbonate) using TG/IR and Py-GC/MS techniques, *Polym. Degrad. Stab.* 81 (1) (2003) 157–165, [https://doi.org/10.1016/S0141-3910\(03\)00085-5](https://doi.org/10.1016/S0141-3910(03)00085-5).
- [10] H.V.T. Nguyen, J. Kim, K.K. Lee, High-voltage and intrinsically safe supercapacitors based on a trimethyl phosphate electrolyte, *J. Mater. Chem. A* (2021) 20725–20736, <https://doi.org/10.1039/d1ta05584d>.
- [11] C. Shi, et al., An ‘all-in-one’ mesh-typed integrated energy unit for both photoelectric conversion and energy storage in uniform electrochemical system, *Nano Energy* 13 (2015) 670–678, <https://doi.org/10.1016/j.nanoen.2015.03.032>.
- [12] A. Nechibvute, A. Chawanda, P. Luhanga, Piezoelectric energy harvesting devices: an alternative energy source for wireless sensors, *Smart Mater. Res.* 2012 (2012) 1–13, <https://doi.org/10.1155/2012/853481>.
- [13] C. Rokaya, P. Schaeffner, S. Tuukkanen, J. Keskinen, and D. Lupo, “Motion energy harvesting and storage system including printed piezoelectric film and supercapacitor,” 2019, doi: 10.1109/IFETC46817.2019.9073717.
- [14] M. Arvani, et al., Flexible energy supply for distributed electronics powered by organic solar cell and printed supercapacitor, in: *Proceedings of the IEEE Conference on Nanotechnology*, 2020, <https://doi.org/10.1109/NANO47656.2020.9183493>, 2020–July.
- [15] T.D. Nielsen, C. Cruickshank, S. Foged, J. Thorsen, F.C. Krebs, Business, market and intellectual property analysis of polymer solar cells, *Sol. Energy Mater. Sol. Cells* 94 (10) (2010) 1553–1571, <https://doi.org/10.1016/j.solmat.2010.04.074>.
- [16] Y. Yang, et al., Self-charging flexible solar capacitors based on integrated perovskite solar cells and quasi-solid-state supercapacitors fabricated at low temperature, *J. Power Sources* 479 (September) (2020), 229046, <https://doi.org/10.1016/j.jpowsour.2020.229046>.
- [17] Z. Tian et al., “Printable magnesium ion quasi-solid-state asymmetric supercapacitors for flexible solar-charging integrated units,” no. 2019, pp. 1–11, doi: 10.1038/s41467-019-12900-4.
- [18] B. Pozo, I. Garate, Á. Araujo, and S. Ferreira, “Energy harvesting technologies and equivalent electronic structural models — review,” 2019.
- [19] R.M. Ferdous, A.W. Reza, M.F. Siddiqui, Renewable energy harvesting for wireless sensors using passive RFID tag technology: a review, *Renew. Sustain. Energy Rev.* 58 (2016) 1114–1128, <https://doi.org/10.1016/j.rser.2015.12.332>.
- [20] InfinityPV, “organic solar cell.” <https://infinitypv.com/11-products/infinitypv/in dex.php>.
- [21] T. Chen et al., “An integrated energy wire for both photoelectric conversion and energy storage,” vol. 51, pp. 11977–11980, 2012, doi: 10.1002/anie.201207023.
- [22] J. O. Thostenson et al., “Integrated flexible conversion circuit between a flexible photovoltaic and supercapacitors for powering wearable sensors integrated flexible conversion circuit between a flexible photovoltaic and supercapacitors for powering wearable sensors,” 2018, doi: 10.1149/2.0141808jes.
- [23] Epeas, “Solar energy harvesting.” <https://e-peas.com/product/aem10941/>.
- [24] J. Keskinen, et al., Printed supercapacitors on paperboard substrate, *Electrochim. Acta* 85 (2012) 302–306, <https://doi.org/10.1016/j.electacta.2012.08.076>.
- [25] S. Lehtimäki, A. Railanmaa, J. Keskinen, M. Kujala, S. Tuukkanen, D. Lupo, Performance, stability and operation voltage optimization of screen-printed aqueous supercapacitors, *Sci. Rep.* 7 (2017), <https://doi.org/10.1038/srep46001>.
- [26] M. Arvani, J. Keskinen, A. Railanmaa, S. Siljander, T. Björkqvist, S. Tuukkanen, Additive manufacturing of monolithic supercapacitors with biopolymer separator, *J. Appl. Electrochem.* (2020), <https://doi.org/10.1007/s10800-020-01423-2>, 0123456789.
- [27] Y. Tian, X. Li, Y. Zhu, R. Xia, Optimal capacity allocation of multiple energy storage considering microgrid cost, *J. Phys. Conf. Ser.* 1074 (1) (2018), <https://doi.org/10.1088/1742-6596/1074/1/012126>.
- [28] A. Railanmaa, et al., Skin-conformable printed supercapacitors and their performance in wear, *Sci. Rep.* 10 (1) (2020) 1–9, <https://doi.org/10.1038/s41598-020-72244-8>.
- [29] X. Sun, X. Zhang, H. Zhang, B. Huang, Y. Ma, Application of a novel binder for activated carbon-based electrical double layer capacitors with nonaqueous electrolytes, *J. Solid State Electrochem.* 17 (7) (2013) 2035–2042, <https://doi.org/10.1007/s10008-013-2051-1>.
- [30] C. Rokaya, J. Keskinen, C. Bromels, P. Schiffer, E. Kılızci, D. Lupo, Polymer-based printed electrolytic capacitor and its circuitry application in a low pass filtering, rectifying and energy storage unit, *Flex. Print. Electron.* 6 (2) (2021) 25005, <https://doi.org/10.1088/2058-8585/ac023d>.
- [31] W. Wang, et al., Hierarchical core-shell Co<sub>3</sub>O<sub>4</sub>/graphene hybrid fibers: potential electrodes for supercapacitors, *J. Mater. Sci.* 53 (8) (2018) 6116–6123, <https://doi.org/10.1007/s10853-017-1971-z>.
- [32] Y. Liu, et al., High-performance flexible all-solid-state supercapacitor from large free-standing graphene-PEDOT/PSS Films, *Sci. Rep.* 5 (1) (2015) 17045, <https://doi.org/10.1038/srep17045>.
- [33] X. Hu, Y. Chen, Z. Hu, Y. Li, and Z. Ling, “All-solid-state supercapacitors based on a carbon-filled porous/dense/porous layered ceramic electrolyte,” vol. 165, pp. 1269–1274, 2018, doi: 10.1149/2.0481807jes.
- [34] K.P. Radha, Magnitude Bode Plot analysis of solid polymer electrolyte PMMA complexed with adipic acid, *Der Pharma Chem.* (2016) 4–9, January.
- [35] N.K. Sidhu, A.C. Rastogi, Bifacial carbon nanofoam-fibrous PEDOT composite supercapacitor in the three-electrode configuration for electrical energy storage, *Synth. Met.* 219 (2016) 1–10, <https://doi.org/10.1016/j.synthmet.2016.04.012>. May 2018.
- [36] B.A. Abdulkadir, J.O. Dennis, M.F.B.A. Shukur, M.M.E. Nasef, F. Usman, Study on dielectric properties of gel polymer electrolyte based on PVA-K2CO<sub>3</sub> composites, *Int. J. Electrochem. Sci.* 16 (1) (2021) 1–15, <https://doi.org/10.20964/2021.01.34>.
- [37] C. H. Chan, “Characterization of polymer electrolytes by dielectric response using electrochemical impedance spectroscopy,” no. February, 2018, doi: 10.1515/pac-2017-0911.
- [38] P. Kurzweil, H.J. Fischle, A new monitoring method for electrochemical aggregates by impedance spectroscopy, *J. Power Sources* 127 (1–2) (2004) 331–340, <https://doi.org/10.1016/j.jpowsour.2003.09.030>.
- [39] G. Porzi, C. Concilio, Halogen-metal interconversion in 2,7-dibromonaphthalene and 2,7-dibromoanthracene, *J. Organomet. Chem.* 128 (1) (1977) 95–98, [https://doi.org/10.1016/S0022-328X\(00\)92039-4](https://doi.org/10.1016/S0022-328X(00)92039-4).
- [40] A. Awitdrus, M. Suleman, N. Syahirah, S. Shamsudin, Energy and power of supercapacitor using carbon electrode deposited with nanoparticles nickel oxide, *Int. J. Electrochem. Sci.* 11 (1) (2016) 95–110.
- [41] S. Lehtimäki, A. Railanmaa, J. Keskinen, M. Kujala, S. Tuukkanen, D. Lupo, Performance, stability and operation voltage optimization of screen-printed aqueous supercapacitors, *Sci. Rep.* 7 (2017) 1–9, <https://doi.org/10.1038/srep46001>. Apr.
- [42] W. Choi, H.C. Shin, J.M. Kim, J.Y. Choi, W.S. Yoon, Modeling and applications of electrochemical impedance spectroscopy (EIS) for lithium-ion batteries, *J. Electrochem. Sci. Technol.* 11 (1) (2020) 1–13, <https://doi.org/10.33961/jecst.2019.00528>.
- [43] W. Hua, et al., Micro-supercapacitors based on oriented coordination polymer thin films for AC line-filtering, *RSC Adv.* 8 (53) (2018) 30624–30628, <https://doi.org/10.1039/c8ra06474a>.
- [44] IEC 62391-1, “International standard : fixed electric double-layers capacitors for use in electronic equipment-Part 1: generic specification,” 2006.
- [45] B.W. Ricketts, C. Ton-Tat, Self-discharge of carbon-based supercapacitors with organic electrolytes, *J. Power Sources* 89 (1) (2000) 64–69, [https://doi.org/10.1016/S0378-7753\(00\)00387-6](https://doi.org/10.1016/S0378-7753(00)00387-6).
- [46] M. Haque, et al., Identification of self-discharge mechanisms of ionic liquid electrolyte based supercapacitor under high-temperature operation, *J. Power Sources* 485 (2020) 2021, <https://doi.org/10.1016/j.jpowsour.2020.229328>. December.

# PUBLICATION II

**Reliability test of fully printed and flexible organic electrolyte-based supercapacitor**

C. Rokaya, J. Keskinen, S. Lahokallio, and D. Lupo

Flexible and Printed Electronics

[10.1088/2058-8585/ac9001](https://doi.org/10.1088/2058-8585/ac9001)

**Publication reprinted with the permission of the copyright holders.**



# Reliability test of fully printed and flexible organic electrolyte-based supercapacitor

Chakra Rokaya<sup>1</sup>, Jari Keskinen<sup>1</sup>, Sanna Lahokallio<sup>2</sup> and Donald Lupo<sup>1</sup>

<sup>1</sup> Faculty of Information Technology and Communication Sciences, Tampere University, Korkeakoulunkatu 3, 33720 Tampere, Finland

<sup>2</sup> Trelic Oy, Tekniikankatu 1, FI-33720 Tampere, Finland

As the demand for supercapacitors in various flexible and wearable energy sectors grows, reliability becomes a key aspect to consider. We report the fabrication and reliability study of printed, flexible organic electrolyte-based supercapacitors. The supercapacitor can be operated over a wide temperature range from -40 °C to 100 °C with excellent repeatability and stability. Thermal shock tests led to a defect in the electrode layer's microstructure, which reduces the supercapacitor performance. Cyclic bending experiments show that the device has excellent robustness, mechanical flexibility, long-term electrical stability, and 100 % capacitance retention up to 10000 bending cycles with a bending radius of 0.41 cm. Thus, the device is suitable for wearable and flexible energy storage applications over a wide temperature range.

Keywords: Supercapacitor, Reliability, Electrolyte, Flexible, Temperature

## 1. Introduction

Supercapacitors, also known as electric double-layer capacitors (EDLC), ultracapacitors, or electrochemical capacitors [1][2]. Supercapacitors have attracted great attention because of their high efficiency, long cycle life, high power densities, wide temperature ranges [3][4], and quick charging time [5]. In many energy applications, supercapacitors are used for providing short term power peaks to devices such as electric vehicles and power tools, as well as for storing energy to power active RFID tags, sensors, sensor networks, and Internet of Things devices (IoT) when the primary energy source is unavailable [6]. Supercapacitors can also be suitable for operation over temperatures from -40 °C to 100 °C [7][8]. In general, a supercapacitor structure is made up of highly porous electrodes, current collectors, separator, and electrolyte. The operation voltage of supercapacitor is limited due to the electrochemical window of the electrolyte.

Compared to the aqueous electrolyte, organic electrolytes can have higher potential window. Some organic electrolytes can provide potential up to 3.3 V, where as with aqueous electrolyte the potential is about 1.3 V [9]. In this reliability study, we used supercapacitors comprising propylene carbonate electrolyte, which can provide up to 2.5 V per cell despite being of low toxicity and cost.

With the recent growth in portable, flexible, wearable, miniaturized electronic products, the demand for flexible and reliable energy storage devices such as supercapacitors has increased. An energy storage device for such applications should be low-cost, environmentally friendly, lightweight, and operate over a wide temperature range [10]. Supercapacitors offer a solution to meet the growing demand for consumer electronics and are widely investigated in terms of reliability [11]. Reliability is a method to check whether the device can perform a required task in specific condition for a given time

interval [12]. Reliability testing, including the determination of failure mechanisms [13], is very important, due to energy storage demand at extreme conditions, and is widely applied to power electronics systems and devices such as inductors, semiconductors, inverters, capacitor banks [14][15] *etc.*, as well as to supercapacitors. Kötzt *et al* [8] investigated temperature dependency behavior of an activated carbon-based supercapacitor in the range -40 °C to 70 °C using 1 M tetraethyl ammonium tetrafluoroborate (TEABF<sub>4</sub>) in acetonitrile and in propylene carbonate (PC). Similar temperature dependent measurement was reported by Liu *et al* [16] and Gualous *et al* [17]. In those cases, the temperature was limited to below 80 °C, even though PC electrolytes can withstand higher temperatures [18]. Azais *et al* [19] investigated electrode pore blockage and gas evolution due to organic electrolyte decomposition on electrode materials. Bitter *et al* [20] observed structural modification of the electrode because of oxidation and reduction. Hahn *et al* [21] found that overvoltage led to a significant expansion of the electrode, and even nominal voltage might result in decomposition of electrode and electrolyte. Oz *et al* [22] investigated the microstructure of the electrode-electrolyte interface changes upon degradation and electrolyte parasitic reactions resulting in precipitation onto the porous surface. This limits the transport of the electrolyte ions to the porous electrode and reduces the performance.

Under extreme conditions, storing energy is still very challenging. A key goal of reliability testing of supercapacitors is to determine their ability to reliably fulfill performance requirements over the targeted range of operating conditions. We have previously reported printed, flexible supercapacitors based on PC electrolyte and carbon black electrodes as energy storage units for low power electronics [23], and report here the result of reliability studies on these devices in different environments, concentrating on performance over a range of temperatures, cyclic bending stability, and reaction to thermal shock. We confirm the functionality of these devices, and possible reasons for the failure following thermal shock tests. In addition, further necessary steps to overcome those failures and design optimization to meet requirements for performance are discussed.

## 2. Experiments

The schematic structure of the supercapacitor is shown in figure 1(a,b). We have reported the fabrication process of similar supercapacitors earlier and briefly summarize the process here [1][23][24][25]. A polyethylene terephthalate and aluminum (5 cm by 4.5 cm) (PET/Al, Pyroll, thicknesses 50 µm and 9 µm, respectively) was used as a current collector. The electrode ink was made with 90 wt% of highly conductive Super P carbon (Timcal) and 10 wt% carboxymethyl cellulose

(CMC) binder. The deionized water added to the mixture to suitable viscosity. The target use case for these devices is as a power peak provider for Bluetooth Low Energy (BLE) transmission in conjunction with a small, printed battery; as a result, the target was a relatively small capacitance of a few mF and a low ESR on the order of 1-2 Ohm. We therefore formulated an electrode ink based on super P carbon black which yields lower capacitance than activated carbon, and also reduces ESR due to high conductivity. These supercapacitors can store sufficient energy and deliver sufficient peak power for a BLE transmission [23]. The laboratory-scale doctor blade unit (Mtv Messtechnik), shown in figure 1(c), was used to print the electrodes on the current collector (substrate). The electrode area of the fabricated supercapacitor was 2 cm by 3 cm and the wet thickness of the was 100 µm. The curing temperature of electrodes were 60 °C for 15 minutes.

Once curing was completed, the electrodes were moved to a nitrogen-filled glove box in order to assemble the device in a clean environment free of water and oxygen. Then, 1 M tetraethylammonium tetrafluoroborate (TEABF<sub>4</sub>) in propylene carbonate (PC) electrolyte was prepared. Although there are other organic electrolytes with wider electrochemical windows (the maximum voltage per cell in the reported devices is 2.5 V), PC was chosen due to low cost and low toxicity. Before assembling the device, the separator and electrode surface was made wet enough with electrolyte, so that the pores get filled. The supercapacitors were then assembled in a sandwiched structure. The electrodes were aligned face to face, separated by the separator (Dreamweaver Titanium 40, dimension 2.5 cm by 3.5 cm). The 3M adhesive tape was used for the adhesion of the electrodes. The overall thickness of the device was about 0.5 mm.

A Zennium electrochemical workstation (Zahner Elektrik GmbH) and software were used for cyclic voltammetry (CV) and electrochemical impedance spectroscopy (EIS) measurements. The supercapacitors were characterized before and after testing. From these, the capacitance and equivalent series resistance (ESR) were determined. Based on the reliability analysis from the cyclic voltammetry at different scan rates and electrochemical impedance spectroscopy, the variation of the capacitance and equivalent series resistance was explained.

Initially, device performance over a wide temperature window ranging from -40 °C to 100 °C was studied. Electrolyte conductivity is one of the most important temperature-dependent properties determining device performance. The operating temperature effect the properties of the electrolytes (e.g. viscosity, thermal stability, solubility, and ionic conductivity). Thus, it leads to changes in capacitance and ESR with temperature. In our experiment, in order to compare

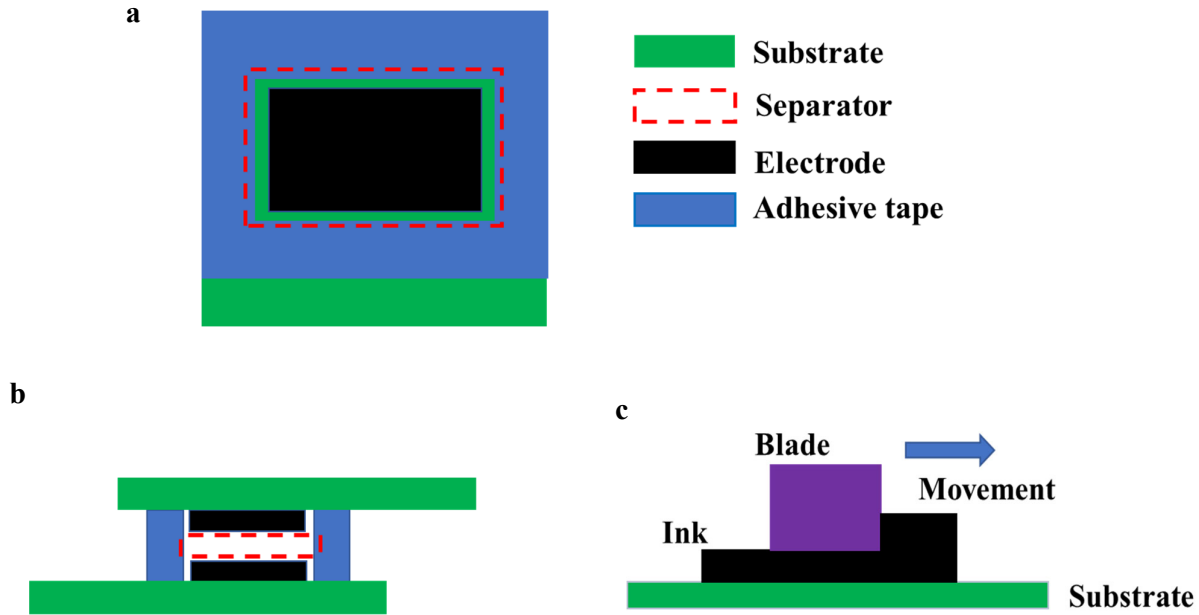


**Figure 1.** Schematic drawing of electrode top view(a), a cross-section of the entire device (b), and doctor blade printing method (c). Layer thickness is not to scale

the influence of the temperature on ESR and capacitance of propylene carbonate electrolyte, the device performance at room temperature (RT) was compared with measurements at low and high temperatures. The supercapacitor was subjected to a climatic test chamber (ESPEC). The results are presented and discussed in Section 3.4.

Next, the robustness of the devices under bending was investigated. While commercial supercapacitors are mostly provided in rigid can-like packages, printed supercapacitors have the potential to be highly flexible, and thus easy to integrate into thin, flexible device applications. We have performed cyclic bending tests on our devices using a Mark 10 bending test system. This testing system is commonly used in electronics for purposes such as bend, peel strength, shear, and component pull-off testing. The cyclic bending setup is shown in figure 5 (a,b,c). One end of the device was attached to the upper grip and the other end was attached to the lower grip. The lower grip was fixed, and the upper grip was adjustable, moving up and down, thus bending the supercapacitors for a specified number of cycles, 8 secs/cycle. Cyclic voltammetry was used to characterize the electrical response of the supercapacitors during these mechanical deformations. The results are presented and discussed in Section 3.5.

In our final experiments, the printed supercapacitors were subjected to thermal shock cycling in a dedicated climate chamber between temperature extremes of  $-40\text{ }^{\circ}\text{C}$  and  $100\text{ }^{\circ}\text{C}$ . The temperature change rate between the extremes of temperatures was  $90^{\circ}/\text{min}$  and dwell time at each temperature extreme 15 minutes, resulting in an approximately 30-minute cycle. Altogether 500 cycles were conducted. The electrical parameters of the supercapacitors were measured before testing as well as after 100, 300, and 500 cycles. The thermal shock cycle of the process is shown in figure 7, where the temperature is set to  $T_0 = -40\text{ }^{\circ}\text{C}$  and  $T_1 = 100\text{ }^{\circ}\text{C}$ ,  $t_1 = t_2 = 15$  minutes. The results are discussed in Section 3.6.

### 3. Results and Discussion

#### 3.1 Cyclic voltammetry measurement

CV is often used in electrochemical studies. Using equations (1,2) [26][27], the capacitance value was calculated. As indicated in figure 2(a), CV sweeps were obtained at various scan rates ranging from  $10\text{ mVs}^{-1}$  to  $80\text{ mVs}^{-1}$  at voltage range from 0 to 2.5 V. Figure 2(b) shows the measured capacitance value from 9 to 10 mF at different scan rates. The capacitance, voltage, and ESR of these devices are sufficient for a two-cell module to apply in BLE transmission.

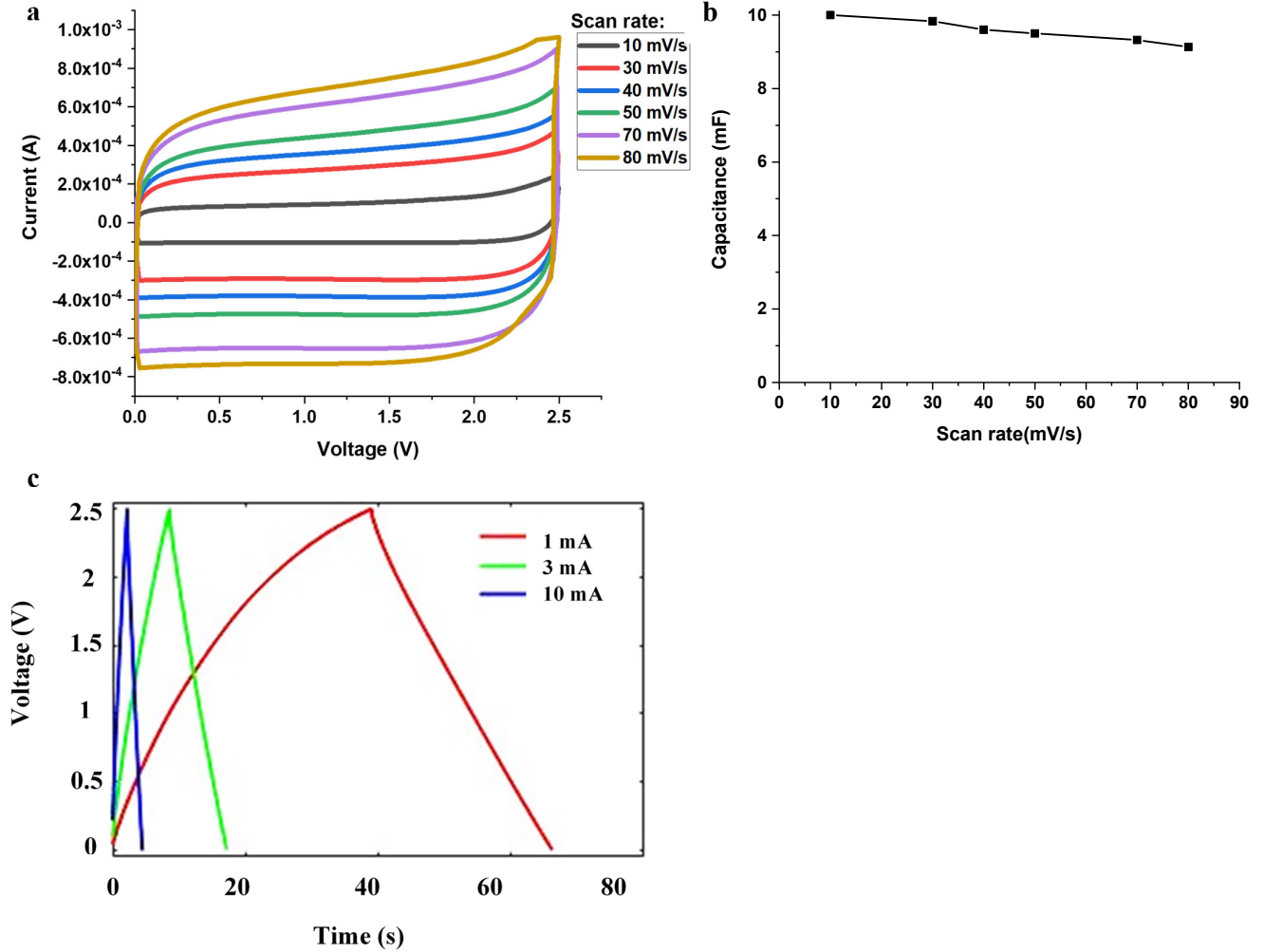


**Figure 2.** A plot of cyclic voltammetry measurement (a), capacitance vs scan rate (b), and charge-discharge measurement (c)

The expression for the current with applied voltage  $V(t)$  to the supercapacitor is given as follow.

$$I(t) = C \frac{dV}{dt} \quad \text{-----} \quad 1$$

The capacitance relation with current and scan rate is given by

$$C = \frac{I(t)}{dV/dt} \quad \text{-----} \quad 2$$

where  $dV/dt$  is the scan rate.

The CV curves show symmetric rectangular shapes that are close to ideal capacitive behaviors of the cells. Figure 2(c) shows device's galvanostatic charge-discharge curves with a constant current of 1 mA, 3 mA, and 10 mA from 0 to 2.5 V. The charging-discharging curves of the device are relatively

symmetrical which indicates good capacitive characteristics. Furthermore, voltage-time curves are linear, implying that the electrodes are stable [27][28].

### 3.2 Electrochemical Impedance spectroscopy

This electrochemical method is often applied to characterize the supercapacitors. This method starts with applying an AC voltage to an electrochemical cell and then measuring current flowing through it. The amplitude of the excitation signal 10 mV with excitation frequency in the range from 1 Hz to 1 MHz. The Nyquist plot of the supercapacitor is shown in figure 3(a). Figure 3(b) shows plot of impedance (real and imaginary) as a function of frequency. As described in Equation (3), the total impedance ( $Z$ ) is a combination of real and imaginary values. The equivalent series resistance is



measured from real part of the Nyquist plot.

$$Z = \sqrt{Z''^2 + Z'^2} \text{ ----- } 3$$

Where,  $Z''$  and  $Z'$  are imaginary and real part respectively.

The porous structure of the active material result a slope line of  $45^\circ$  at the intermediate frequency, which defines the distributed resistance and is also known as Warburg diffusion region. The steeper slope indicates higher diffusion capability of ions entering the pores [29]. At high frequencies ranging from 1 kHz to 1 MHz, a semi-circle loop was observed. As shown in figure 3(a,b), the ESR intersects the real axis  $Z'$  and decreases towards higher frequencies. The ESR value of device was from 1.1  $\Omega$  to 2  $\Omega$ . The ESR consists of the electrolyte resistance (denoted as  $R_1$ , left most intersect  $Z'$ ), electrode and current collector's contact resistance (denoted as  $R_2$ , width of the semicircle), and porous active material's distributed resistance (denoted as  $R_3$ ,  $45^\circ$  segment) [8][25].

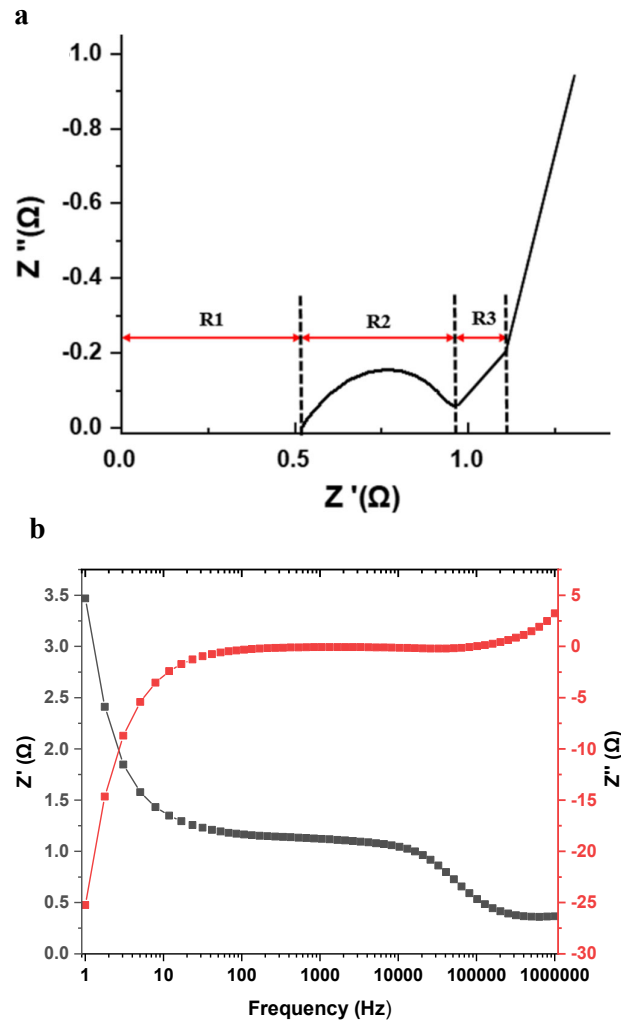


Figure 3: Nyquist plot (a), and plot of real and imaginary impedance as function of frequency (b)

### 3.3 Leakage current

The leakage current in our supercapacitors was measured by applying 2.5 V for 24 hours. In order to maintain that voltage level, a small float current needed which is called a leakage current. By using the industrial standard IEC 62391-1 [30], leakage current was recorded. Very low leakage current between 0.1  $\mu\text{A}$  and 0.4  $\mu\text{A}$  was measured. The impurities at the electrodes due to Faradiac charge-transfer reactions may cause small residual leakage current. The impurities which are frequently found in carbon materials may be transition metal ions. Final assembly of these devices in glove box and robust sealing is very important to prevent water or oxygen from entering the devices.

### 3.4 Temperature test

The CV curves at scan rate 5 mV/s (0 - 2.5 V) and the EIS measurement graph, from which capacitance and ESR were determined between  $-40^\circ\text{C}$  and  $100^\circ\text{C}$ , are shown in figure 4(a,c). The CV curves are relatively rectangular, indicating good capacitor performance and electrode stability. However, the area of the curve changes due to the effect of temperature on the electrochemical performance of the supercapacitor. The reference RT capacitance and ESR values were 8.5 mF and 1.97  $\Omega$ , respectively. The plot of ESR as function of temperature is shown in figure 4b. Table 1 shows the supercapacitor capacitance and ESR performance under different temperature conditions. The dependence of capacitance on temperature is substantially weaker than the dependence of ESR. The capacitance increased by 11% at  $100^\circ\text{C}$  and decreased by 7% at  $-40^\circ\text{C}$ . On the other hand, there is a significant change in ESR with a decrease in temperature. The ESR value increases from 1.97  $\Omega$  to 4.98  $\Omega$  from RT to  $-40^\circ\text{C}$ . The increase in ESR at low temperature is due to the increased viscosity and reduced ionic conductivity of the electrolyte. As can be seen from figure 4(c) with the help of the Nyquist plot, the major component contributing to ESR is the electrolyte resistance (leftmost intersect of the real axis  $Z'$ ), which gradually increases with decreasing temperature.

At RT the electrolyte resistance was 0.55  $\Omega$ , which increased to 2.32  $\Omega$  at  $-40^\circ\text{C}$ . This results from the increased viscosity, which inhibits free movement of ions in the electrolyte and through the porous separator and pores in the carbon electrode. The second dominant factor was the distributed resistance due to ion diffusion in the porous active material which was 0.1  $\Omega$  and 0.9  $\Omega$  at RT and  $-40^\circ\text{C}$ , respectively. The difference in ESR is very small at high temperature. In addition, the

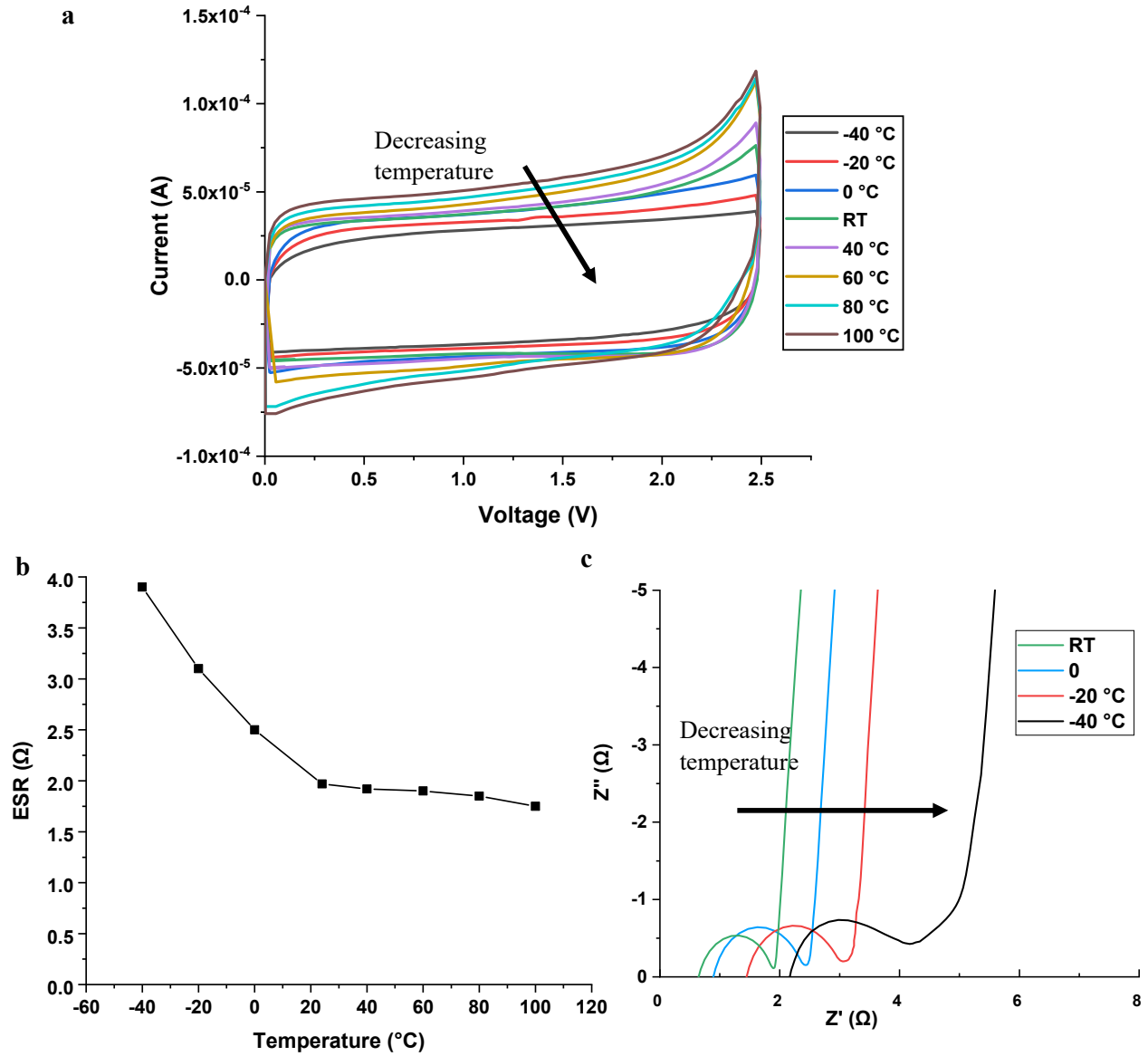


**Figure 4.** Cyclic voltammetry measurement at a different temperature from -40 °C to 100 °C at 5mV/s (a), Plot of equivalent series resistance vs temperature (b), and Nyquist plot of real and imaginary impedance (c)

supercapacitor retained its room temperature capacitance when cooled from 100 °C and defrosted from -40 °C, indicating stability and repeatability of the device.

The results reported here for flexible supercapacitors are consistent with earlier work on organic electrolytes-based supercapacitors in other architectures. Liu *et al* [16] investigated a rise in ESR for PC-based supercapacitors from 16 m $\Omega$  to 77 m $\Omega$  for RT and -30 °C. Kötzt *et al* [8] reported an increased in ESR by 200% from 2.5 m $\Omega$  to 7.5 m $\Omega$ , mainly

dominated by the distributed resistance at the 45° region. Zhi *et al* [31] reported significant changes in ESR from 135 m $\Omega$  to 876 m $\Omega$  at 60 °C and -40 °C respectively.

Table 1. Capacitance and ESR change with temperature

Temperature (°C)	Capacitance (mF)	Change capacitance %	ESR	Change ESR %
100	9.5	11	1.78	-9.6
80	9.4	10.5	1.85	-6.0
60	9.3	9.4	1.9	-3.5
40	8.7	2.3	1.93	-2.0
RT	8.5	0	1.97	0
0	8.4	-1.1	2.5	26.9
-20	8	-5.8	3.13	58.8
-40	7.9	-7	4.98	153

### 3.5 Cyclic bending test

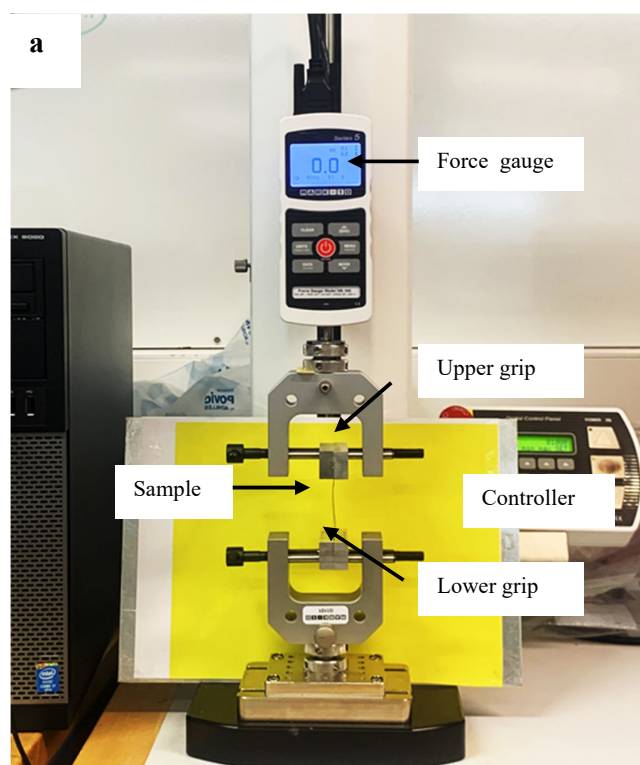
The cyclic voltammetry curves are almost identical, indicating excellent and long-term mechanical, electrical stability, and reliability under deformations. Figure 5 shows the measurement Mark 10 setup. Similarly, figure 6(a) shows the CV measurement at up to 10000 bending cycles. The plot of capacitance retention is shown in figure 6(b). We observed 100 % capacitance retention and the ESR was constant at about  $1.1 \Omega$  after 10000 bending cycles. The devices are well functional and the electrochemical performance is well maintained under various deformations. There was no sign of physical damage, delamination, or leakage in the device due to robust sealing. The minimum bending radius tested was 0.41 cm, which indicates sufficient flexibility for a wide range of printed and wearable electronics applications.

### 3.6 Thermal shock test

Gualous et al [17] investigated the reaction of conventional supercapacitors to thermal shock and found a decrease in the electrical performance. However, in their study, the temperature was limited to between  $-20^\circ\text{C}$  to  $80^\circ\text{C}$  and 20 cycles only, even though PC electrolyte has the potential to withstand temperatures much higher than  $80^\circ\text{C}$  [18].

The area of the CV curves becomes smaller in size as shown in figure 8(a), indicating reduced capacitance, and ESR increases as the number of test cycles increases. The supercapacitor behaves relatively well up to 100 cycles, followed by more severe degradation with increasing number of thermal shock cycles. The capacitance decreased to less than half of the initial value, from 9.5 to 3.5 mF, after 500 cycles. From the Nyquist plot of real and imaginary impedance, we observed that there is a significant increase in the contact resistance between the current collector and electrode at 500 cycles (width of semicircle), as shown in figure 8(b). Even though the electrolyte and diffusion

resistance increase, the contact resistance is dominant, at about  $40 \Omega$ . To investigate a possible cause, the electrodes were analyzed under a microscope Olympus BX51. As shown in figure 9, the microscopic images show microstructural defects, cracks, and peel-off of the electrode after being subjected to thermal shock cycling. The degradation in the microstructure of the electrode layer results in weak contact with the current collector. This is believed to be due to the difference in coefficients of thermal expansion for the materials in the polymer/aluminum/carbon stack and is the most likely cause for the decrease in the electrical performance of the supercapacitors.



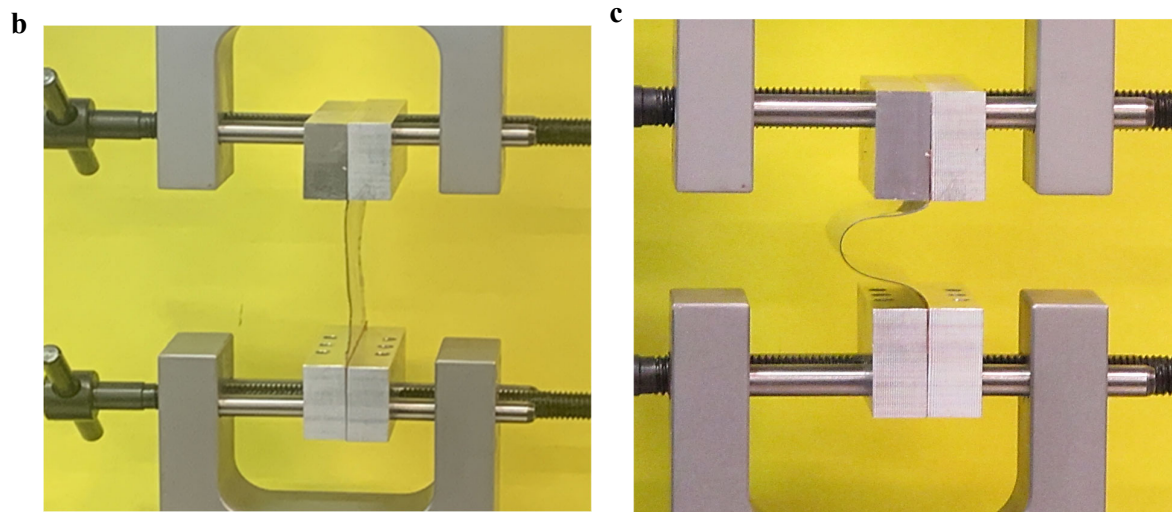
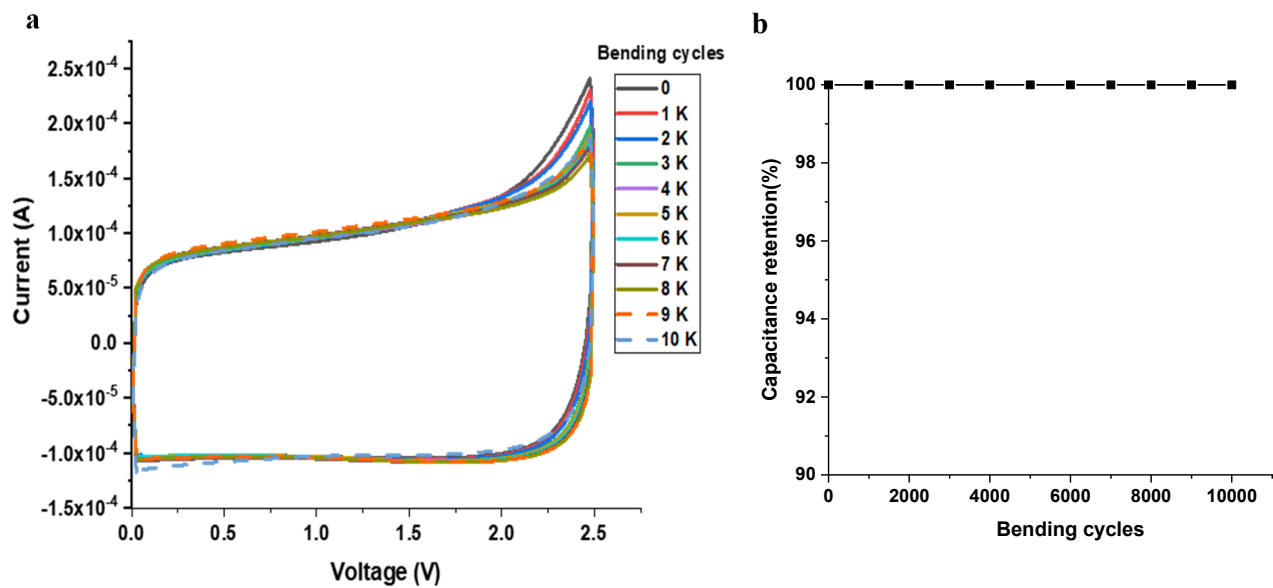


Figure 5. Photograph of mark 10 test setup system (a), before bend(b), after bend (c)



**Figure 6.** CV measurement up to 10000 bending cycles at scan rate  $10\text{mVs}^{-1}$  (a), a plot of capacitance retention vs bending cycles (b)

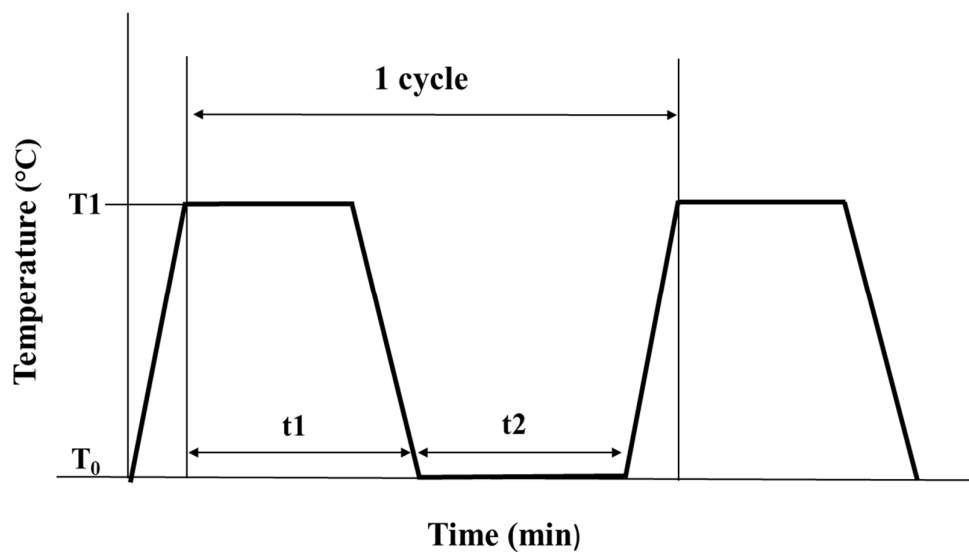


Figure 7. Thermal shock test process

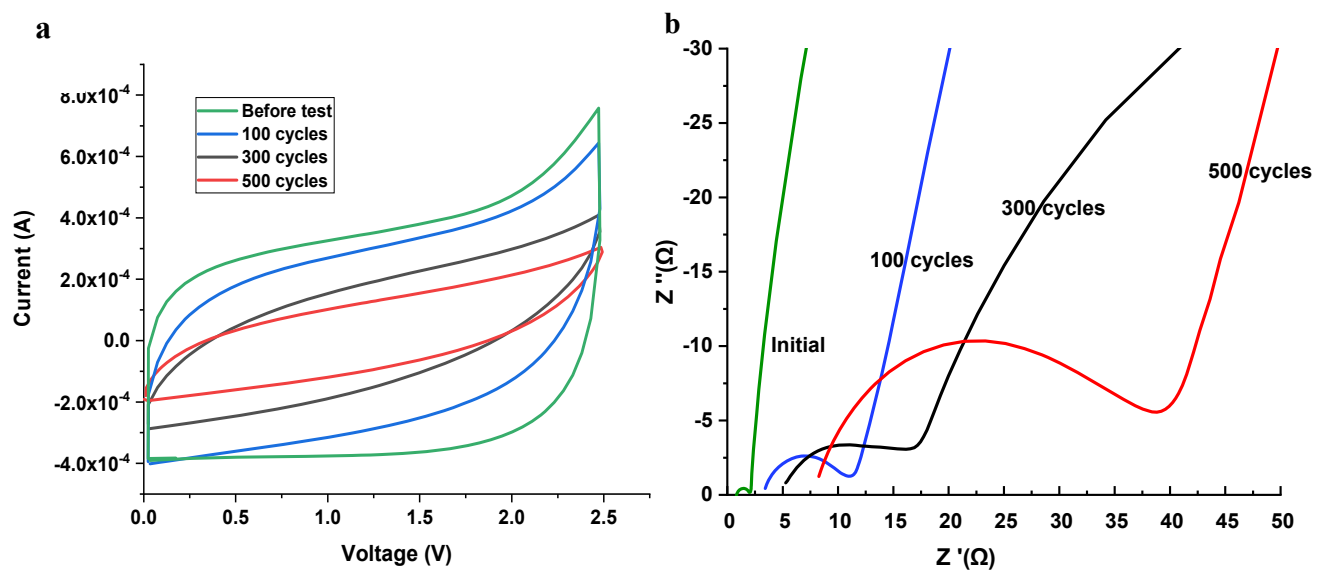
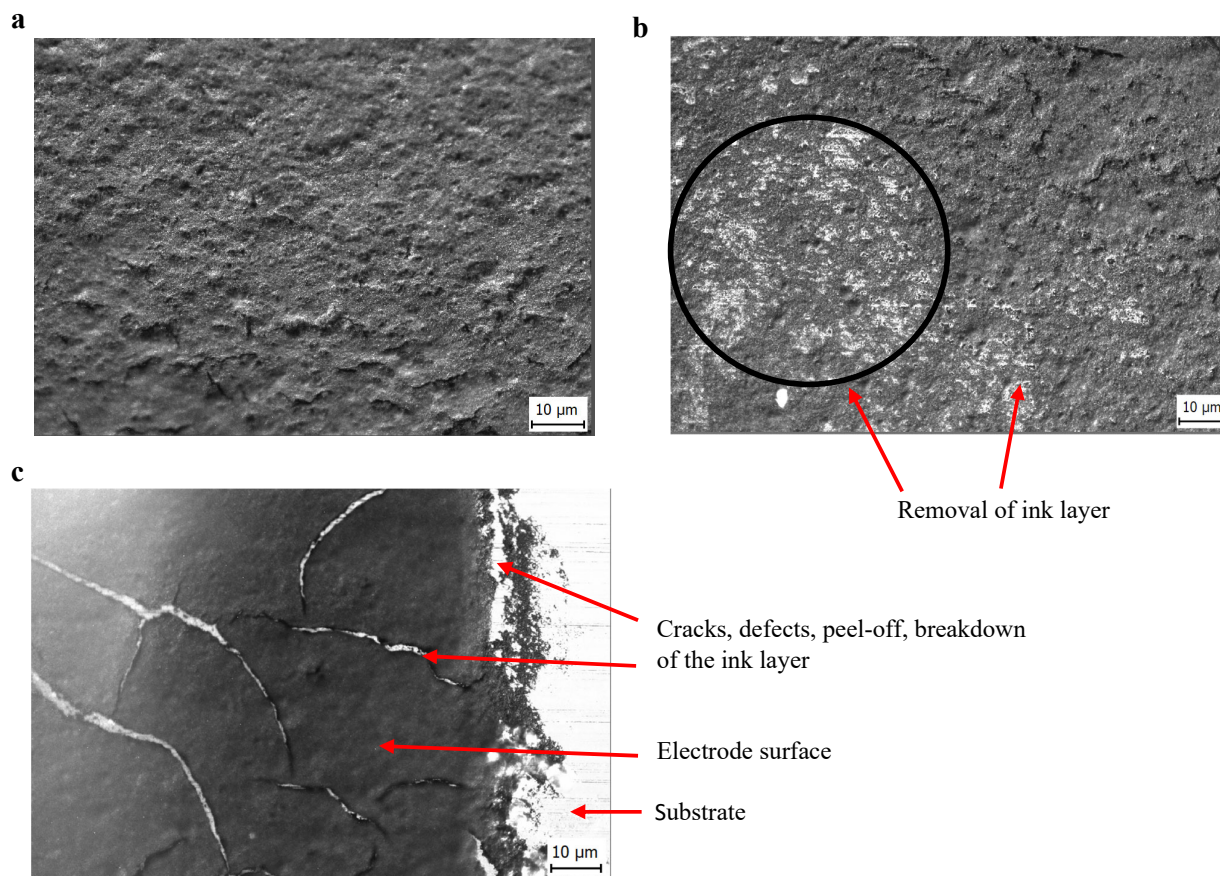


Figure 8. Cyclic voltammetry measurement before and after thermal shock test (a), and Nyquist plot (b) up to 500 cycles





**Figure 9:** Microscopic images of printed electrode surfaces, before thermal shock test (a), and after thermal shock test (b) removal of the electrode layer (white spot area) and (c) cracks, defects, and peel off of the electrode layer

#### 4. Conclusion

In this work, we report a systematic reliability study of an organic electrolyte-based, printable, and flexible supercapacitor. The devices, which contained 1 M TEABF<sub>4</sub>/PC as electrolyte, were shown to operate successfully over the quite wide temperature range of -40 °C to 100 °C. The capacitance depends only weakly on temperature, while the ESR varies considerably. At sub-zero temperature, the ESR is the main limiting factor in terms of the electrical performance of the supercapacitor. Despite the stability to gradually changing temperature, thermal shock tests cause a significant decrease in device performance. This is due to an increase in contact as a result of formation of

microcracks and defects in the porous electrode layer, which causes poor electrical contact to the current collector. The supercapacitors show excellent electrical performance under cyclic bending tests, confirming mechanical flexibility, stability, and robustness under up to 10000 bending cycles, with a minimum bending radius of 0.41 cm. Thus, these printed, simple structures, and lightweight supercapacitors are well suited and very promising for wearable and flexible electronics for energy storage applications.

## Acknowledgements

This work was financially supported by the European Union's Horizon 2020 research and innovation programme under grant agreement no 825143, project Smart2Go. The infrastructure of Laboratory for Future Electronics at Tampere University is supported by Academy of Finland Finnish Research Infrastructure (FIRI, Grant No. 320019).

## References

- [1] Keskinen J, Lehtimäki S, Dastpak A, Tuukkanen S, Flyktman T, Kraft T, Railanmaa A and Lupo D 2016 Architectural modifications for flexible supercapacitor performance optimization *Electron. Mater. Lett.* 12 795–803
- [2] Zhang R, Xu Y, Harrison D, Fyson J and Southee D 2016 A study of the electrochemical performance of strip supercapacitors under bending conditions *Int. J. Electrochem. Sci.* 11 7922–33
- [3] Wang S, Wei T and Qi Z 2009 Supercapacitor energy storage technology and its application in renewable energy power generation system *Proceedings of ISES World Congress 2007 (Vol. I -- Vol. V)* ed D Y Goswami and Y Zhao (Berlin, Heidelberg: Springer Berlin Heidelberg) pp 2805–9
- [4] Krishnamoorthy K, Pazhamalai P, Mariappan V K, Manoharan S, Kesavan D and Kim S Two-dimensional Siloxene – graphene heterostructure-based high-performance supercapacitor for capturing regenerative braking energy in electric vehicles
- [5] Moon H, Lee H, Kwon J, Suh Y D, Kim D K, Ha I, Yeo J, Hong S and Ko S H 2017 Ag/Au/Polypyrrole core-shell nanowire network for transparent, stretchable and flexible supercapacitor in wearable energy devices *Sci. Rep.* 7 41981
- [6] Keskinen J, Tuurala S, Sjödin M, Kiri K, Nyholm L, Flyktman T, Strømme M and Smolander M 2015 Asymmetric and symmetric supercapacitors based on polypyrrole and activated carbon electrodes *Synth. Met.* 203 192–9
- [7] Hung K, Masarapu C, Ko T and Wei B 2009 Wide-temperature range operation supercapacitors from nanostructured activated carbon fabric *J. Power Sources* 193 944–9
- [8] Kötz R, Hahn M and Gallay R 2006 Temperature behavior and impedance fundamentals of supercapacitors *J. Power Sources* 154 550–5
- [9] Nguyen H V T, Kim J and Lee K-K 2021 High-voltage and intrinsically safe supercapacitors based on a trimethyl phosphate electrolyte *J. Mater. Chem. A* 20725–36
- [10] Nyholm L, Nyström G, Mihranyan A and Strømme M 2011 Toward Flexible Polymer and Paper-Based Energy Storage Devices 23 3751–69
- [11] Shi S, Xu C, Yang C, Li J, Du H, Li B and Kang F 2013 Review Flexible supercapacitors Particoulougy 11 371–7
- [12] Liu S, Wei L and Wang H 2020 Review on reliability of supercapacitors in energy storage applications *Appl. Energy* 278 115436
- [13] Kim S K, Kim H J, Lee J C, Braun P V. and Park H S 2015 Extremely Durable, Flexible Supercapacitors with Greatly Improved Performance at High Temperatures *ACS Nano* 9 8569–77
- [14] Wang H, Liserre M, Blaabjerg F, de Place Rimmen P, Jacobsen J B, Kvisgaard T and Landkildehus J 2014 Transitioning to Physics-of-Failure as a Reliability Driver in Power Electronics *IEEE J. Emerg. Sel. Top. Power Electron.* 2 97–114
- [15] Zhou D, Song Y, Liu Y and Blaabjerg F 2019 Mission Profile Based Reliability Evaluation of Capacitor Banks in Wind Power Converters *IEEE Trans. Power Electron.* 34 4665–77
- [16] Liu P, Verbrugge M and Soukiazian S 2006 Influence of temperature and electrolyte on the performance of activated-carbon supercapacitors *J. Power Sources* 156 712–8
- [17] Gualous H, Gallay R, Alcicek G, Tala-ighil B, Oukaour A, Boudart B and Makany P 2010 Supercapacitor ageing at constant temperature and constant voltage and thermal shock *Microelectron. Reliab.* 50 1783–8
- [18] Jasinski R and Carroll S 1970 Thermal Stability of a Propylene Carbonate Electrolyte *J. Electrochem. Soc.* 117 218
- [19] Azaïs P, Duclaux L, Florian P, Massiot D, Lillo-Rodenas M A, Linares-Solano A, Peres J P, Jehoulet C and Béguin F 2007 Causes of supercapacitors ageing in organic electrolyte *J. Power Sources* 171 1046–53
- [20] Bittner A M, Zhu M, Yang Y, Waibel H F, Konuma M, Starke U and Weber C J 2012 Ageing of electrochemical double layer capacitors *J. Power Sources* 203 262–73
- [21] Hahn M, Kötz R, Gallay R and Siggel A 2006 Pressure evolution in propylene carbonate based electrochemical double layer capacitors *Electrochim. Acta* 52 1709–12

- [22] Oz A, Gelman D, Goren E, Shomrat N, Baltianski S and Tsur Y 2017 A novel approach for supercapacitors degradation characterization J. Power Sources 355 74–82
- [23] Rokaya C, Keskinen J and Lupo D 2022 Integration of fully printed and flexible organic electrolyte-based dual cell supercapacitor with energy supply platform for low power electronics J. Energy Storage 50 104221
- [24] Keskinen J, Sivonen E, Jussila S, Bergelin M, Johansson M, Vaari A and Smolander M 2012 Printed supercapacitors on paperboard substrate Electrochim. Acta 85 302–6
- [25] Lehtimäki S, Railanmaa A, Keskinen J, Kujala M, Tuukkanen S and Lupo D 2017 Performance, stability and operation voltage optimization of screen-printed aqueous supercapacitors Sci. Rep. 7
- [26] Rokaya C, Keskinen J, Bromels C, Sch ffner P, Küzeci E and Lupo D 2021 Polymer-based printed electrolytic capacitor and its circuitry application in a low pass filtering, rectifying and energy storage unit Flex. Print. Electron. 6 25005
- [27] Wang W, Yuan Y, Yang J, Meng L, Tang H, Zeng Y, Ye Z Z and Lu J 2018 Hierarchical core-shell Co<sub>3</sub>O<sub>4</sub>/graphene hybrid fibers: potential electrodes for supercapacitors J. Mater. Sci. 53 6116–23
- [28] Liu Y, Weng B, Razal J M, Xu Q, Zhao C, Hou Y, Seyedin S, Jalili R, Wallace G G and Chen J 2015 High-performance flexible all-solid-state supercapacitor from large free-standing graphene-PEDOT/PSS Films Sci. Rep. 5 17045
- [29] Awitdrus A, Suleman M, Syahirah N and Shamsudin S 2016 Energy and power of supercapacitor using carbon electrode deposited with nanoparticles nickel oxide Int. J. Electrochem. Sci. 11 95–110
- [30] IEC 62391-1 2006 International standard: Fixed electric double-layers capacitors for use in electronic equipment-Part 1: Generic Specification
- [31] Zhang Z, Lai Y, Li J and Liu Y 2009 Electrochemical behavior of wound supercapacitors with propylene carbonate and acetonitrile based nonaqueous electrolytes J. Cent. South Univ. Technol. 16 247–52



# PUBLICATION III

**Polymer-based printed electrolytic capacitor and its circuitry application in a low pass filtering, rectifying and energy storage unit**

C. Rokaya, J. Keskinen, C. Bromels, P. Schäffner, E. Küzeic and D. Lupo

Flexible and Printed Electronics

<https://doi.org/10.1088/2058-8585/ac023d>

**Publication reprinted with the permission of the copyright holders.**



# Polymer-based printed electrolytic capacitor and its circuitry application in a low pass filtering, rectifying and energy storage unit

Chakra Rokaya<sup>1</sup>, Jari Keskinen<sup>1</sup>, Cat Bromels<sup>2</sup>, Philipp Schöffner<sup>3</sup>, Erkan Küzeci<sup>4</sup> and Donald Lupo<sup>1</sup>

<sup>1</sup> Faculty of Information Technology and Communication Sciences, Tampere University, Korkeakoulunkatu 3, 33720 Tampere, Finland

<sup>2</sup> Clemson University, Department of Graphic Communications /The Sonoco Institute of Packaging Design and Graphics, USA

<sup>3</sup> Joanneum Research Forschungsgesellschaft mbH, Franz-Pichler-Strasse 30, 8160 Weiz, Austria

<sup>4</sup> TDK Foil Italy S.p.A, Via Rosenthal 5, 20089, Rozzano, Italy

## Abstract

We report the fabrication of flexible, printed polymer electrolytic capacitors and their implementation in printed electronics applications such as filtering, rectification and energy harvesting and storage. Capacitors were fabricated by depositing conductive polymer PEDOT:PSS onto porous anodized aluminum foil and yielded specific capacitance of  $1 \mu\text{Fcm}^{-2}$ . This is far higher than values reported for printed plate capacitors and opens up the possibility of new applications in printed electronics related to filtering and smoothing at low frequencies. In this work, we have used printed polymer electrolytic capacitors to implement an RC (Resistor capacitor) first order 1.03 kHz passive low pass filter, a full wave bridge rectifier circuit and a piezo-transducer energy harvester. An integrated full wave bridge rectifier based on these devices shows an efficiency of 80.5% at 1 kHz. When integrated with a vibration-motion based flexible piezoelectric transducer, the devices are able to generate and store about 1 mJ energy, which is a sufficient amount of energy for some low power electronics applications.

Keywords: PEDOT:PSS, Electrolytic capacitor, RC filter, Rectifier, Transducer, Harvester, Energy storage

## 1. Introduction

A capacitor is an important component in analog and digital electronic circuits. The most commonly known capacitors consist of a dielectric layer between two plate electrodes, and can cover a wide range of sizes and capacitance, but other types such as electrolytic capacitors and supercapacitors are also used, and we have reported previously on the use of printed supercapacitors as energy storage devices [1][2][3]. The required electrical parameters,

such as capacitance, working voltage and maximum power, vary depending on their applications. For example, capacitors are used for smoothing in radio frequency identification (RFID) tags and wireless power harvesting systems for Internet of Things (IoT). Heljo et al. reported a printed RF charge pump circuit that included printed 1.3 nF capacitors [4]. In these studies, printed plate capacitors in the nF range were used, which was suitable for these frequencies. On the other hand, rectification and smoothing of lower frequencies requires a capacitance in the  $\mu\text{F}$  range, which is not easily accessible to printing.

Electrolytic capacitors can have far higher capacitance than conventional plate capacitors of similar size, due to the high specific surface created by etching technologies. Foil etching is an electrochemically controlled selective dissolution process, which can produce 3D structures from nano to micrometric dimensions inside the aluminium foil. The geometric form of these structures depends on the combination of electrochemical process parameters, electrolyte composition and the crystal properties of the used aluminium foil [5].

A particularly interesting type of device is the polymer electrolytic capacitor. Typically, these devices comprise a polymer electrolyte or conducting polymer instead of a liquid electrolyte, and a porous aluminium film which has been oxidized as one electrode, with a current collector on the polymer, which effectively acts like a second electrode, with the aluminium oxide functioning as a very thin dielectric. The conductive polymer PEDOT:PSS (Poly(3,4-ethylenedioxythiophene):poly(styrenesulfonate), which has been used in a variety of applications in printed electronics such as supercapacitor, organic light emitting diode, transistors etc. due to its high conductivity, transparency as well as excellent stability [6], has become the most common polymer in commercial polymer electrolytic capacitors. Polymer electrolytic capacitors can have large capacitance, low equivalent series resistance (ESR) and excellent bias characteristics, which can make them suitable for smoothing and filtering applications in e.g. the kHz range and below, which can be a common frequency range in motion energy harvesting. Polymer electrolytic capacitors are widely used in numerous electronic devices, such as in digital cameras, panel displays, computer motherboards, integrated circuits and charge storage [7].

In analog circuit design, it is essential to control high frequency signals in order to get the desired signal using low pass filter circuits. A low pass filter allows or passes signals of lower frequencies while rejecting frequencies above the cutoff frequency. The cutoff frequency is the frequency of reference for the operation of the filter.

In this paper, we report the fabrication of a printed PEDOT:PSS based electrolytic capacitor in the  $\mu\text{F}$  range and describe its application in low frequency circuits such as rectifier, resistor capacitor (RC) low pass filter and a piezo transducer energy harvester system. The polymer capacitor connected across the load acts as a smoothing capacitor and attenuates noise and ac variations. When the capacitor is used as a smoothing component in a rectifier connected to a piezoelectric energy harvester, it can additionally be used to store small amounts of energy as part of a clean and renewable energy source. The use of conventional batteries in such a system is not an optimal solution, not only due to the small amount of energy being produced, so that it would take an excessively long time to charge a battery, but also because of

lower life cycle than capacitors, and the presence of corrosive, poisonous or strategically problematic materials. [8][9][10]. Due to advances in low power electronics, polymer electrolytic capacitors might be an alternative approach in energy storage units, e.g. for powering low-energy circuitry or low-power radio transmission.

## 2. Experiments

### 2.1 Fabrication of polymer electrolytic capacitor

The schematic structure of the polymer electrolytic capacitor is shown in figure 1. Figure 1 was not drawn to scale due to vast difference in length scales for various layers, between nm and  $\mu\text{m}$ , as well as the porosity of the aluminum foil. It consists of an anode and a cathode separated by a dielectric layer ( $\text{Al}_2\text{O}_3$ ). Aluminum foil Alpha 897 220V (TDK Foil Italy S.p.A.) with thickness of 85  $\mu\text{m}$  was used as anode. The foil was supplied etched and porous, with an oxide layer of ca. 300 nm produced by anodic oxidation. The etching process is mainly composed of two steps, pre-etching (the formation of fine tunnels) and etching (tunnel enlargement according to the desired tunnel diameter). The surface of the etched foil is covered by an aluminum oxide layer, which serves as dielectric. Therefore, the tunnel diameter of the etched foil must be optimized to accommodate the thickness of this layer, which increases with increasing forming voltage. The oxide layer for main capacitor applications is made of crystalline high purity  $\gamma$ -alumina with a low leakage current behavior. Due to low yield as a result of cracking of the brittle as-received oxide layer during handling, an additional oxidation was performed before device preparation to heal cracks. This was performed in 0.01 molar citric acid at a voltage of 35 V, (total oxide thickness 1.4  $\text{nmV}^{-1}$ ), using a platinum metal as cathode and the aluminum foil as anode. The reforming at 35 V leads to a thickness of ca. 49 nm on top of the cracks, which is thinner than the average layer on the as-received foils but, due to low relative surface area, does not make a substantial difference in the capacitance. After anodization, highly conductive, stabilized poly(3,4-ethylenedioxythiophene) polystyrene sulfonate PEDOT:PSS (Heraeus Clevios S V4) was deposited onto the foil by doctor blade coating [11]. The thickness of the ink layer was 200  $\mu\text{m}$  and the area 16  $\text{cm}^2$ . The curing temperature was 130  $^\circ\text{C}$  for 30 minutes. Finally, a current collector made of graphite ink (Henkel Electrodag PF-407C) with thickness of 150  $\mu\text{m}$  and area 14.4  $\text{cm}^2$  was printed on top. The ink was cured at 60  $^\circ\text{C}$  for 20 minutes and a 50  $\mu\text{m}$  thick copper tape (3M) was attached on top of graphite for robust electrical contact.

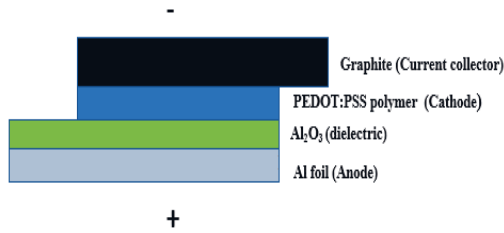


Figure 1: Schematic structure of polymer electrolytic capacitor.

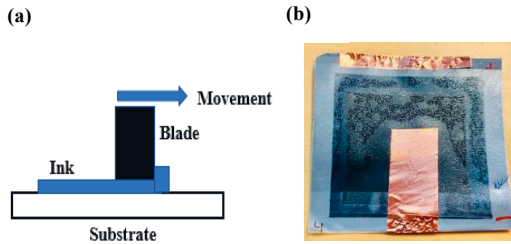


Figure 2: (a) Doctor blade printing method (b) Fabricated electrolytic capacitor.

### 3. Results and Discussion

#### 3.1 Microstructure

Microscopy analysis of etched and formed aluminium foil before and after deposition of polymer was performed with scanning electron microscopy (SEM) as shown in figure 3 and 4. The standard capacitor foil is etched and formed on both of the surfaces. In this study the prototype capacitor has been prepared using only one surface of the foil with polymer deposition (as shown in figure 4(a)). The porous fine tunnel structure of aluminium is clearly visible as well as the PEDOT:PSS layer with thickness of 4-6  $\mu\text{m}$ . Energy dispersive X-ray analysis (EDX) analysis in figure 5 reveals the presence of organic compounds especially due to sulphur, which is attributed to the PEDOT:PSS layer. Near the interface between aluminium foil and polymer deposit, we can see only some traces of carbon.

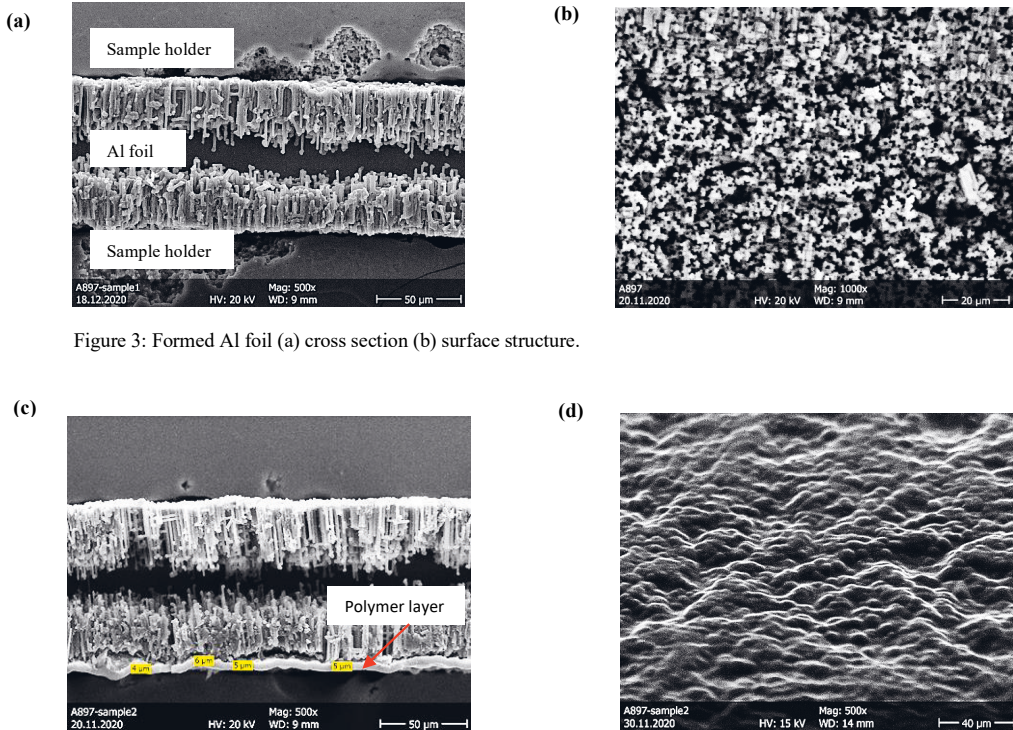


Figure 3: Formed Al foil (a) cross section (b) surface structure.

Figure 4 : Deposited PEDOT:PSS (c) cross section (d) surface structure.

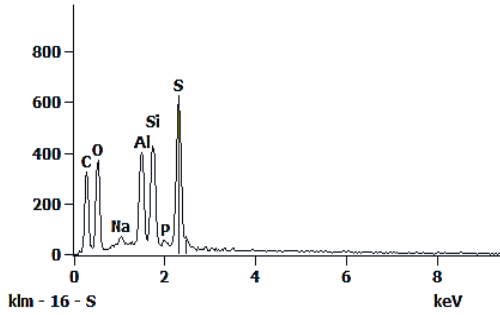


Figure 5: EDX analysis of the surface with PEDOT:PSS.

### 3.2.1 Cyclic voltammetry measurement

A Zennium electrochemical workstation (Zahner Elektrik GmbH) was used for the characterization of the polymer electrolytic capacitor using cyclic voltammetry (CV) and electrochemical impedance spectroscopy (EIS). In the CV method, voltage is scanned linearly with time to maximum value and then back to original value and current is recorded [12]. CV sweeps were measured at different scan rates from  $10 \text{ mVs}^{-1}$  to  $100 \text{ mVs}^{-1}$  (see figure 6(a)). The value of capacitance was measured using the formula given in equation 2. The defined capacitance at different scan rates is shown in figure 6(b). The values were in the range  $13.3 \mu\text{F}$  to  $14 \mu\text{F}$ .

If  $V(t)$  is an applied voltage to the capacitor, then the current  $I(t) = C \frac{dV}{dt}$  -----(1)

Then Capacitance,  $C = \frac{I(t)}{dV/dt}$  ----- (2)

where  $dV/dt$  is the scan rate [13].

### 3.2 Device characterization

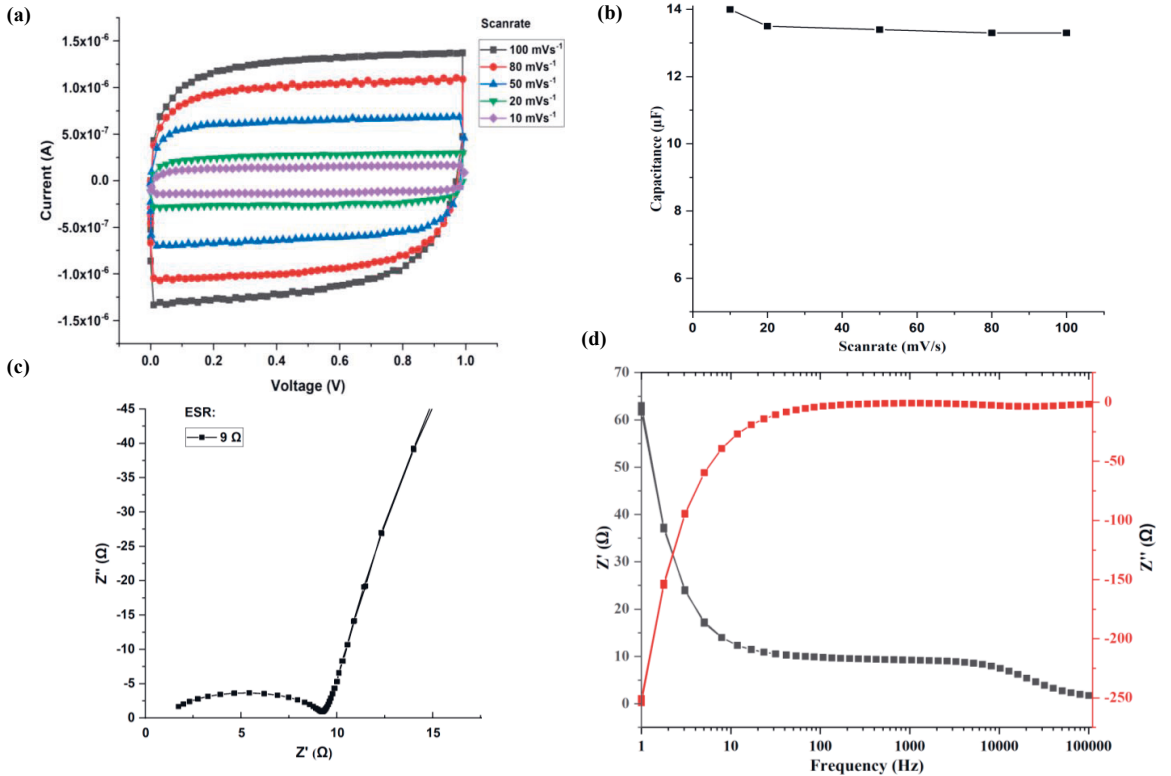


Figure 6: Device characterization (a) Cyclic voltammograms graph. (b) Capacitance vs scan rate. (c) Equivalent series resistance defined from Nyquist plot. (d) Plot of real and imaginary impedance vs frequency.

The Nyquist plot in figure 6(c) shows real ( $Z'$ ) and imaginary ( $Z''$ ) impedance of the polymer electrolytic capacitor and the extraction of the ESR from the plot. The frequency range was 1 Hz - 100 kHz to generate the impedance curve until loop was observed. The curve is nearly vertical at low frequencies, a sloped line at middle frequencies, and a semicircle loop at high frequencies [14]. The equivalent series resistance was found from the curve to be about 9  $\Omega$ .

### 3.2.2 Mechanical and electrical reliability

Mechanical, electrical, and environmental robustness is critical for the reliability of electronic components in flexible applications. In order to evaluate the flexibility of the electrolytic capacitors, the device was bent, twisted, and rolled using a rod with a radius of curvature of 0.4 cm while cyclic voltammograms of the device at 100 mVs<sup>-1</sup> were measured and compared to flat devices, as shown in Figures 7 and 8. The CV curves were identical, thus the device shows good mechanical as well as electrical stability.

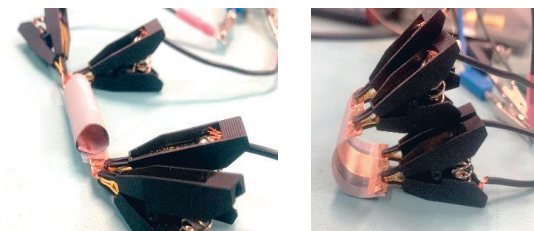


Figure 7: Photograph of electrolytic capacitor under bending test (rolled and twisted).

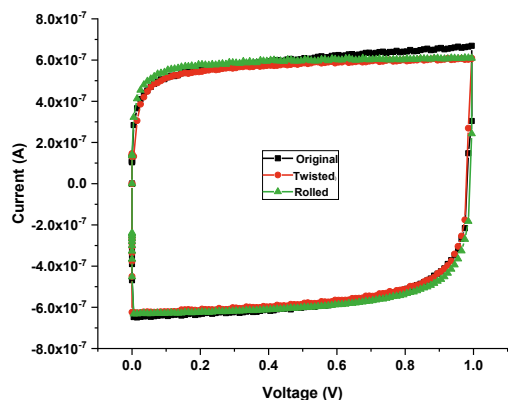


Figure 8: Cyclic voltammograms under different bend conditions.

We investigated temperature stability by performing cyclic voltammetry (CV) at temperatures from 20 °C to 90 °C, as shown in Figure 9. The shape of CV curves continued to

indicate good capacitor performance over this temperature range. We observed a reversible increase in capacitance with temperature, which agrees with earlier results on polymer tantalum capacitors by Freeman et al. which were attributed to thermal expansion of the PEDOT:PSS and resulting increase of contact area between electrode and dielectric [15].

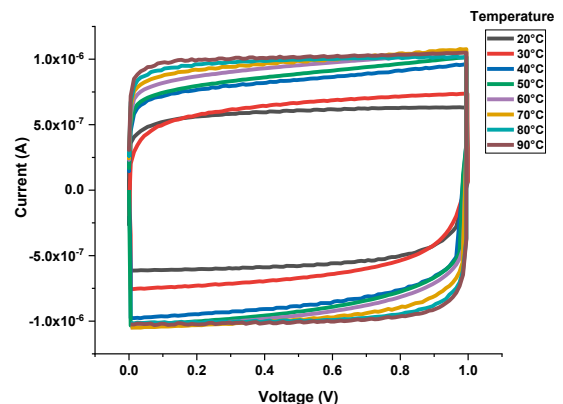


Figure 9: Cyclic voltammetry measurement on temperature dependence of polymer electrolytic capacitor from 20 °C to 90 °C.

### 3.2.3 Bode Plot Analysis

The complex impedance was defined by the equation.

$$Z^* = Ze^{j\theta} \text{ ----- (3)}$$

where  $Z$  is impedance and  $\theta$  is phase angle.

$$\text{The impedance is further expressed as } Z = \frac{1}{2\pi fc} \text{ ----- (4)}$$

Electrochemical impedance spectroscopy method was used to characterize the capacitor. The Bode plot is shown in figure 10. From the phase frequency response, the peak phase angle measured was -85.6 °, which is close to the ideal capacitor value of -90 ° [16]. The characteristic frequency was determined to be 32.2 kHz at a phase angle of -45°. This corresponds to a relaxation time of only 30  $\mu$ s ( $t_0 = f_0^{-1}$ ). This is the minimum time needed to discharge energy from the device with an efficiency greater than 50 % [17]. The phase angle declined at higher frequency because of the frequency dependence of the capacitive reactance of the capacitor [18]. The measured impedance phase angle of our polymer electrolytic capacitor at 120 Hz (a figure of merit in AC line filtering) was -84 °, which is comparable to previously reported literature values [17][16][19]. The impedance is inversely proportional to frequency, as seen in equation 4. This is due to the reactive component (capacitive) to the current, which is frequency dependent. At the highest

frequency, the Ohmic resistance dominates the impedance, and the impedance value is constant [20].

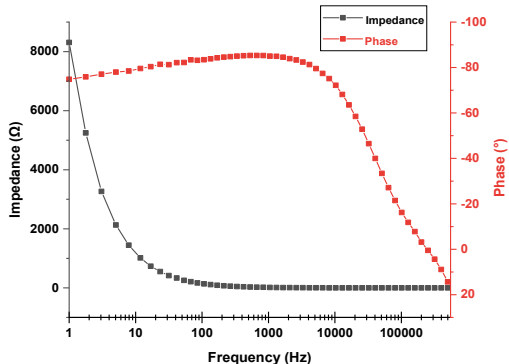


Figure 10: Bode plot analysis of electrolytic capacitor.

### 3.2.4 Dependence of capacitance on area

The capacitance was measured based on geometrical area of 2 cm<sup>2</sup>, 4 cm<sup>2</sup>, 6 cm<sup>2</sup> and 16 cm<sup>2</sup> respectively. As expected, the capacitance is proportional to the area, as shown in Figure 11. The measured specific capacitance was 1 μFcm<sup>-2</sup>.

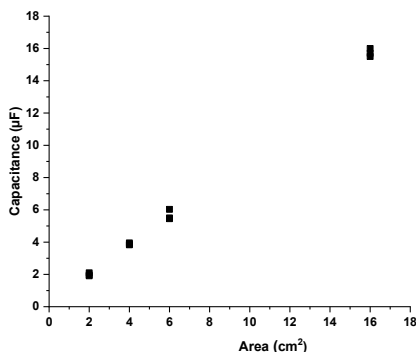


Figure 11: Capacitance vs area.

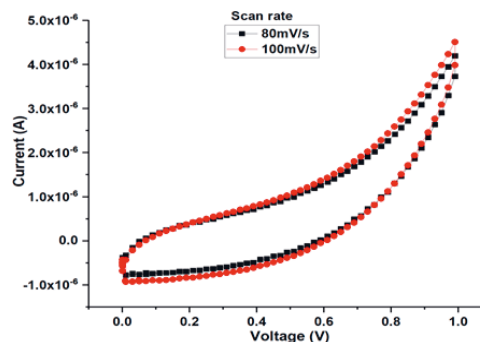
### 3.3 Post formation of polymer electrolytic capacitor

We observed that some fabricated capacitors showed irregular and non-symmetrical cyclic voltammograms, as shown in figure 12(a). The possible reasons include defects or cracks in the dielectric oxide layer occurring after the fabrication process and mechanical stress upon foil bending, winding etc. These defects were repaired by post formation or reforming after the device had been assembled, which led to stable electrical performance [21]. During reforming, a voltage was applied gradually until the chosen maximum anodized voltage of 35 V was reached, then this voltage was

held constant for 5 minutes. We ensured that no heating occurred in the capacitor. Once the reforming process was completed, the capacitor was disconnected from power supply and discharged completely. After the oxide reforming process, the CV curves were symmetrical and well behaved at 80 mVs<sup>-1</sup> and 100 mVs<sup>-1</sup>, as shown in figure 12(b). Thus, post formation of aluminum oxide increases the yield in printed electrolytic capacitors by healing cracks in the dielectric.

The measured capacitance value of 14 μF yields a specific capacitance of about 1 μFcm<sup>-2</sup>. The nominal capacitance value for the original foil used is 1.37 μFcm<sup>-2</sup>, including both sides of the aluminum foil. There is also potential for improvement. By optimizing etch morphology, dielectric thickness and polymer penetration, it is possible to obtain higher capacitance values. Optimization of the etched architecture for a specific purpose (this work used a commercial foil optimized for different architectures) would allow complete penetration of pores by the conductive polymer, while reduction of oxide thickness to the minimum required for the voltage range application would increase the capacitance per unit area in the area in which the PEDOT-PSS contacts the dielectric.

(a)



(b)

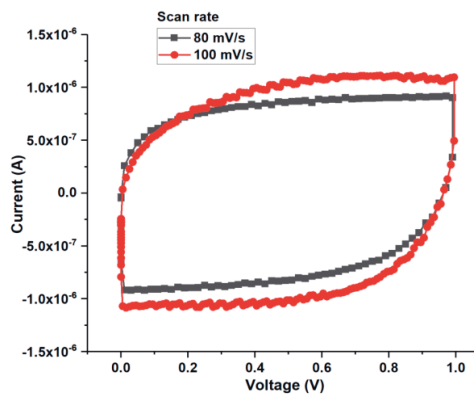


Figure 12: Cyclic voltammograms (a) Before post formation. (b) After post formation.



To measure leakage current, the voltage applied to the capacitor was held constant at a maximum value of 35 V for one hour and the small float current required to maintain that voltage level is recorded as leakage current of the capacitor. The measured leakage current was 0.2  $\mu$ A.

In order to observe the potential and long term cyclic stability of the capacitor, the capacitor underwent cyclic tests from 1 cycles to 100 cycles at a scan rate of 50 mVs<sup>-1</sup>. We observed the stable cyclic voltammograms shown in figure 13 and capacitance values were well retained up to 100 cycles.

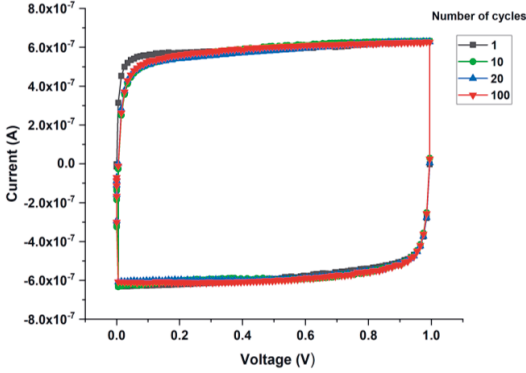


Figure 13: Cyclic measurement from 1 cycle to 100 cycles at scan rate 50mVs<sup>-1</sup>.

### 3.4 Resistor capacitor (RC) low pass filter

A resistor capacitor filter is a simple RC circuit which passes low frequency signals until it reaches its cutoff frequency and attenuates higher frequency signals. National Instrument Multisim 14.1 version software was used for the simulation of RC low pass filter. The circuit diagram of a simple RC low pass filter is shown in figure 14. It is a first order low pass filter consisting of a single resistor in series and a capacitor in parallel with the load. The input sinusoidal signal  $V_{in} = 1$  V<sub>pp</sub> is applied to the filter circuit by a function generator and output signal  $V_{out}$  was measured across the capacitor with an oscilloscope. The frequency range was from 2 Hz to 13 kHz. Simulated and experimental results were compared. The equations for cutoff frequency and phase shift are given by:

$$\text{Cutoff frequency, } f_c = \frac{1}{2\pi RC} \quad (5)$$

$$\text{Phase shift } \phi = -\arctan(2\pi RC) \quad (6)$$

where R is the resistor and C is the capacitance [22].

Using equation 5, the RC values used for low pass filter at a cut-off frequency 1.03 kHz are R=11  $\Omega$  and C=14  $\mu$ F.

The simulated results shown in figure 15 give a gain of -3 dB and phase shift of -45° at cutoff frequency. The simulated

voltage on the output at 1.03 kHz and 10 kHz were 0.7 V<sub>pp</sub> and 0.1 V<sub>pp</sub>, respectively. (See figure 16).

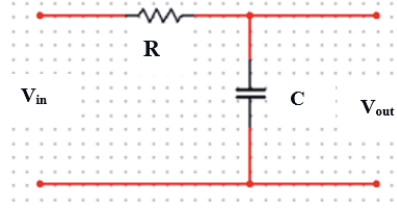
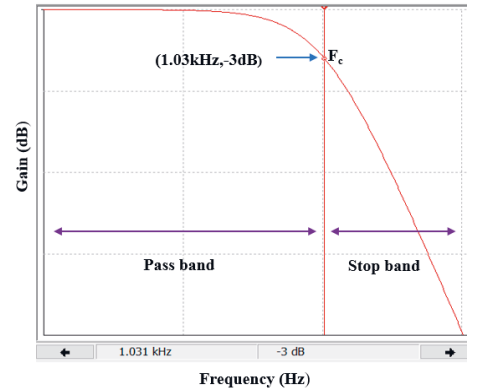


Figure 14: RC low pass filter circuit.

(a)



(b)

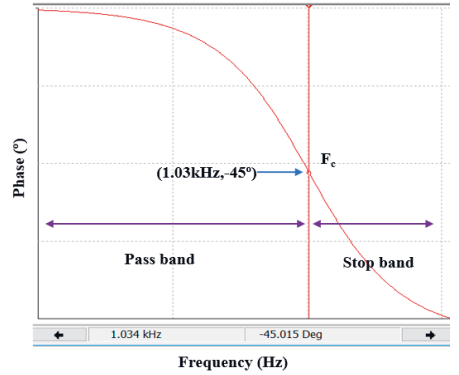


Figure 15: Simulated (a) Gain-frequency response. (b) Phase-frequency response of low pass filter at 1.03kHz.

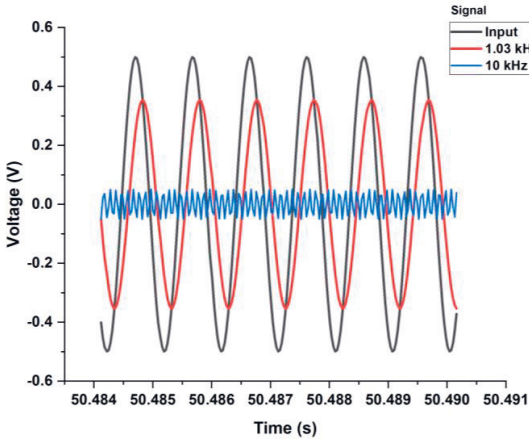


Figure 16: Simulated sinusoidal input and output signal of low pass filter 1.03 kHz signal and 10 kHz signal.

After simulation, a measurement was performed on the low pass filter using the same parameters used for simulation. The input voltage to the filter was  $1 V_{pp}$  and the output voltage was measured in the frequency range from 2 Hz to 13 kHz. The gain and phase of the filter at the nominal cutoff frequency of 1.03 kHz were -3 dB and  $-44.8^\circ$ , respectively, as shown in figure 17. The measured output signal was  $0.74 V_{pp}$  at 1.03 kHz and attenuated beyond its cutoff frequency (see figure 17 & 18). Experimental results are compared to the simulated values in table 1.

Table 1: Simulated and measured results of RC low pass filter at  $1 V_{pp}$

Parameters	Simulated values	Measured values
Cutoff frequency $f_c$	1.03 kHz	1.03 kHz
Gain @ $f_c$	-3 dB	-3 dB
Phase @ $f_c$	$-45^\circ$	$-44.88^\circ$
$V_{outpp}$ @ $f_c$	$0.707 V_{pp}$	$0.74 V_{pp}$
$V_{outpp}$ @ 10 kHz	$0.10 V_{pp}$	$0.13 V_{pp}$

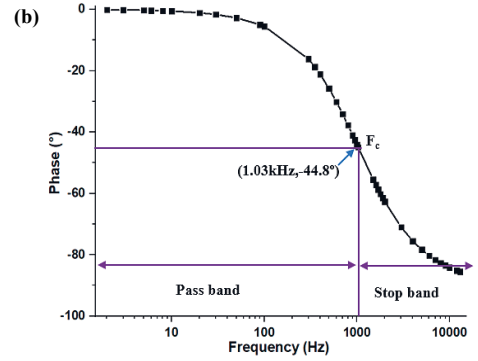
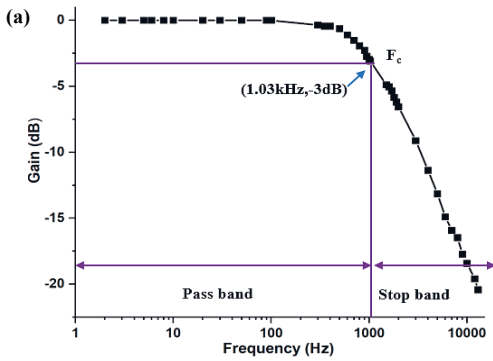


Figure 17: Measured (a) Gain-frequency response. (b) Phase frequency response of low pass filter at 1.03 kHz.

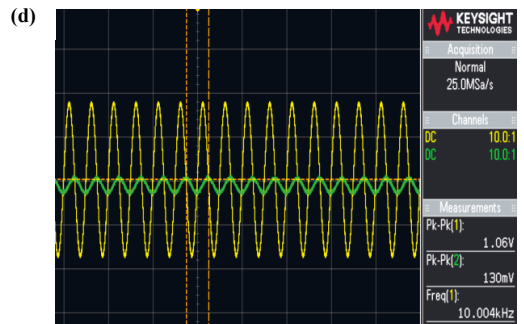
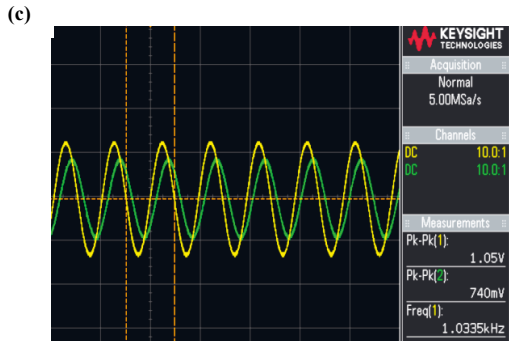


Figure 18: Measured sinusoidal input and output signal of low pass filter (c) 1.03 kHz. (d) 10 kHz. Yellow colour is input signal and green colour is output signal.

### 3.5 Smoothing capacitor

AC power can be converted into DC power using rectifiers [23]. Among other rectifiers, full wave bridge rectifiers are widely used in various electronics system such as frequency multipliers, automatic gain control system, expander circuits etc. [24]. A full wave bridge rectifier consists of four diodes arranged in bridge form as shown in figure 19 (a). The printed electrolytic capacitor of 14  $\mu\text{F}$  acts as a smoothing capacitor and was connected to the output of the rectifier to eliminate noise, ripples etc. Commercial Schottky diodes BAT46 were used for rectification. A function generator was used to provide an input voltage of 4 V<sub>pp</sub> at 1 kHz frequency and the rectified output voltage was measured with an oscilloscope with and without smoothing capacitor, as shown in figure 19 (b & c).

The efficiency of the full wave bridge rectifier is,

$$\eta = \frac{\text{dc output power}}{\text{ac input power}} = \frac{V_{dc}^2/R}{V_{rms}^2/R} \text{-----} (7)$$

and

$$V_{dc} = \frac{2V_m}{\pi} \text{ and } V_{rms} = \frac{V_m}{\sqrt{2}} \text{-----} (8)$$

where  $V_{dc}$  is a DC voltage,  $V_{rms}$  is root mean square voltage,  $R$  is the load resistance and  $V_m$  is the respective maximum output voltage

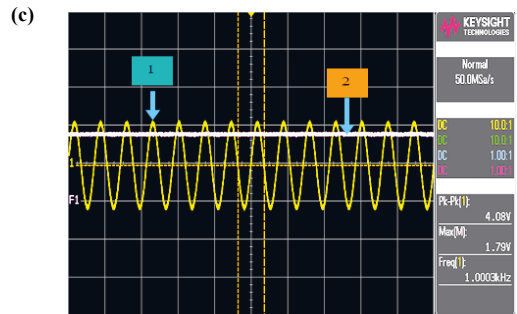
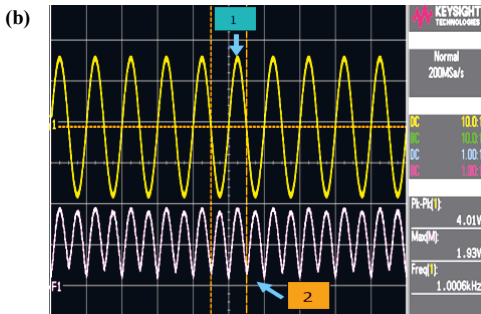
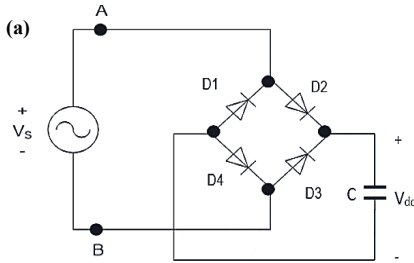


Figure 19. (a) Bridge rectifier. Input and output waveform of full wave bridge rectifier (b) without smoothing capacitor. (c) with smoothing capacitor. 1-input signal; 2-output signal.

The values for the rectifier reported here were found to be  $V_m = 1.8 \text{ V}$ ,  $V_{dc} = 1.14 \text{ V}$  and  $V_{rms} = 1.26 \text{ V}$ . The measured efficiency,  $\eta$ , was 80.5 % and in practice the maximum efficiency of a full wave bridge rectifier is 81.06 %, [25] which was close to the observed value. The measured ripple voltage  $V$  peak-peak was about 0.033 V. Thus, the printed polymer electrolytic capacitor is suitable for filtering and minimizing output ripple at relatively low frequencies.

### 3.6 Piezo harvester and energy storage unit

Energy harvesting allows capturing energy from surroundings in form of heat, movement, pressure etc.[26] Energy conversion of mechanical to electrical energy by piezo electric transducer materials has become popular in last few years. Such harvested energy can be used for low powered systems such as calculators, watches, wireless transducers etc.[27] An energy harvester comprising a transducer, rectifier and storage capacitor was assembled; the block diagram is shown in figure 20.

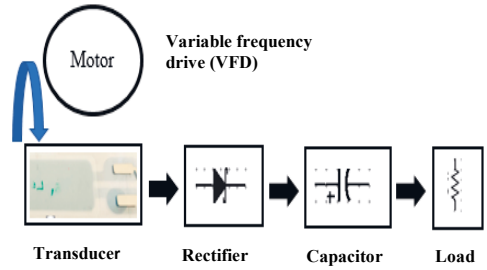


Figure 20. Block diagram of energy harvesting system.

As energy harvesting transducer, a PyzoFlex® sensor was used (Joanneum Research Forschungsgesellschaft mbH, Austria), which is a poly(vinylidene fluoride trifluoroethylene) (P(VDF-TrFE))-based piezoelectric transducer fully screen-printed on a film substrate [28] [29]. The transducer had an active area of 14 cm<sup>2</sup> and the 14 µF capacitor was used for charge storage. The motor used for excitation of the transducer was controlled by a VFD (variable frequency drive) in frequency range 2 Hz to 20 Hz. One side of the transducer was fixed, and other side oscillated when a mechanical load attached to the motor shaft struck on the transducer. Figure 21 shows the transducer connected the rectifier and capacitor. Figure 22 shows the time plots of the AC voltage from the transducer and the rectified voltage.

The rectified voltage and charge generated are proportional to the excitation frequency. Once the capacitor is charged to peak voltage, corresponding to the output voltage of the transducer, then the voltage at the capacitor remains constant. Because of the small amount of energy from single piezo transducer, it takes about 1 minute to completely charge the capacitor

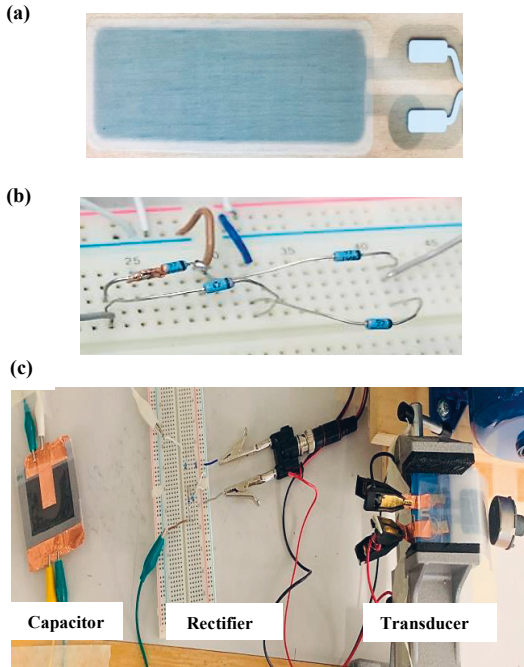


Figure 21. (a) Piezo transducer. (b) Close view of rectifier connection. (c) Piezo transducer bending motion setup with energy storage unit.

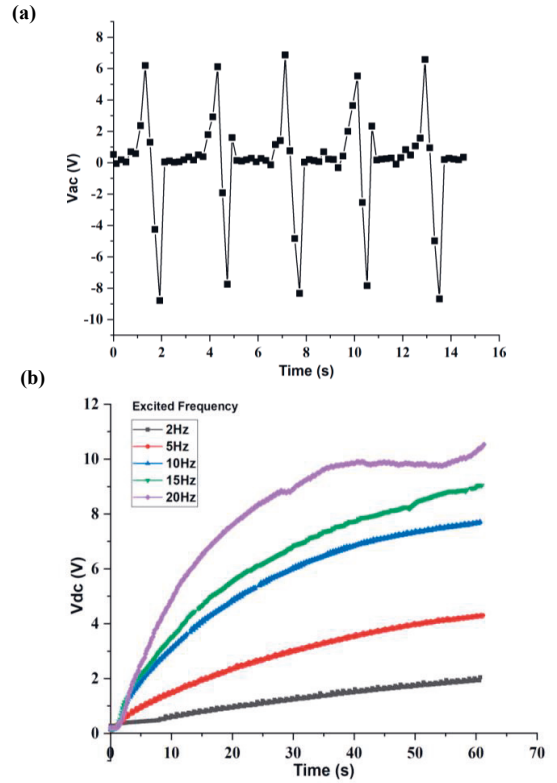


Figure 22. (a) Output response of transducer at 10 Hz. (b) Rectified voltage of transducer from 2 Hz to 20 Hz.

The equation for energy harvested is  $E = \frac{1}{2}CV^2$  -----(9)

where C is the capacitance and V is the rectified voltage [30]. The rectified voltage at 20 Hz was 11 V to 12 V and thus the amount of energy stored in the 14 µF capacitor was about 1 mJ. The short drop in rectified voltage at 55 seconds was due to temporary loss of contact between the load and transducer. As a result, the capacitor partially discharged, and the voltage declined. After the contact was re-established, the output of the transducer was high enough to charge the capacitor efficiently. This energy is enough to operate low power portable devices [9]. Since the energy is proportional to the square of the voltage, considerably more energy can be generated by increasing the output voltage of transducer by applying higher frequency.

## 4. Conclusion

We have printed flexible polymer-based electrolytic capacitors with a specific capacitance of about  $1 \mu\text{Fcm}^{-2}$ . Post formation of aluminum oxide helps to maintain stable electrical values in polymer electrolytic capacitors by regenerating the oxide layer which might be damaged during fabrication. Our modeling and fabrication experiments show that the polymer electrolytic capacitor has potential in RC low pass filtering. Thus, printed polymer electrolytic capacitors can take over conventional capacitors in electronic circuits and deliver capacitance values that are not achievable with printed dielectric capacitors. With a piezo harvester setup, the capacitor was able to store energy in the mJ scale. Thus, the polymer electrolytic capacitor can act as a next generation energy storage system in low power portable devices.

## Acknowledgements

This work was financially supported from the European Union's Horizon 2020 research and innovation programme under grand agreement n 825143, project Smart2Go. We thank TDK Foil Italy S.p.A. for providing the aluminum foils with microscopy/SEM images and Joanneum Research Forschungsgesellschaft mbH, Austria, for providing the PyzoFlex® piezo transducers.

## References

- [1] Lehtimäki S, Railanmaa A, Keskinen J, Kujala M, Tuukkanen S and Lupo D 2017 Performance, stability and operation voltage optimization of screen-printed aqueous supercapacitors *Sci. Rep.* **7**
- [2] Keskinen J, Lehtimäki S, Dastpak A, Tuukkanen S, Flyktman T, Kraft T, Railanmaa A and Lupo D 2016 Architectural modifications for flexible supercapacitor performance optimization *Electron. Mater. Lett.* **12** 795–803
- [3] Railanmaa A, Lehtimäki S, Keskinen J and Lupo D 2019 Non-toxic printed supercapacitors operating in sub-zero conditions *Sci. Rep.* **9** 14059
- [4] Heljo P, Lilja K E, Majumdar H S and Lupo D 2014 High rectifier output voltages with printed organic charge pump circuit *Org. Electron.* **15** 306–10
- [5] Goad D G W and Uchi H 2000 Modelling the capacitance of d.c. etched aluminum electrolytic capacitor foil *J. Appl. Electrochem.* **30** 285–91
- [6] Volkov A V., Wijeratne K, Mitraka E, Ail U, Zhao D, Tybrandt K, Andreasen J W, Berggren M, Crispin X and Zozoulenko I V. 2017 Understanding the Capacitance of PEDOT:PSS *Adv. Funct. Mater.* **27**
- [7] Pamanokgroup 2012 Polymer Aluminum Capacitors : World markets, technologies and opportunities 1–22
- [8] Renaud M, Fiorini P, van Schaijk R and van Hoof C 2009 Harvesting energy from the motion of human limbs: the design and analysis of an impact-based piezoelectric generator *Smart Mater. Struct.* **18** 35001
- [9] Rokaya C, Schaeffner P, Tuukkanen S, Keskinen J and Lupo D 2019 Motion energy harvesting and storage system including printed piezoelectric film and supercapacitor *2019 IEEE International Flexible Electronics Technology Conference, IFETC 2019*
- [10] Kang D H P, Chen M and Ogunseitan O A 2013 Potential environmental and human health impacts of rechargeable lithium batteries in electronic waste *Environ. Sci. Technol.* **47** 5495–503
- [11] Keskinen J 2018 *Supercapacitors on Flexible Substrates for Energy Autonomous Electronics* (Tampere University)
- [12] Lehtimäki S 2017 *Printed Supercapacitors for Energy Harvesting Applications* (Tampere University)
- [13] Wang W, Yuan Y, Yang J, Meng L, Tang H, Zeng Y, Ye Z Z and Lu J 2018 Hierarchical core-shell Co3O4/graphene hybrid fibers: potential electrodes for supercapacitors *J. Mater. Sci.* **53** 6116–23
- [14] Sun X, Zhang X, Zhang H, Huang B and Ma Y 2013 Application of a novel binder for activated carbon-based electrical double layer capacitors with nonaqueous electrolytes *J. Solid State Electrochem.* **17** 2035–42
- [15] Freeman Y, Luzinov I, Burtovoy R, Lessner P, Harrell W R, Chinnam S and Qazi J 2017 Capacitance Stability in Polymer Tantalum Capacitors with PEDOT Counter Electrodes *ECSS J. Solid State Sci. Technol.* **6** N104–10
- [16] Zhang M, Zhou Q, Chen J, Yu X, Huang L, Li Y, Li C and Shi G 2016 An ultrahigh-rate electrochemical capacitor based on solution-processed highly conductive PEDOT:PSS films for AC line-filtering *Energy Environ. Sci.* **9** 2005–10
- [17] Hua W, Xiu J, Xiu F, Zhang Z, Liu J, Lai L and Huang W 2018 Micro-supercapacitors based on oriented coordination polymer thin films for AC line-filtering *RSC Adv.* **8** 30624–8
- [18] Kp R 2016 Spectroscopic analysis of composite polymer electrolyte PVA : NH 4 PF 6 : ZrO 2  $\sigma$  48–51
- [19] Wu Z, Li L, Lin Z, Song B, Li Z, Moon K S, Wong C P and Bai S L 2015 Alternating current line-filter based on electrochemical capacitor utilizing template-patterned graphene *Sci. Rep.* **5** 1–7
- [20] Radha K P 2016 Magnitude Bode Plot analysis of solid polymer electrolyte PMMA complexed with adipic acid *Der Pharma Chem.* **4**–9
- [21] Ferdinand H and Wolschek H 1978 Method and apparatus for reforming solid electrolytic capacitors 56–65
- [22] Sriprachubwong C, Srichan C, Lomas T and Tuantranont A 2010 Simple RC low pass filter circuit fabricated by unmodified desktop inkjet printer *ECTI-CON2010: The 2010 ECTI International Conference on Electrical Engineering/Electronics, Computer, Telecommunications and Information Technology* pp 929–32
- [23] Pyakuryal S 2012 Implementation of AC to DC converter Using Thyristor in ATP *IOSR J. Eng.* **02** 06–11
- [24] Prempraneerach Y 1985 A single-diode full-wave rectifier *Int. J. Electron.* **58** 1033–6
- [25] Tayal D 2010 *Basic Electronics* (Faridabad: Himalaya publishing house pvt. ltd.)
- [26] Bai Y, Jantunen H and Juuti J 2018 Energy harvesting research: The road from single source to multisource *Adv. Mater.* **30** 1–41
- [27] Harb A 2011 Energy harvesting: State-of-the-art *Renew. Energy* **36** 2641–54
- [28] “Joanneum Research Forschungsgesellschaft mbH” (January 2021)

- [29] Stadlober B, Zirkel M and Irimia-Vladu M 2019 Route towards sustainable smart sensors: Ferroelectric polyvinylidene fluoride-based materials and their integration in flexible electronics *Chem. Soc. Rev.* **48** 1787–825
- [30] Kötz R and Carlen M 2000 Principles and applications of electrochemical capacitors *Electrochim. Acta* **45** 2483–98

# PUBLICATION IV

**Motion energy harvesting and storage system including printed piezoelectric film and supercapacitor**

C. Rokaya, P. Schäffner, J. Keskinen, S. Tuukkanen and D. Lupo

2019 IEEE International Flexible Electronics technology Conference (IFETC)

[10.1109/IFETC46817.2019.9073717](https://doi.org/10.1109/IFETC46817.2019.9073717)

**Publication reprinted with the permission of the copyright holders.**





# Motion energy harvesting and storage system including printed piezoelectric film and supercapacitor

C. Rokaya, P. Schaeffner\*, S. Tuukkanen, J. Keskinen and D. Lupo

Tampere University, Korkeakoulunkatu 7, Tampere, Finland 33720

\*Joanneum Research Forschungsgesellschaft mbH, Franz-Pichler-Strasse 30, 8160 Weiz, Austria

\*Contact: Chakra.Rokaya@tuni.fi., phone +358-504478515

## Abstract—

We report the study of piezoelectric transducer based on the copolymer P(VDF:TrFE) for energy harvesting based on deformation of the film. The bending characteristics, sensitivity, charge generation and frequency response at typical machine component frequencies of printed piezoelectric transducer was studied. Interestingly piezoelectric transducer shows response towards a different level of frequency and the bending forces. As expected, increased frequency and deformation yield increased energy harvesting. A harvester system in piezo flex foil with integrated rectifier and printed supercapacitor was demonstrated, which harvests sufficient energy for low power measurements or radio transmission.

## I. INTRODUCTION

Energy harvesting is a method for obtaining or capturing the possible amounts of energy from our surroundings available in the form of heat, motion, mechanic, solar, pressure gradients etc. A large amount of energy in a macro scale can be obtained from solar, wind, kinetic for domestic as well as industrial purposes. Energy harvesting is also a useful and important means of making low power distributed transducers energetically autonomous and environmentally sustainable. [1] Harb mentioned there are a number of approaches to energy harvesting. One way is energy conversion of mechanical to electrical energy using piezoelectric transducer materials. Such harvested energy can be used for low powered systems such as wireless transducers, biomedical implants, military monitoring services, structure-embedded instrumentation, remote weather station, calculators, watches, Bluetooth headsets etc. [2]

A recent trend in electronics has been a decrease of the size and power consumption of devices and components. This has enabled the creation of new applications with low power requirements. Furthermore, environmental issues and imposed regulations are associated with portable energy sources. The use of conventional batteries is not an optimal solution because of the limited cycle life and the requirement for recycling due to problematic materials. Due to advances in low power electronics, harvesting ambient energy and storage in

supercapacitors is becoming a viable and more sustainable alternative approach, including piezoelectric harvesting. [3]

Future mobile electronics technologies will focus on light weight, flexible, bendable and stretchable devices as well as large area interactive and learning environments. For such products, flexible piezoelectric materials can play important role both for sensing and energy harvesting. [4] Polyvinylidene fluoride (PVDF) is the most frequently used piezoelectric polymer. It has four phases out of which only the  $\beta$ -phase exhibits spontaneous polarization. It is semi-crystalline (about 50-60% crystallinity) with a repeating unit of  $(CH_2-CF_2)$ . The size of the crystallites and chain packing is influenced by annealing. [5] Its piezoelectric properties arise from the strong molecular dipoles within the polymer chain with piezoelectric coefficients ( $d$ ) in the range of 10-40 pC/N. [6] Introducing ca. 20-50% of trifluoroethylene (TrFE), in which one hydrogen is replaced by the slightly larger fluorine, forms a stable copolymer. [7] Energy harvesting from PVDF and its copolymer P(VDF:TrFE) has been reported previously. Bhavanasi *et al.* used bilayer films of P(VDF:TrFE) that generate  $4.41 \mu W cm^{-2}$ . [8] Dey *et al.* showed that electrical response of PVDF:TrFE nanofibers increased with excitation frequency. [9] Lee *et al.* reported micro patterned P(VDF:TrFE) based nano generators releasing  $15 \mu W$  power. Kymissis *et al.* used 16 sheets of PVDF connected in parallel in a sandwich structure in a shoe sole and was able to produce  $1 mJ/step$ . [10] Wang *et al.* used a synchronized switch harvesting on inductor (SSHI) rectifier for a PVDF stack configuration and harvested 11-13mW power. [11] Zirkel *et al.* demonstrated an all printed matrix transducer array fabricated by screen printing an ink solution of piezoelectric copolymer P(VDF:TrFE). [12] Ink jet deposition of patterned metal layers on PVDF film to realize a scalable, bendable and low costing sensing system for large area artificial skin was reported by Seminara *et al.* [13]. Because of flexibility, piezoelectric polymers it can be integrated into devices for human body health monitoring, smart clothing such as shoes, and other motion harvesters applications. [14]

Rajala *et al.* measured the sensitivity of a PVDF transducer and observed a piezoelectric coefficient of 25.1 to 26.8 pC/N, using a shaker system. [15] In this work we report the use of a similar setup for determination of the piezoelectric sensitivity, and a motor-driven bending apparatus to measure harvesting of energy from bending deformation. In addition, a 3D bending model is used to analyze the results.

## II. EXPERIMENT AND RESULTS

### A: Piezo transducer design and electrical polarization

A transducer consists of four layers. Polyethylene terephthalate (PET, Melinex ST506 from DuPont) of 175  $\mu\text{m}$  thickness was used as a substrate, printed conductive polymer PEDOT:PSS((poly(3,4ethylenedioxythiophene):poly(styrenesulfonic acid)) (Clevios SV 3 from Heraeus) act as bottom and top electrodes, and fluoropolymer P(VDF:TrFE), poly(vinylidene fluoride trifluoroethylene) (80:20) (see Ref. 12 for details) as a transducer material is sandwiched between the electrodes. Screen printing was used to deposit the transducer material and electrodes. The thickness of the transducer material was  $\sim 6\mu\text{m}$  for single layer and  $\sim 12\mu\text{m}$  for double layer. The samples were annealed at 100  $^{\circ}\text{C}$  for 10 minutes to evaporate solvents. Additionally, silver wiring was printed to electrically connect the transducer to the harvester circuitry, but is not part of the layer stack. Figure 1 shows the transducer schematic diagram.



Figure 1: Structure of Piezo transducer

In contrast to PVDF films, the copolymer P(VDF:TrFE) crystallizes into the ferroelectric  $\beta$ -phase without the need of stretching or applying of very high electric fields. In P(VDF:TrFE), the crystallites have an electric dipole moment and are embedded in an amorphous matrix. After solution-processing of P(VDF: TrFE), however, the crystalline dipoles are randomly oriented and need to be aligned in order to have a nonzero overall polarization and thus show piezoelectricity. This alignment of crystalline dipoles is usually performed by applying an electric field via attached electrodes, forcing the crystalline dipoles to be reoriented towards the external field. This process is commonly referred to as poling. [7] The poling current  $I$  and voltage  $V$  are monitored and the polarization in the ferroelectric layer can be derived using the relation

$$P = \frac{1}{A} \cdot \int I dt, \quad (1)$$

where,  $A$  is the area spanned by the electrodes. A triangular shaped alternating signal of frequency 1Hz was used for poling over several cycles until a saturation in the remanent polarization or charge, respectively, was observed (Figure 2). Plotting the polarization  $P$  over the voltage  $V$  gives the typical hysteresis loop of ferroelectrics (Figure 3). A PUND poling

method was applied to separate the remanent polarization  $P_r$  due to crystalline dipole reorientation (dotted line) from the total displacement (solid line in Figure 3). To reach a high remanent polarization and thus piezoelectric coefficient ( $d_{33}$ ), the poling voltage amplitude was chosen such as to apply about two times the coercive field strength  $E_r$  [16]

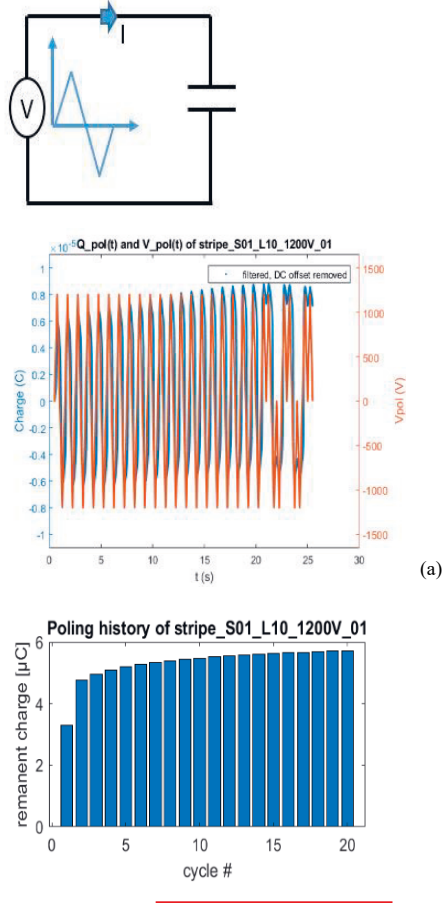


Figure 2: Poling of the ferroelectric P(VDF:TrFE). Poling charge as calculated from the monitored current and poling voltage (top); The remanent charge increases with every poling cycle and saturates, (bottom)

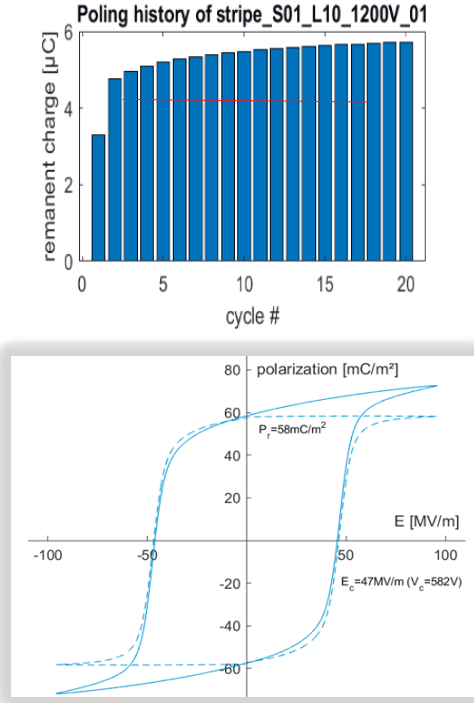


Figure 3: Typical hysteresis loop of the studied Piezoelectric transducer showing the remanent polarization  $P_r$  and coercive field strength  $E_c$ .

The coercive electric field strength measured was 47 MV/m and the remanent polarization amounts to approximately 58 mC/m<sup>2</sup>. [12]

#### B: Sensitivity measurement bending and unbending setup

A type 4810 Brüel & Kjær mini-shaker was used for material characterization. The shaker has a piston of area of 1.56 mm<sup>2</sup> and can generate a dynamic excitation force up to 10 N and frequencies up to 18 KHz. A sinusoidal input for the shaker was provided with a Tektronix AFG3101 function generator. Two types of forces were used simultaneously for sensitivity measurements. First one is static force with sensitivity of 2.646 mV/N, was used to prevent the transducer from jumping off the stage during application of dynamic sinusoidal force. The next is dynamic force with sensitivity of 530.2 mV/N at varying amplitudes up to 10 N for sensitivity measurements. The measurement set up was previously reported by Rajala *et al.* [15] Tuukkanen *et al.* [17] and Kärki *et al.* [18]

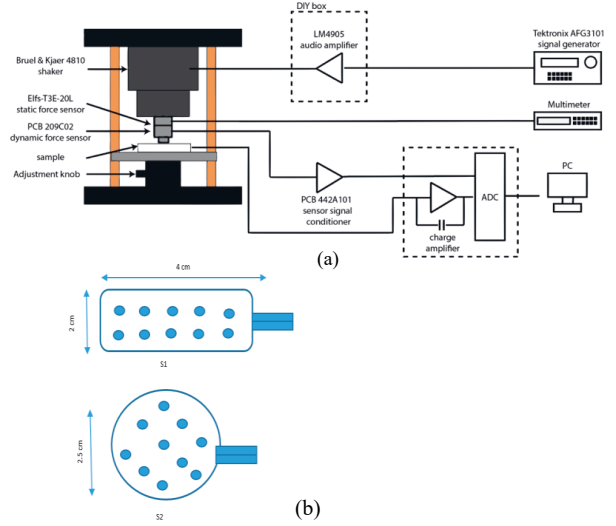


Figure 4: A schematic drawing of measurement set up (a); piezo transducer with excitations point marked (S1 and S2) (b)

Two piezo transducers, designated here as S1 and S2, were selected for measurements and compared. (REF. Table 1). In the first set of measurements in normal mode, the transducer was placed in the metal plate. In the second set of measurements (bending mode), greater sample deformation was allowed, as shown in Figure 5. A sinusoidal signal of 1 V peak to peak at 2 Hz frequency was applied as input to the shaker, which resulted in a force of approximately 1.4 N. The transducer was excited at 10 different positions. The same positions were excited from both sides of the transducer, resulting in total of 20 excitations per transducer in order to average out effects resulting from film roughness, increases the statistics and thus, decreases the effect of layer variations in the sensing layer thickness. The charge generated was measured by a charge amplifier. The sinusoidal were fit to the charge output curve and the dynamic force curve, and the sensitivity was obtained by dividing charge amplitude by force amplitude. [15]

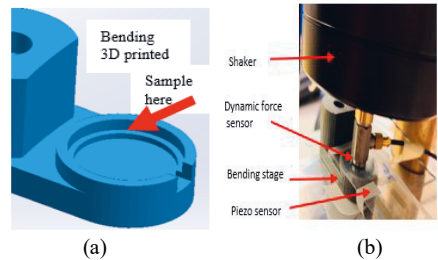


Figure 5: Bending 3d setup (a); piezo transducer excited by mini-shaker (b)

Dynamic sensitivity is the charge generated based on the force applied in pC/N and was measured using both the normal and bending mode. The dynamic sensitivity is given by

$$\text{Dynamic sensitivity} = \frac{Q}{\text{Dynamic force}} \quad (2) \quad [15]$$

TABLE 1: Dynamic sensitivity measurement results, reported as mean value  $\pm$  standard deviation

Sample measured	Dynamic sensitivity (pC/N)	
	Normal mode	Bend mode
S1(8cm <sup>2</sup> )	24.41 $\pm$ 3.2	286 $\pm$ 52
S2(7.85cm <sup>2</sup> )	23.46 $\pm$ 2.68	268 $\pm$ 23.84

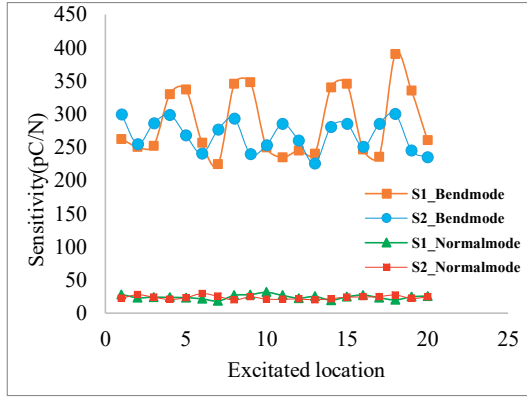


Figure 6: Sensitivity results with normal mode and bending mode

The charge generated by deformation of the material depends on the amount of force applied. Figure 7 shows generated charge as a function of applied force. Less force was required to generate a higher amount of charge using the bending stage, as it is primarily deformation that leads to charge generation. When using the bending stage 240pC charge was generated by applying 0.866 N force, compared to 27.5 pC charge from 1.4 N force using the rigid table. Rajala *et al.* [15] observed similar behavior.

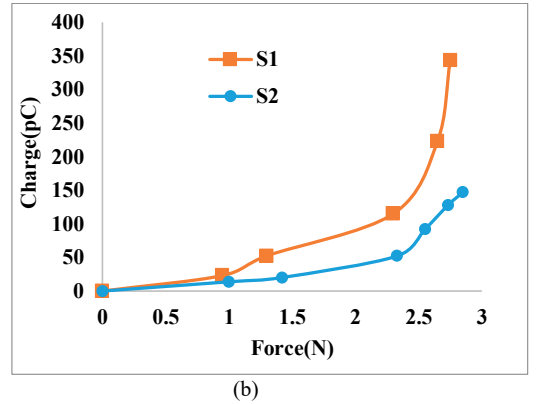
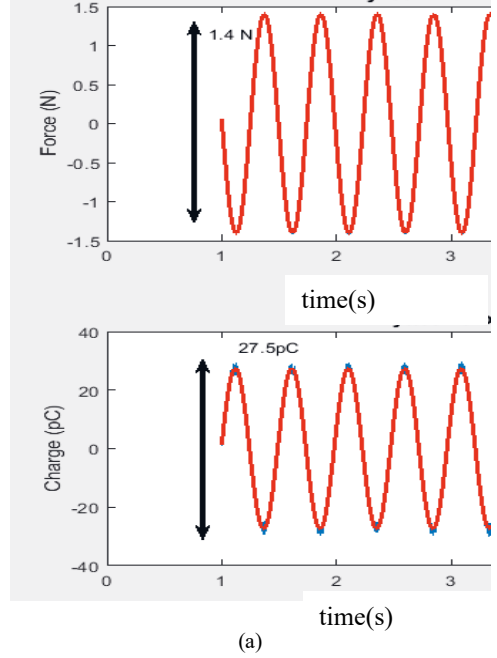


Figure 7: Charge generated based on force, normal mode (a); Graph plot of piezo transducer S1 and S2 (b)

### C: Energy harvesting by angular bending

A measurement setup for energy harvesting by bending/unbending is shown in figure 8. It consists of a servo motor that rotates from 0 to 180 ° and back with pulse width modulation, powered and controlled by an Arduino Uno microcontroller platform. A piezo transducer of 8 cm<sup>2</sup> size was attached to the cylindrical shaft of the servo motor and this was flexed and unflexed as the motor rotated. The transducer output voltage response was 8 V peak to peak. (See figure 9(a)) The output response of the piezo transducer was measured with a 10 Mega ohm NI USB-4065 multimeter from National Instruments.

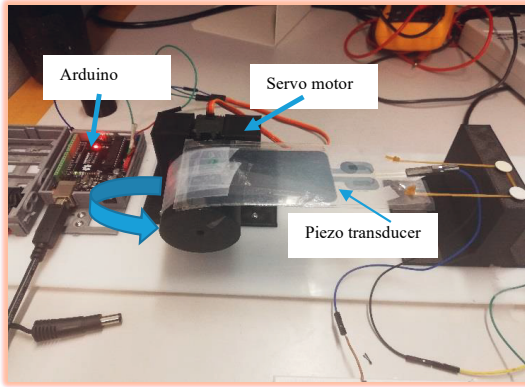


Figure 8: Setup for controlling Servomotor for angular bending

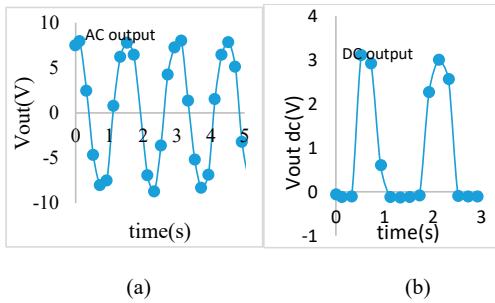


Figure 9: Piezo transducer output Voltage Ac (a); DC (b)

A half wave rectifier circuit was integrated to the transducer to convert AC into DC. The DC obtained without smoothing capacitor is shown in Figure 9b. Figure 10 shows the charging characteristics of a smoothing/storage capacitor integrated to the system. The rectified voltage across a load of 10 M Ohm is 1.05V.

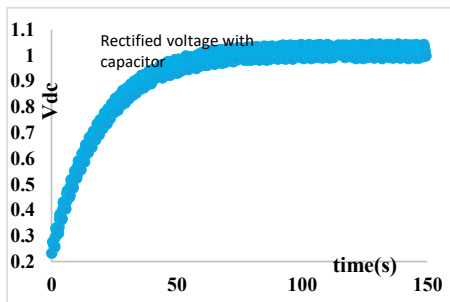


Figure 10: Rectified voltage with capacitor

The harvested energy is given by

$$E = \frac{1}{2}cv^2 \quad (3)$$

where E is energy in Joule, C is capacitance in Farads and V is the voltage across the capacitor. This yields a harvested energy of 300  $\mu$ J.

#### D: Frequency dependency of piezo transducer

An energy harvester comprising a piezo transducer, rectifier circuit and storage capacitor was assembled; the block diagram is shown in Figure 11. Figure 12 shows photographs of a harvester circuit including a voltage doubler rectifier.

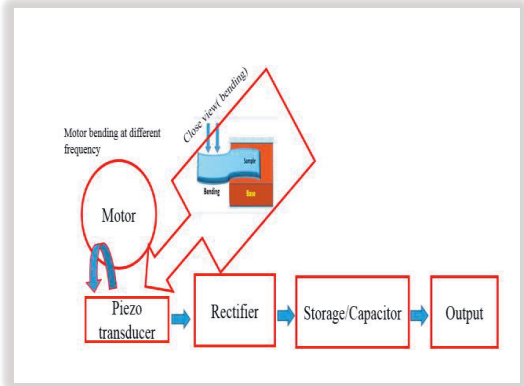


Figure 11: Variable frequency generator and energy harvesting system



Figure 12: Piezo transducer A and B + Energy harvester

Two samples were investigated using the same excitation methods. The first transducer has an area of 14 cm<sup>2</sup> (7cm \*2cm) while the second has area transducer has an area of 1cm<sup>2</sup> (1cm\*1cm); both were connected to a voltage doubler rectifier. The motor was controlled by a VFD (variable frequency drive) in order to rotate at different speeds. One side of the piezo transducer was fixed while the other side can oscillate freely. A small mechanical load was attached to the shaft of the motor. As the motor rotates, the load hits the piezo transducer and bends it up and down, generating an AC voltage. Transducer 1 has AC output response of 6 V peak to peak (See figure 13) whereas transducer 2 generates 3 V peak to peak AC at 10 Hz frequency. A National Instruments 10 mega Ohm USB 4065 multimeter was used to measure the DC output.

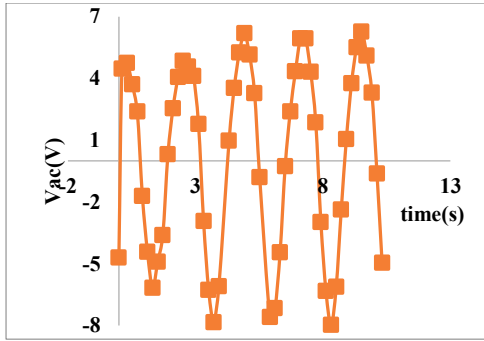
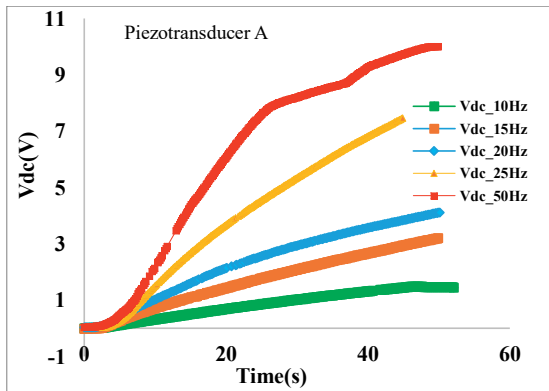


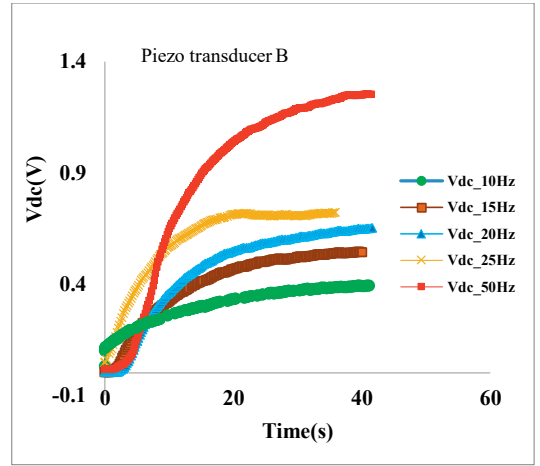
Figure 13: Response of Piezo Transducer A

As the output current of the transducer is low, it takes time to charge a capacitor greater than  $100\mu\text{F}$ . This can be observed with a  $470\mu\text{F}$  capacitor (angular bending test), which yielded an output voltage of 1.04 DC. Printed supercapacitors typically have an area specific capacitance of ca  $100\text{ mF/cm}^2$ , with leakage current more or less proportional to capacitance. [19] Due to the small amount of energy from a single transducer in this work, the leakage current for a supercapacitor in the range of hundreds of mF would be comparable to the amount of current generated. Therefore in these experiments we selected a commercial electrolytic capacitor of  $22\mu\text{F}$  and a printed  $33\mu\text{F}$  supercapacitor. This supercapacitor was fabricated using PET (polyethylene terephthalate) as substrate and graphite ink of about  $40\mu\text{m}$  thickness deposited manually by pressing ink using thin metal plate, both as current collector and electrode. One Molar aqueous sodium chloride (NaCl) was used as an electrolyte and Dreamweaver cellulose paper as a separator.

The capacitor charging curves are shown below for transducers 1 and 2 for excitation 10 Hz to 50 Hz, showing that the rectified voltage and speed of charging are proportional to the excitation frequency. This implies that the fundamental frequency response of the transducers is more or less flat over this frequency range.



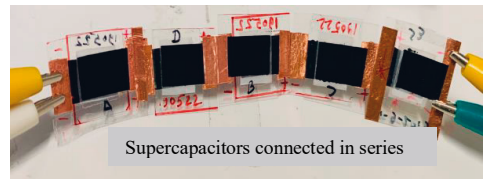
(a)



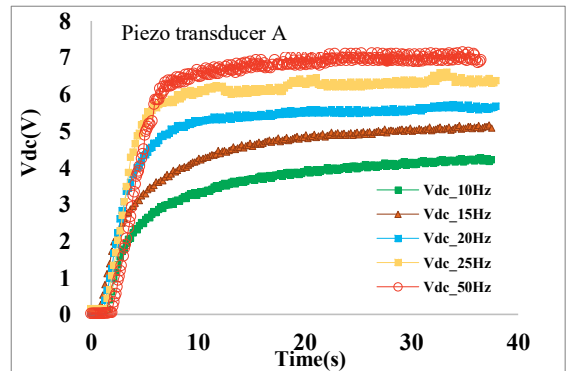
(b)

Figure 14: Rectified DC voltage of transducer A (a); transducer B (b) from 10 Hz to 50 Hz

The maximum voltage a single supercapacitor with aqueous electrolyte can withstand is about 1.2 V. In order to store the higher voltage generated by the transducer, 5 supercapacitors were connected in series, with total capacitance of  $3\mu\text{F}$  as shown in Figure 15, and could be charged up to 7 V. Figure 15 also shows the charging curve for the series connected supercapacitor module at different frequencies.



(a)



(b)

Figure 15: Five series connected supercapacitors (a); rectified voltages (b) from the harvester upon excitation in the test unit described in this work.

The rectified DC voltage increases in both transducers with the excitation frequency. The measurement was done with different piezo transducers and capacitor values. Transducer B has very low output compared to transducer 1, about 8 times less at 50 Hz due to its small area.

Table 2 summarizes the harvesting results. While it was not possible with a single transducer to charge a single 33  $\mu$ F supercapacitor fully, due to the competition between charging and leakage current, both the electrolytic capacitor and the module were charged in less than a minute.

TABLE 2: Energy harvested from 10 Hz to 50 Hz

Frequency (Hz)	Piezo transducer A				Piezo transducer B	
	V <sub>dc</sub> (V)		Energy (mJ)		V <sub>dc</sub> (V)	Energy (mJ)
	Electrolytic capacitor (EC) 22 $\mu$ F	Super capacitor (SC) 33 $\mu$ F	EC	SC		
10	1.45	4.2	0.02	0.0266	0.39	0.00251
15	3.19	5.07	0.11	0.0388	0.54	0.004811
20	4.08	5.7	0.18	0.049	0.65	0.006971
25	7.4	6.36	0.60	0.061	0.72	0.00855
50	10	7	1.12	0.073	1.25	0.0257

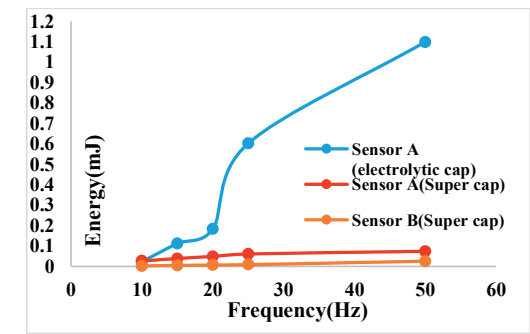


Figure 16: Energy harvested as a function of excitation frequency

This is sufficient energy to operate low power circuitry. We constructed a low power LED drive circuit using a CMOS 555 timer operated at 2V. The voltage stored in the capacitor was supplied to the LED driver circuit as shown in figure 17. The transistor acts as a switch and remains ON when the output pulse of the 555 timer drives the base of a transistor, and current flows to the LED. [20]

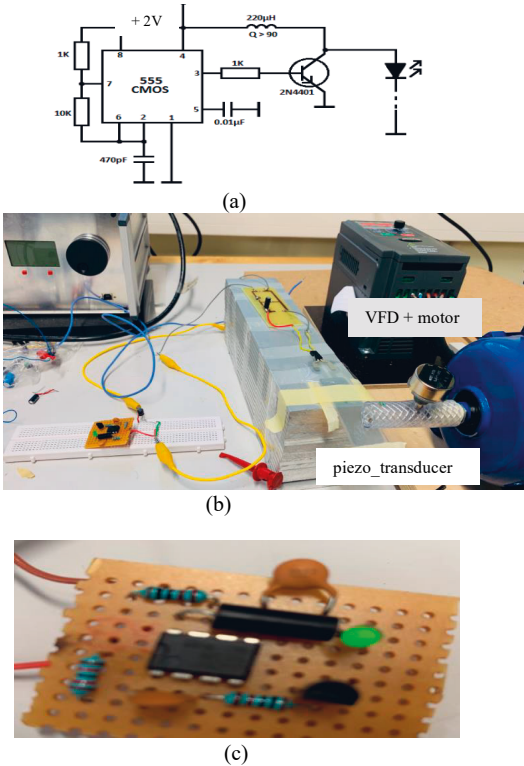


Figure 17: Schematic diagram of the LED driver circuit as published in [17] (a), photograph of the bending setup with LED driver circuit (b), and close-up of the LED driver circuit (c)

The operation voltage of the LED driver circuit was 1.85V and, current required to turn on LED was 6mA. Thus, the peak power generated by the circuit for short durations was measured i.e.  $P=1.85*6=11.1\text{mW}$ . It can be observed from Table 3 that the power generated can be used to operate a number of common low power portable devices.

TABLE 3: Power consumption of the portable devices [21] [3] [22] [23] [24]

Device		Power consumption (mW)
MP3 player		50-97
Wearable EEG		0.8
Cardiac pacemaker		0.05
Hearing aid		1
Respiratory rate meter		0.83
Heart rate meter		0.83
Blue tooth (sleep mode)		0.008
Wifi (sleep mode)		0.01
Carbon monoxide detector	Active	1.7
	Stand by	0.0018
Pagers		30



### III. CONCLUSIONS

We have tested printed piezoelectric transducers based on P(VDF:TrFE) for their potential as energy harvesters in low power electronic devices. The piezoelectric sensitivity was a strong function of the freedom of the transducer to be deformed, with average sensitivity value (pC/N) in bending 11 to 12 times higher than when applying force when the sample was mounted on a rigid holder. The response varied from 20 - 31pC/N in a rigid architecture to 225.2-390 pC/N when bending was allowed. We have furthermore tested the energy harvesting potential of these transducers in a dedicated bending unit. In addition to determining the AC voltage generated by bending, an energy harvesting circuit on foil comprising transducer, voltage doubler rectifier and printed supercapacitor or electrolytic capacitor, respectively. The system was able to generate and store up to 1.2 mJ and deliver power of at least 11.1 mW, sufficient to drive an LED. This is sufficient power to drive a number of low power portable devices and confirms the potential of printed P(VDF:TrFE) as a potential means of harvesting energy from motion for distributed electronic devices.

### References

- [1] Y. Bai, J. Jantunen and J. Jari, "Energy harvesting research: The road from single source to multisource," *Advanced materials*, 2018.
- [2] A. Harb, "Renewable Energy," *Energy harvesting : State -of-the-art*, vol. 36, 2011.
- [3] J. Rocha, P. Silva and S. Mendez, "Energy Harvesting from piezoelectric materials fully integrated in footwear," *IEEE*, vol. 57, 2010.
- [4] M. Zirkel, G. Scheipl, B. Stadlober, C. Rendl, M. Haller and P. Hartmann, "Pyzoflex : a printed piezoelectric pressure sensing foil for human machine interfaces," *Proc. of SPIE*, vol. 8831, 2013.
- [5] G. H. Heartling, "Ferroelectric Ceramics: History and Technology," *J. Am. Ceram. Soc.*, vol. 82, no. 4, pp. 797-818, 1999.
- [6] K. Rashmi, Jayarama, Navin Bappalige and R. Pinto, "A Review on vibration based piezoelectric energy harvesters," *Sahyadri International Journal of Research*, vol. 3, no. 1, 2017.
- [7] B. Stadlober, M. Zirkel and I. M. Vladu, "Route towards sustainable smart sensors: ferroelectric polyvinylidene fluoride-based materials and their integration in flexible electronics," *Royal society of Chemistry*, 2019.
- [8] V. Bhavanasi, V. Kumar, K. Parida, J. Wang and S. P. Lee, "Enhanced piezoelectric energy harvesting performance of flexible PVDF-TrFE films with graphene oxide," *ACS Publications*, vol. 8, pp. 521-529, 2015.
- [9] S. Dey, M. Purahmad, S. S. Ray and M. Dutta, "Investigation of PVDF-TrFE nanofibers for energy harvesting," *Nano Technology materials and Devices Conference*, 2013.
- [10] J. Kyminsis, C. Kendail, J. Paradiso and N. Gershenfeld, "Parasitic power harvesting in shoes," *IEEE*, 1998.
- [11] Wang, "Piezoelectric energy harvesting utilizing human locomotion," *MSc Thesis, University of Minnesota*, 2010.
- [12] M. Zirkel, A. Sawatdee and U. Helbig, "An all printed ferroelectric active matrix sensor network based on only five functional materials forming a touchless control interface," *Advanced Materials*, vol. 23, pp. 2069-2074, 2011.
- [13] L. Seminara, L. Pinna and M. Valle, "Piezoelectric polymer transducer arrays for flexible tactile sensors," *IEEE Sensors Journal*, vol. 1, no. 10, 2013.
- [14] J. Zhao and Z. You, "A shoe embedded piezoelectric energy harvester for wearable sensors," *Sensors*, vol. 14, no. 7, pp. 12497-12510, 2014.
- [15] S. Rajala, S. Tuukkanen and J. Halttunen, "Characteristics of piezoelectric polymer film sensors with solution processable graphene based electrode materials," *IEEE Sensors Journal*, vol. 15, 2015.
- [16] J. Tressler, S. Alkoy and R. Newnham, "Piezoelectric sensors and sensor materials," *Journal of Electroceramics*, vol. 2, no. 4, pp. 257-272, 1998.
- [17] S. Tuukkanen and S. Rajala, "Nanocellulose as a piezoelectric material," *IntechOpen*, 2018.
- [18] S. Kärki, M. Kiiski, M. Mäntysalo and J. Lekkala, "A PVDF sensor with printed electrodes for normal and shear stress measurements on sole," *Fundamental and Applied Metrology*, 2009.
- [19] S. Lehtimäki, M. Li, J. Salomaa, J. Pöyhönen, A. Kalanti, S. Tuukkanen, P. Heljo, K. Halonen and D. Lupo, "Performance of printable supercapacitors in an RF energy harvesting circuit," *Electrical Power and Energy Systems*, vol. 58, pp. 42-46, 2014.
- [20] "Available online" <https://www.electroschematics.com/6754/led-driver-with-555-timer/>.
- [21] V. Lenov, Energy harvesting for self powered wearable devices, Springer US, 2011, pp. 27-49.
- [22] R. Vullers, R. V. Schaijk, I. Doms, C. V. Hoof and R. Mertens, "Micropower energy harvesting," *Solid-State Electronics*, vol. 12, no. 11, 2008.
- [23] Snehalika and U. Bhasker, "Piezoelectric energy harvesting from shoels of soldier," *IEEE Power electronics, Intelligent control and Energy Systems*, pp. 1-5, 2016.
- [24] V. Bhatnagar and P. Owende, "Energy harvesting for assistive and mobile applications," *Energy Science and Engineering*, vol. 3, pp. 153-173, 2015.
- [25] J. Lekkala, J. Tuppurainen and M. Paajanen, "Material and operational properties of large area membrane type sensors for smart environments," *XVII IMEKO World Congress*, 2003.
- [26] A. V. Shirinov and W. K. Schomburg, "Pressure sensor from a PVDF film," *Sensors and Actuators*, vol. 142, pp. 48-55, 2008.
- [27] S. Lehtimäki, M. Li, J. Salomaa, P. Juho, A. Kalanti, S. Tuukkanen, P. Heljo, K. Halonen and D. Lupo, "Performance of printable supercapacitors in an RF energy harvesting circuit," *Electrical Power and Energy Systems*, vol. 58, pp. 42-46, 2014.





